MOLECULAR MODELING OF POLYMER CRYSTALS AND CRYSTALLIZATION

by

Tongtong Shen

A Dissertation

Submitted to the Faculty of Purdue University

In Partial Fulfillment of the Requirements for the degree of

Doctor of Philosophy

School of Materials Engineering

West Lafayette, Indiana

May 2021

THE PURDUE UNIVERSITY GRADUATE SCHOOL
STATEMENT OF COMMITTEE APPROVAL

Dr. Alejandro H Strachan, Chair
School of Materials Engineering

Dr. James Caruthers
Davidson School of Chemical Engineering

Dr. R. Byron Pipes
School of Materials Engineering

Dr. Jeffrey Youngblood
School of Materials Engineering

Approved by:
Dr. David F. Bahr

Dedicated to all the people I met during PhD

ACKNOWLEDGMENTS

This book would not have been written without the support of so many colleagues and friends. First and foremost, I would like to thank my advisor and supervisor Prof. Alejandro H Strachan and other Thesis/Dissertation Committee Members Prof. James Caruthers, Prof. R. Byron Pipes and Prof. Jeffrey Youngblood. Thanks a lot for all of their great suggestions on my research progress and I could not achieve this without any of their efforts. I would especially like to acknowledge Alejandro Strachan Research Group at Purdue including current and former group members Dr. Chunyu Li, Dr. Benjamin Haley, Dr. Md Mahbubul Islam, Dr. Karthik Guda Vishnu, Dr. Saaketh Desai, Dr. Mitch Wood, Dr. Lorena Alzate-Vargas, Dr. Kiettipong Banlusan, Dr. David Guzman, Dr. Sam Reeve, Michael Sakano, Brenden W Hamilton, Shivam Tripathi, Pilsun Yoo, Zachary D. McClure, Timothy Wolfe, Juan Carlos Verduzco Gastelum, Saswat Mishra and Shukai Yao. Also, Dr. Jessica Nash from the Molecular Sciences Software Institute (MolSSI), with whom I developed PolymerXtal (Polymer Crystal Structure Generator and Analysis Software). My mentor Dr. Muhammad Masuduzzaman and supervisor Deepanshu Dutta at Western Digital are also greatly acknowledged.

Research works reported in this book were sponsored by the Institute for Advanced Composites Manufacturing Innovation - The Composites Institute under the Design Modeling and Simulation Technology Area at Purdue University, the Boeing Co. and the U.S. Office of Naval Research, Multidisciplinary University Research Initiatives (MURI) Program, Contract No. N00014-16-1-2557. We thank program managers Chad Stoltz and Kenny Lipkowitz. Computational support from nanoHUB and Purdue University are gratefully acknowledged.

TABLE OF CONTENTS

LIST OF TABLES

LIST OF FIGURES

ABSTRACT

Polymer materials are receiving increased attention in the field of materials science, both in academia and industry, with its widespread application from commercial plastics to advanced biomaterials. These include composites in airplanes and automobiles, functional films on monitors in mobile phones and computers, as well as adhesive and coating materials in civil engineering. Despite significate efforts, the major questions and challenges in understanding key properties of polymer materials are still not solved. Such lack of understanding hinders advances in delicate design and controlling of polymers for advanced functional applications. The development of polymer science began with the pioneering work made by Flory and his coworkers at 1950s as commercial synthetic polymer industry started to develop and grow. During the following decades, experimental work guided by theoretical predictions had been the major contribution of our further understanding while the great challenges in experimental techniques at molecular level always blurred critical information in polymer materials. With enhanced ability in computational science, simulation starts to become an essential investigation method to provide thermodynamic insights at this molecular level. Along with great progress in properties prediction with improved accuracy, great challenges still exist in modeling processing of polymer systems, especially in accurate description of dynamic evolution incorporated with various processing conditions resulting macroscopic structural changes like carbon fiber processing from polyacrylonitrile (PAN) precursor in which crystalline regions represent more than 55% of the material by volume. In terms of crystallinity in polymers, with the heated debates over classical crystal-growth models, major questions and challenges are still not solved including the control and determination of molecular conformations and crystal structures as well as mesoscale morphologies, detailed understanding of melting and crystallization. It is clear that molecular scale investigations on crystal structure and crystallization mechanisms as well as predictive simulations of that will be a huge demand in the near future to explore mechanical, optical, and other physical properties in polymeric materials.

The purpose of my dissertation is to summarize my major research contributions to our current understanding of crystalline polymers in the aspects of crystal structure determination and crystallization processes at molecular level, and to introduce our effort on simulation software development and indicate possible future directions in the field of molecular modeling of polymer crystals. Three major research topics will be included as the following

1. Crystalline and pseudo-crystalline phases of polyacrylonitrile from molecular dynamics;
2. Novel mode of non-crystallographic branching in the initial stages of polymer fibril growth;
3. Polymer crystal structure generator and analysis software (PolymerXtal).

1. INTRODUCTION

Crystal structure and crystallization of polymers are important field of scientific investigation due to broad industrial applications. The world's most popular synthetic polymer, in terms of volume produced per year, is polyethylene (PE) which can crystallize. Other high-volume polymers such as isotactic polypropylene (PP), poly(hexamethylene adipamide) (Nylon 6,6), and poly(ethylene terephthalate) (PET) crystallize, as do many specialty materials, such as poly(tetrafluoroethylene) (Teflon) and poly(p-phenylene terephthalamide) (Kevlar). In general, crystallinity conveys has enhanced mechanical strength, greater resistance to degradation and better barrier properties. While, understanding and analyzing crystalline polymers, either on the perspective of the structure and morphology or on the kinetics and processing during crystallization, has been restricted by some of the issues and remains a big challenge. [1] The purpose of this chapter is to introduce some important topics in this field based on my own research experience. In the following section, I will briefly introduce carbon fiber processing from polyacrylonitrile precursor in which crystalline regions represent more than 55% of the material by volume, followed by Sec. 1.2 with current understanding of spherulites formation during polymer crystallization.

1.1 Processing of polyacrylonitrile (PAN)-based carbon fiber

Carbon fibers (CFs) are an important class of engineering materials due to their light weight, high stiffness and strength [2]. They are used in a range of applications from civil infrastructure to aerospace [3]. PAN-based, cellulose-based and pitch-based CFs are commonly used commercial fibers distinguished by their precursors. PAN-based CFs have been investigated for many years due to their outstanding mechanical performance and supports more than 90% of commercial carbon fiber production. [4] Figure 1.1 shows comparison of Young's modulus and tensile strength with density among forms, polymers, metals, alloys and PAN CFs.

Recent industry efforts focused on reducing the material cost of the CF, which currently limit the use of CF in automotive industry, and current target is $5/lb to make carbon fiber-based cars more competitive with steel cars, see Figure 1.2. Detailed CF cost breakdown, see Figure 1.3

and Table 1.1, shows that CF costs are primarily driven by its manufacture and precursors occupy more than 50% of the manufacturing costs.

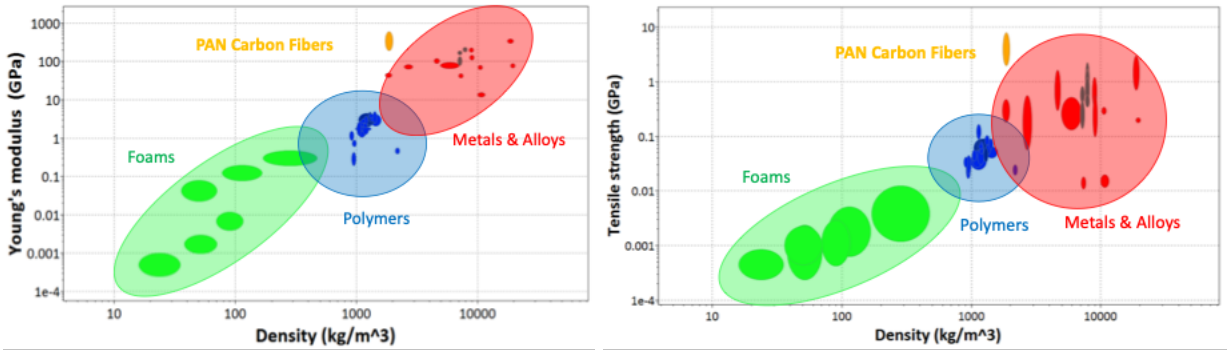

Figure 1.1. Comparison of Young's modulus and tensile strength with density among forms, polymers, metals, alloys and PAN CFs. (Image Credits: Saaketh Desai)

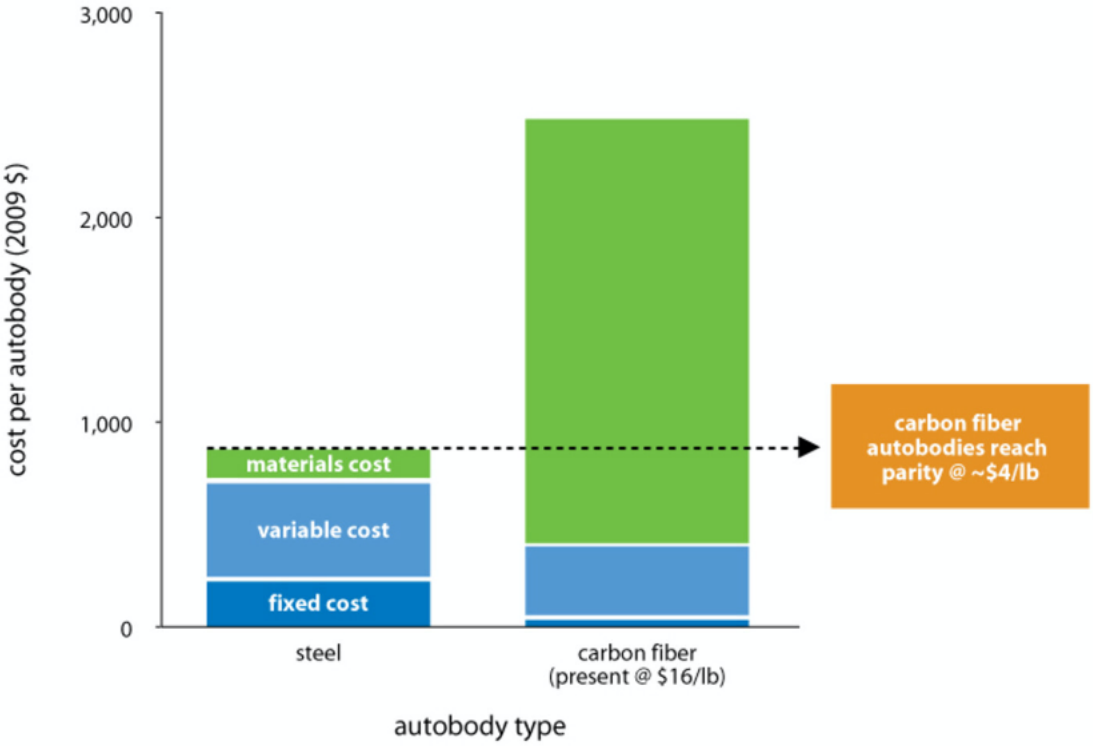

Figure 1.2. Comparison of CF vs. steel manufacturing costs. *Rocky Mountain Institute © 2011*

Processing of these fibers starts with spinning PAN or a PAN-based co-polymer into fibers, followed by a series steps involving oxidation and stabilization, carbonization, and graphitization

under stretching [5–8]. The brief discussion of these process steps is given in the following paragraphs.

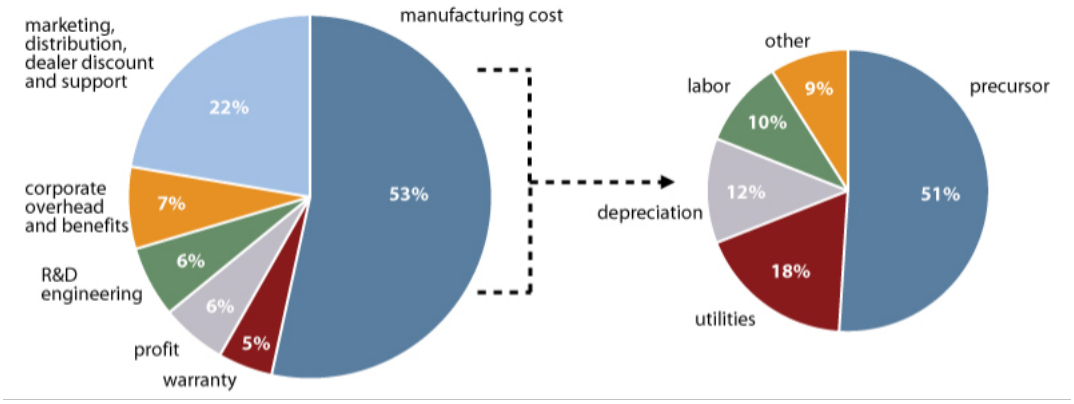

Figure 1.3. CF cost break down. Left: total costs; right: manufacturing costs. *Rocky Mountain Institute © 2011*

Table 1.1. CF manufacturing costs through a standard manufacturing process. *Rocky Mountain Institute © 2011*

	precursors	stabilization & oxidation	carbonization/graphitization	surface treatment	spooling & packaging
baseline cost per pound	$5.04	$1.54	$2.32	$0.37	$0.61

1.1.1 Spinning

Most commercial PAN fiber precursors are produced through wet-spinning and this method has recently been replaced by dry jet wet spinning. The purpose of spinning is to generate fibers with even cross-sectional area, achieve a high level of molecular alignment and reduce the surface defects for the final products. The resulting molecular structure of the spun fibers is critical for the following processing steps, such as oxidation and stabilization [9] that involves cyclization, dehydrogenation, and oxidation reactions [10], and the ultimate properties of the final fibers [11]. Figure 1.4 compares Young's modulus of the final CF with those of the precursors. Fiber spinning remains an active area of research. Attempts by using gel-spinning to produce PAN fiber precursors proves that gel-spun PAN fiber has less core-skin differences and defects and results better molecular orientations and forms better crystalline in PAN fiber precursors [12]. L. Tian

and D. Pan further proved that gel-spun PAN fiber has better mechanical properties than wet-spun fiber [13]. CFs processed from gel spun precursor are considered to have best mechanical performance with the highest combination of modulus and strength [14]. Effects of stretching during spinning have also been investigated, see Figure 1.4.

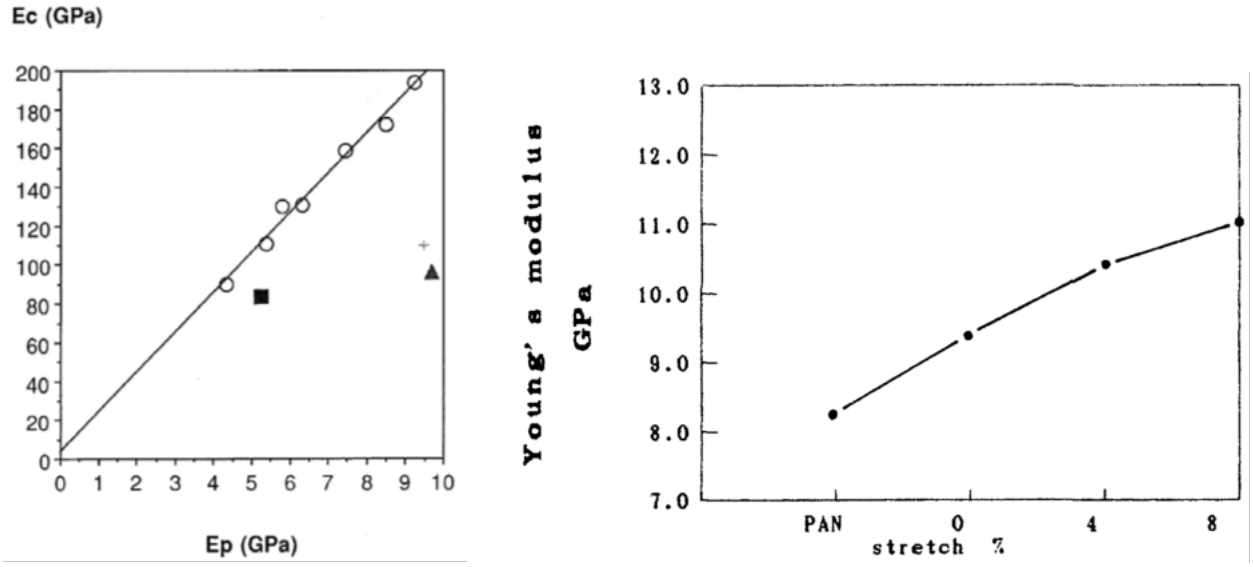

Figure 1.4. Left: properties of individual fibers extracted from drawn tows compared to original Ec (Young's modulus of CF) vs. Ep (Young's modulus of precursor). Figure adapted from Ref. [15]. Right: Variation of the Young's modulus of the PAN precursor with the stretch ratio. Figure adapted from Ref. [16]

1.1.2 Stabilization

In this stage, PAN precursors are treated in air at 180-300°C under tension to avoid the shrinkage of the polymer chains [5,17]. During stabilization, the PAN precursors chains are physically unfolded and mainly undergo three types of chemical reaction: oxidation, dehydrogenation and cyclization [5]. C≡N converts to C=N with N atoms connected to adjacent C atoms to form ring structure [18] and some of H atoms are eliminated in the form of HCN, H_2O and NH_3 [19]. Stabilization, usually taking 2 hours to finish, is the most expensive and time-consuming process [17] as well as the most complicated reaction process with a lot of controversies. Figure 1.5 summarizes several hypothesis of reaction mechanism and chemical structure after stabilization [6]. Several factors which may affect the structure and properties of stabilized fibers includes the content of copolymer, heating temperature, heat rate, airflow rate,

method of stabilization process (batch process, continuous process, and accelerator process [18]), stretching ratio and prestabilization treatment (polymerization and spinning).

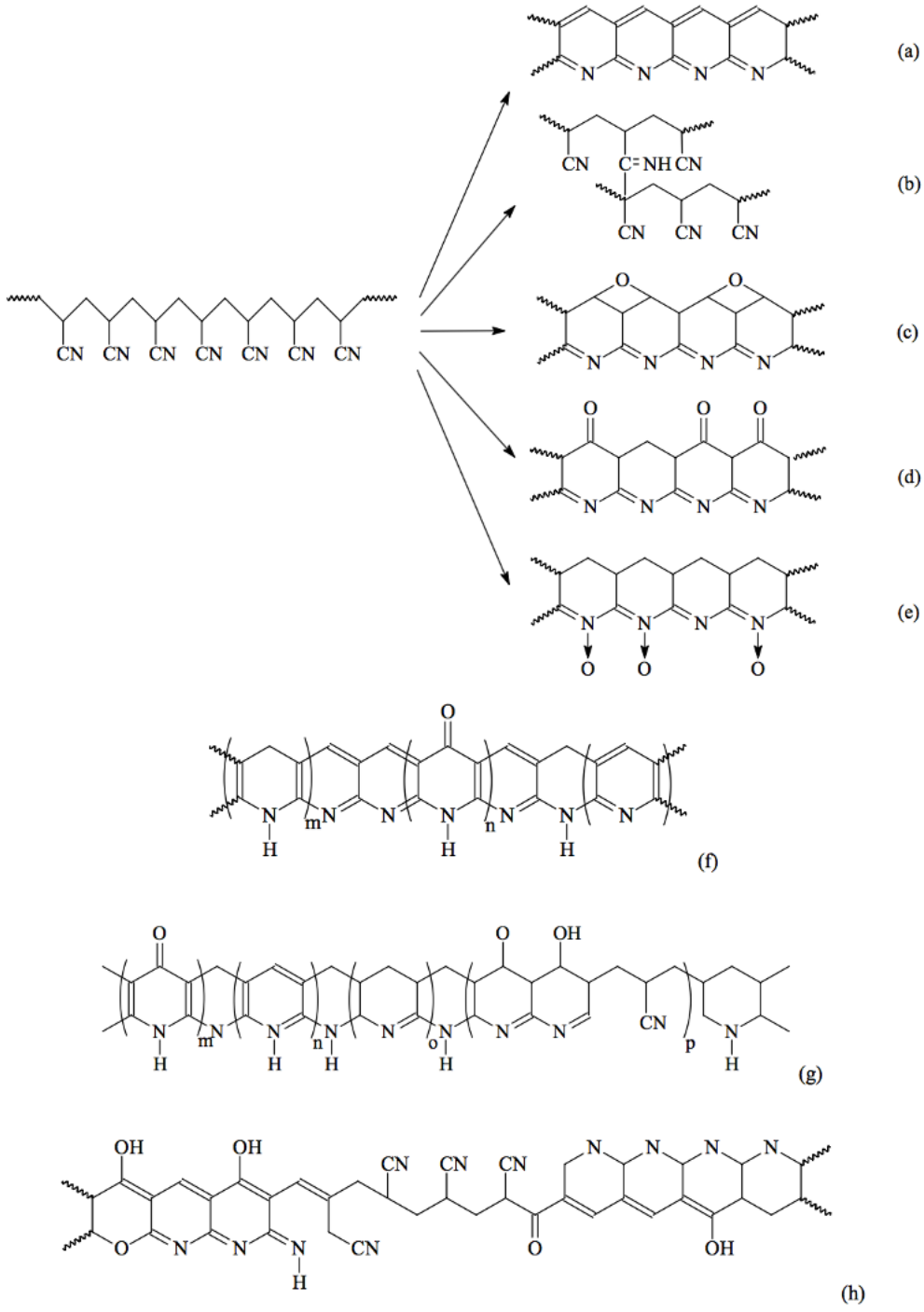

Figure 1.5. Oxidization of PAN, figure adapted from Ref. [6].

1.1.3 Carbonization

Carbonization process usually happens between 800 and 3000°C within an inert atmosphere containing only N_2 gas [20]. The cyclized PAN structure starts with intermolecular dehydrogenation and denitrogenation. Therefore, the stabilized PAN fiber chains are cross-linked and form basal planes along the axis. Further growth along the dimensions of these basal planes rearranges the microstructure and decreases the carbon fiber diameter. [21] Another reason of the reduction of fiber diameter is the elimination of non-carbon elements. H, N and O are eliminated as volatile gases like CH_4, H_2, N_2, HCN, H_2O, CO, CO_2, NH_3 and various other gases during this stage. Pre-carbonization process is applied to avoid the sudden heat releasing which can caused defects in fiber structures. This preliminary treatment uses low temperature at 300-700°C and can greatly improve the Young's modulus of the final structure. [22] Heating rate also affects the strength of the fiber, fast heating would cause defects in the micro structure and too low rate would affect the early stage and result huge loss of nitrogen which plays an important role in the rearrangement of basal planes [6]. Typical properties after carbonization are illustrated in Table 1.2 [17].

Table 1.2. The comparison of typical properties between carbonized and graphitized fibers. Table reproduced from Ref. [17].

Typical Properties	Carbonized Fiber	Graphitized Fiber
Modulus	200-300 GPa	500-600 GPa
Compressive Strength	~3 GPa	1 GPa
Shear Modulus	~15 GPa	10 GPa
Diameter	5-7 µm	5-7 µm
Electrical Conductivity	50,000 S/m	100,000 S/m
Thermal Conductivity	<10 W m^{-1} K^{-1}	<50 W m^{-1} K^{-1}

1.1.4 Graphitization

At this stage, carbon fibers are treated at more than 3000°C under Argon environment [23]. Highly ordered carbon structures are largely growing both at the in-plane area and the thickness. More than 99 % of the carbonized fibers are finally converted into graphite structure. [5] Figure 1.6 shows the structure evolution from stabilized fiber to the final graphite like structure [24].

PAN precursor structure is known to critically affect final CF microstructure and consequently properties. While, studies on precursor morphology are still not sufficient, especially

on topics regarding spinning temperature, spinning rate, copolymer type and stereoregularity [25]. Due to the complexity of the atomic-level processes involved in the processing of CFs that are believed to be critical in determining microstructure, molecular simulations would be an ideal complement to experimental efforts. These simulations are a promising tool to understand and eventually control the processing of carbon fibers in order to yield product with better properties. While, because of the long relaxation time of high molecular weight polymers compared with the short time range of molecular dynamics (MD) simulation, the PAN precursor molecular structure in simulation has not yet been produced. In Ch. 3, I will present our efforts on understanding the structure of PAN fibers using MD simulations.

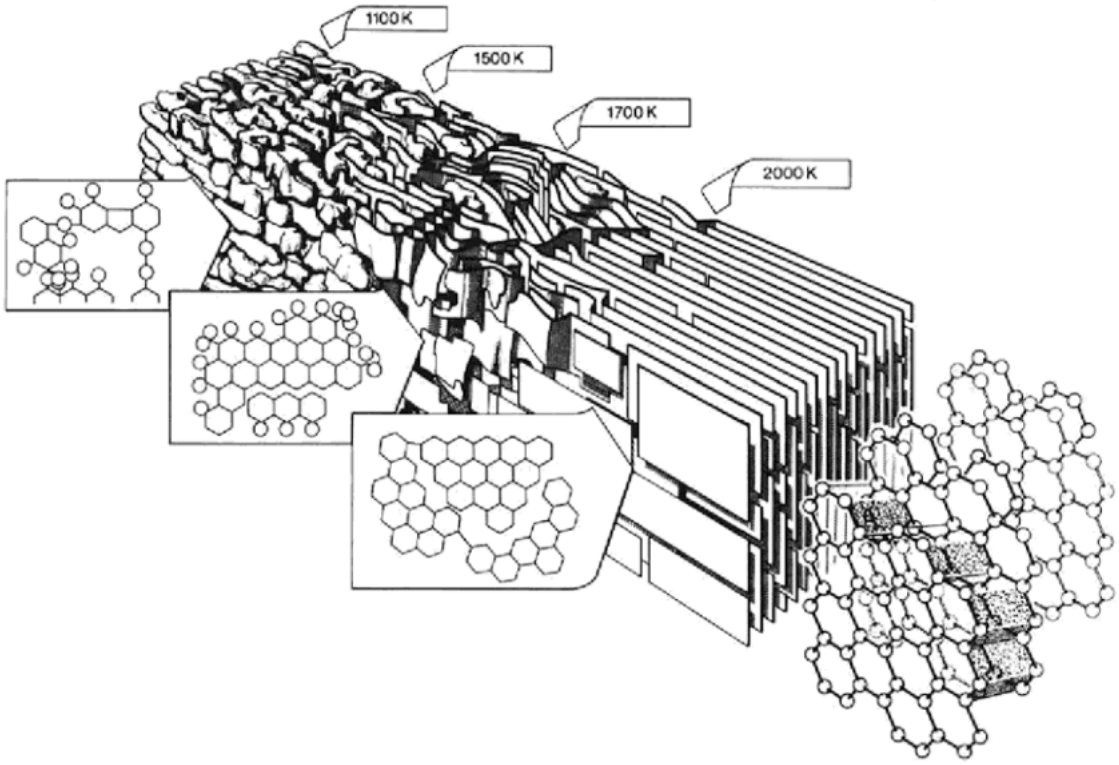

Figure 1.6. Marsh-Griffiths model of carbonisation/graphitisation process, figure adapted from Ref. [24].

1.2 Polymer spherulites

Spherulites are the most ubiquitous of polycrystalline microstructures, they develop by the subsequent branching of crystalline lamella that results in an overall spherical shape. Three levels

of polymer spherulite structure are illustrated in Figure 1.7. On the first level, individual chain backbones form helices (of which an all-trans conformation is a special case), and pack with neighboring chains to form unit cells. The typical unit cell contains only a few monomers, and has dimensions of 2–20 Å on a side. On the second level, unit cells pack into thin sheets, called lamellae, which are typically 100–500 Å thick and several microns wide in the other two dimensions. The chain backbones lie at some fixed angle relative to the thin direction, and often fold by 180° at the lamella surface in order to reenter the crystal. Chain-folded lamellae, illustrated in Figure 1.7, are a unique morphological feature of polymers. Finally, in a bulk sample the lamellae grow to fill space, often producing a three-dimensional spherulite structure which can be tens or hundreds of microns across. [26] Spherulites form not just in polymers [27–36] but in a wide range of materials, like elemental selenium [37,38], oxide and metallic glasses [39], mineral and volcanic rocks [40] and biological molecules [41], upon crystallization from the melt, solid, or solution and their microstructural details have a strong effect on materials properties [42]. Thus, there is significant interest in understanding and controlling their formation [43,44].

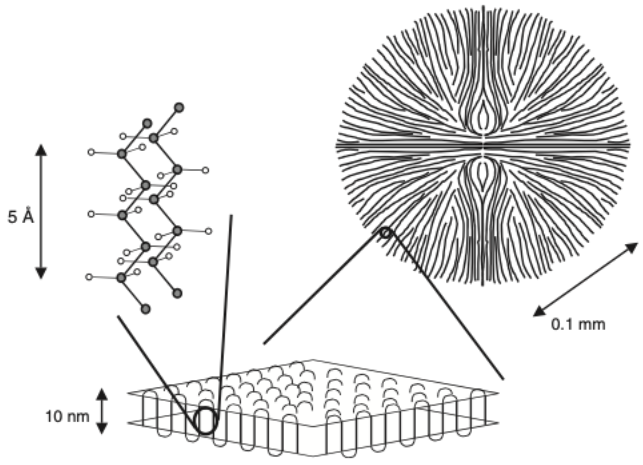

Figure 1.7. Three levels of polymer spherulite structure. Figure adapted from Ref. [26].

The name, spherulite, originates from the nearly spherical shapes they exhibit before impinging into each other or with other boundaries [42]. Since the first report in 1837 that spherical crystals crystallize in borax ($Na_2B_4O_7 \bullet 10H_2O$) from a drop of phosphoric acid [45,46], their fascinating internal microstructure have puzzled researchers. It is well established that their spherical shape originates from the successive branching during the growth of crystallites. In

addition, unlike other polycrystalline structures (such as snowflakes and dendrites) where branches are formed along crystallographic habits, the core of spherulites is non-crystallographic branching [42].

Spherulites appear in disparate materials and their formation, as in the case of phase separation, is remarkably insensitive to molecular structure which hints at a common underlying process. While some explanation is required regarding a more common appearance of spherulite crystallization patterns in polymers. Magill has noted [47] that the viscosity of the incipiently crystallizing materials which form spherulites becomes as large as 30 Pa·s to 50 Pa·s, which seems to implicate glassy dynamics in the phenomenon, although spherulites have been observed when trying to crystallize materials in a gel or other highly disordered matrix [48,49]. Therefore, the relaxation dynamics of the undercooled liquid should be slow compared to the nucleation rates, and growth should outpace nucleation.

1.2.1 Formation of fibrous crystals

One of the universal crystal growth habits underlying spherulite formation in diverse material is the general tendency to form needle-like crystals and explaining the general tendency has gone a long way to providing a fundamental understanding of spherulite growth. MD simulations of crystalline Ni have indicated that the mobility on different crystallographic interfaces of this material can differ by orders of magnitude [50], providing a rationale for the kinetic anisotropy implicit in the phase field simulations [51].

In polymers, there is significant consensus regarding the mechanisms of chain folding, see Figure 1.8, led by a faster intramolecular nucleation path where stems are added to the front growth, reach a critical value for stability, and grow until the overall thickness of the lamella is reached. It is well established that fibrous crystals involve folding chains into lamellae with thickness in the 5-35 nm range which ultimately results in a metastable, semi-crystalline microstructures [52].

1.2.2 Non-crystallographic branching (NCB)

To account for spherulitic crystallization in polymers, one must not only explain the formation of fibrils but also the mechanisms behind profuse NCB [53,54]. NCB was postulated by Keith and Padden in the 1960s [53,55–60] based on geometrical considerations and several

mechanisms have been proposed to explain it. Branching in NCB occurs with small misorientations relative to the primary nucleus and results in the growth of subsidiary lamellae. This common mechanism is believed to underlie the similar morphologies observed in materials with disparate atomic or molecular structures.

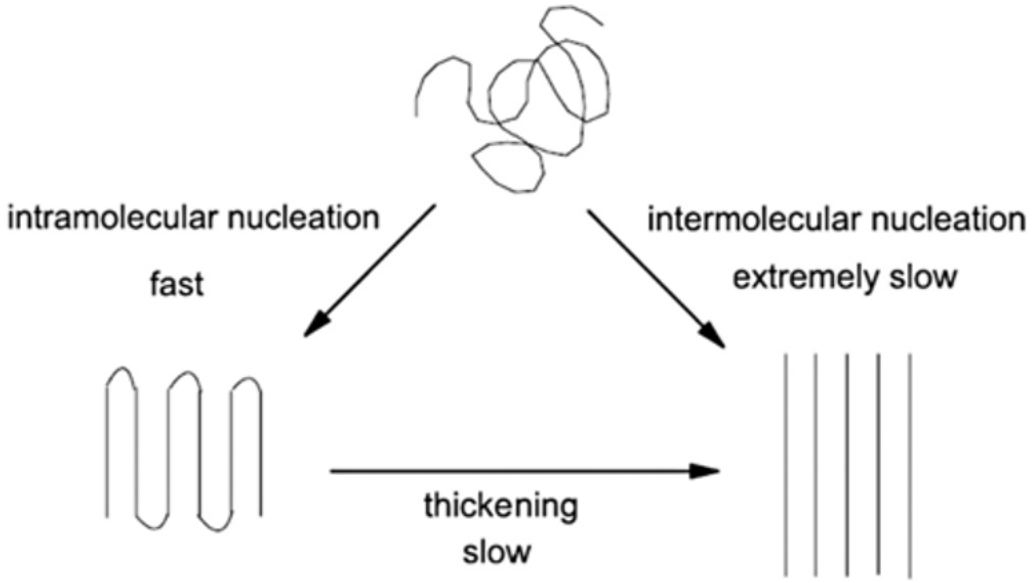

Figure 1.8. Illustration of principle of chain-folding during polymer crystallization. Figure adapted from Ref. [61].

Recent progress on mesoscale simulations by Gránásy that incorporate *ad hoc* rules for NCB showed that heterogeneity in liquids, either in the form of impurities or additives, or the inherent dynamic heterogeneity of cooled liquids plays a role of both in the prevalence for crystal nucleation and secondary nucleation in crystallizing materials and its associated NCB in spherulitic growth. These models build on expressions of the free energy for polycrystalline systems and describe the independent relaxation of the various fields. While, specifications of a free energy density in terms of order parameters relevant to a particular material and mobilities relevant to the positional and orientational order parameters in terms of which the free energy is expressed are required. [54] This is the current shortcoming of phase field theory and extensive MD simulations are required to validate these free energy expressions. Basically, these simulations assumed that a basic property of glass-forming liquid was responsible for the NCB, and in

particular, this property was attributed to the relative anisotropy between rotational and translational mobility, i.e., "decoupling". In other words, decoupling between translation and rotational modes has been shown to result in branching and to control the resulting polycrystalline structure. There is extensive experimental data supporting this picture [49,51], both in terms of the relatively universal occurrence of spherulite structure formation and the progressive change from symmetric crystal, dendritic to spherulitic crystallographic branching with increasing cooling almost regardless of the chemical makeup of the crystallographic material.

While NCB is believed to be the common underlying process across materials classes, its molecular origin is material-dependent and remains poorly understood. In the case of atomic materials and molecular crystals, there is evidence of crystal inhomogeneities [62,63], dislocation structures [37,63–66] and stress [67] playing a role in NCB. In polymeric systems, impurities and self-catalytic processes [68,69] can result in the instability of a growing crystallite, for example the segregation of impurities can depress the local melting temperature and change the growth direction [53]. However, the observation of spherulites in pure systems [37,38,47,70–72] indicates that these mechanisms are not expected to be dominant in polymers [42].

Autodeformation mechanism. Based on the crystal split and spherulite growth in minerals, Punin proposed the concept of self-deformation, aimed to develop a universal of spherulitic growth [73]. In the past few years, Kniep with colleagues [74–77] developed an electric field-induced growth mechanism for gelatin-grown apatite spherulites grown from gelatin based on the concept of autodeformation. If the crystalline phase is polar, the electric field induced by a growing crystallite can result in the orientation in the material in the amorphous region along the electric field lines and cause branching [78]. This model was also applied to zinc oxide [79], see Figure 1.9.

Tip splitting. Originally proposed by Keith, H. D., and F. J. Padden Jr, interface instability can generate two lamellae from one, and lead to low-angle NCB [53]. This concept was later perfected by Toda et al. as illustrated in Figure 1.10 [80]. Unstable interface leads to bifurcation of the growth front when the crystal width W achieves a width $W \approx \lambda = \lambda_c$, where λ_c is the critical wavelength of an interface perturbation. It is assumed that the adjacent protrusions will increase in length and width, and overlap as the width of each protrusion increases, thereby forming a topological giant screw dislocation. The process repeats itself when each new protrusion reaches width λ_c after growing radially by $g\lambda_c$, where $g > 0$. [81] Lamellar divergence may be due to the

spatial repulsion near the pinning point, as Bassett suggested for spiral growths [82]. It has been observed in dendritic polymer crystals grown in dilute solution for decades that topologically huge screw dislocations has been formed by twisting the Δθ angle as proposed in Figure 1.10 [83].

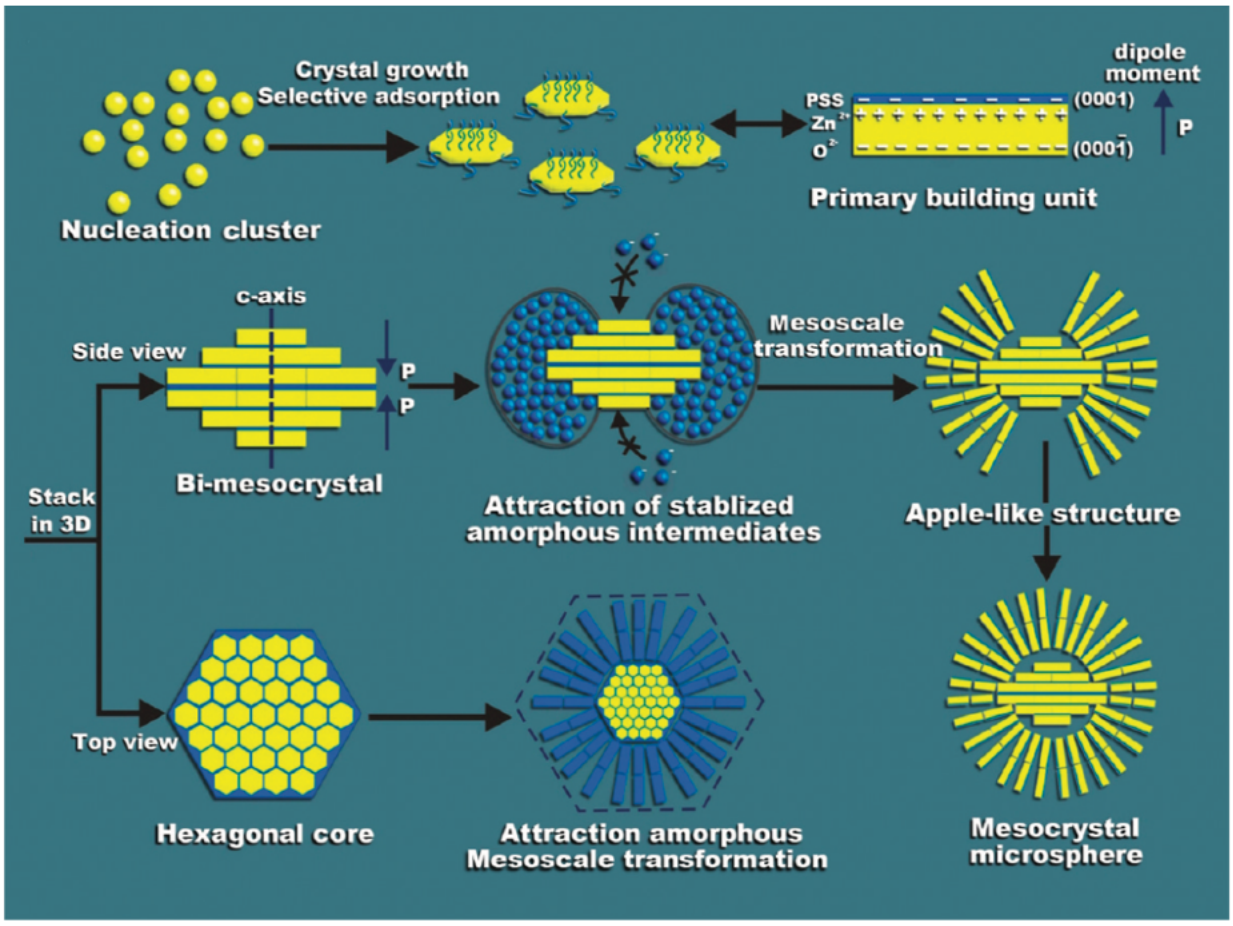

Figure 1.9. Schematic illustration of the growth model for intrinsic dipole-field-driven mesoscale crystallization of core-shell ZnO mesocrystal microspheres. Figure adapted from Ref. [79].

Induced nucleation is one speculation of spherulite formation mechanism specific to polymers. Chains ends or loops dangling from a crystal have been postulated to act as nucleation sites for subsidiary lamellae which branch at small, non-crystallographic angles, as sketched in Figure 1.11 [42,84,85]. Recent characterization of crystallization in thin polymeric films using AFM identified the nucleation of secondary lamella adjacent to a pre-existing ones [85,86], but the resolution is not enough to provide a molecular-level mechanism. Another AFM study on polymer monolayers provided insight into the early stages of growth of individual lamella,

indicating non-monotonous rates and correlated induced nucleation [87]; yet, the molecular mechanisms underlying branching remain obscure.

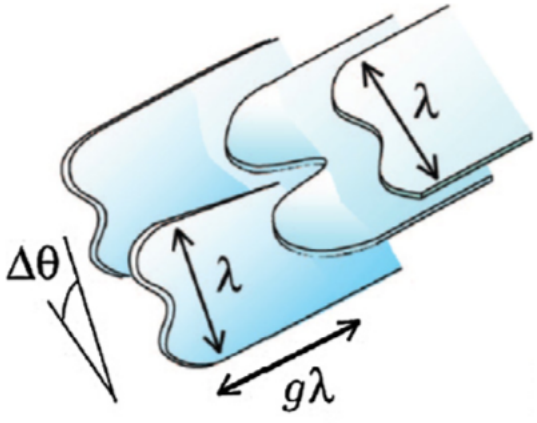

Figure 1.10. Conceptual sketch of branching via a topological giant screw dislocation with protrusions formed by interface instability when the crystal achieves a width $W \approx \lambda = \lambda_c$. Figure adapted from Ref. [81].

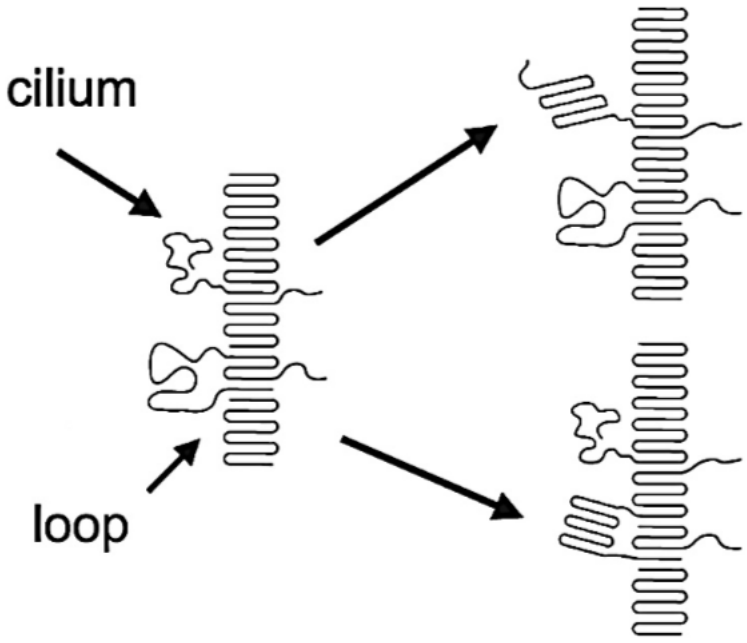

Figure 1.11. Illustration of induced nucleation. Figure adapted from Ref. [79].

MD simulations are, in principle, ideally suited to characterize the processes underlying NCB but very little MD modeling has yet been performed on polymer materials. During the next chapter, I will introduce the basic theory of MD and its application on polymer materials.

2. THEORY AND METHODS

The influence of molecular modeling and simulation has increased as an important auxiliary tool to determine the helical structure in static structure analysis. At the same time, molecular simulation as a means of analyzing the dynamic process that occurs in polymer crystallization seems to be more restricted at present. Due to flexible and complex molecular shapes, polymer crystals are usually far away from thermodynamic equilibrium, and their crystallization occurs in a metastable state of deep subcooling, involving not only enthalpy but also entropy-driven processes. In the current molecular simulation research, generating or even simply reproducing cr process is also a challenging topic. In addition, polymer crystallization depends on short-range interactions, mainly van der Waals forces, but long-range order occurs. The need of detailed short-range structure complexity analysis is also underlined for any long-range order investigations. [1] In this chapter, I will introduce the basic method of molecular dynamics as implemented with the LAMMPS [88] framework and a general-purpose force field DREIDING [89], as well as its application on a wide range of polymers.

2.1 Molecular dynamics (MD)

MD classically evolves the position and momentum of each particle via Newtonian dynamics

$$\vec{F_i} = m_i\vec{a_i} = -\nabla_r V(r_i) \tag{2.1}$$

$$\dot{\vec{p}} = \vec{F} \tag{2.2}$$

$$\dot{\vec{r}} = \frac{\vec{p}}{m} \tag{2.3}$$

which can be reformulated into Hamiltonian dynamics as such:

$$H(r_i,p_i) = \sum_{i=0}^{3N} \frac{p_i(t)^2}{2m_i} + V(r_i) \tag{2.4}$$

$$\dot{r}_i = \frac{\partial H}{\partial p_i} \tag{2.5}$$

$$\dot{p}_i = \frac{\partial H}{\partial r_i} \tag{2.6}$$

where V(r) is determined by an interatomic potential model and time integration utilizes a Verlet algorithm.

2.2 Force field

The potential used here is DREIDING [89] force field which can provide semi-quantitative predictions of a wide range of polymers and thermo-mechanical properties [90–92]. In this force field, each atom interacts through bonding and non-bonding potentials. The bond stretching potential between two adjacent atoms is

$$E_{bond} = k_l(l - l_0)^2 \tag{2.7}$$

where l is the length of bond, k_l is the bond stretching constant. The bond angle bending potential between three adjacent atoms is

$$E_{angle} = k_\theta(\theta - \theta_0)^2 \tag{2.8}$$

where θ is the complement of the bond angle, k_θ is the angle-bending constant. The bond twisting potential between four adjacent atoms is

$$E_{torsion} = k_\varphi(1 + \cos n\varphi) \tag{2.9}$$

where φ is the torsion angle, k_φ is the torsion constant and n is an integer varying based on different type of covalent bonding.

Lennard-Jones 12-6 potential describes all intermolecular interactions between atoms in different chains and intramolecular interactions between atoms in the same chain separated by four or more bonds,

$$E_{EJ} = 4\varepsilon[\left(\frac{\sigma}{r}\right)^{12} - \left(\frac{\sigma}{r}\right)^{6}] \quad (2.10)$$

where ε is the strength factor for interatomic interaction and σ is the size factor.

2.3 Molecular modeling of polymer crystallization

Prior MD simulations contributed to the molecular understanding of the formation and growth of chain folded lamella in polymers [93–95], the mechanism behind chain folding and thickening associated with grain growth, and the effect of molecular weight and temperature [96–102]. The growth pathway of individual lamellar crystals has been tracked in MD showed that there are the two main kinetic processes during polymer crystallization into formation of chain folded lamella. The fast path of crystal growth selects the intramolecular mode of secondary crystal nucleation. Therefore, the chain folding process inhibits crystal growth along the chain axis, resulting in layered crystals. The latter then gradually thickened to form stable extended chain crystals. [61]

Studies focusing on homogeneous nucleation [100] show that the nucleation rate is not sensitive to chain length, and the critical nucleus is significantly smaller than the radius of gyration of the chain. The MD characterization of single crystal growth [97] also shows that the length of the loops is widely distributed, which supports the "switchboard model" of early crystals formed under deep subcooling conditions.

Unlike continuum models of crystallization, MD describes crystallization by explicitly modeling the temporal evolution of each individual atom in a material without any assumptions regarding mechanisms of crystal growth, secondary nucleation, spontaneous nucleation, or induced nucleation. In Ch. 4, I will also introduce our efforts on molecular modeling of polymer crystallization and show how atomistic simulations of polyethylene (PE) crystallization reveal the molecular-level origin of this non-crystallographic branching (NCB).

2.4 Molecular modeling of polymer structures

The determination of polymer structure relies on a comprehensive set of techniques, including X-ray diffraction and nuclear magnetic resonance spectroscopy [1]. In this section, I will

review the experimental literature on the characterization of crystal structure determination as well as their underlying theory, followed by introductions of molecular modeling of polymer structures, both amorphous and crystalline, using MD methods.

2.4.1 Characterization of crystal structure determination

X-ray Diffraction (XRD) has been widely used to determine the crystal structure of solids, including unit cell, geometry, crystal orientation and defect detection [103]. The mechanism is based on the Bragg's Law:

$$\lambda = 2d \sin\theta \tag{2.11}$$

With a crystal plane model like Figure 2.1(a) [26], Bragg's law can be rewritten as:

$$m\lambda = 2D \sin\frac{\theta}{2} \tag{2.12}$$

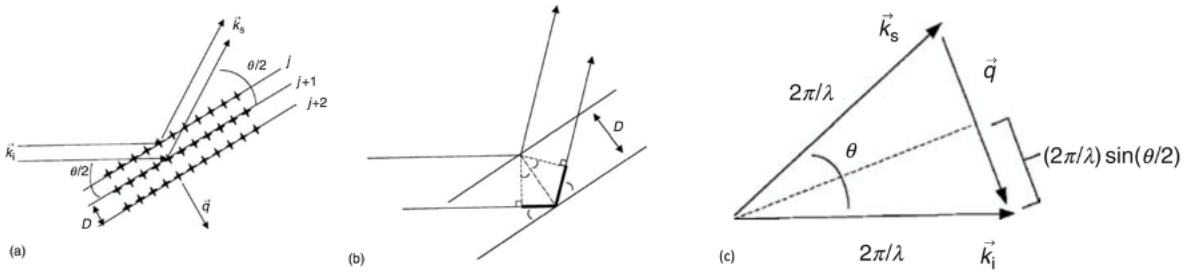

Figure 2.1. Illustration of Bragg's law. (a) The incident light wave and the diffracted light wave each makes an angle $\theta/2$ with each plane in the crystal. The planes are separated by a distance D, and the direction of the scattering vector $\vec{q}$ is indicated. (b) The bold line segments correspond to the extra distance the wave travels in being scattered from the second plane. All four indicated angles are equal to $\theta/2$, and thus each of the bold line segments has length $D \sin\theta/2$. (c) the length of the scattering vector is calculated in terms of the scattering angle θ and the magnitude of the incident and scattered wavevectors, $2\pi/\lambda$. Figure adapted from Ref. [26].

The scattering vector $\vec{q}$ is defined as

$$\vec{q} \equiv \vec{k_i} - \vec{k_s} \tag{2.13}$$

where $\vec{k_i}$ is the incoming wave vector and $\vec{k_s}$ is the scattered vector. The relationship between $\vec{q}$ and scattering angle θ can be derived as following based on Figure 2.1(c):

$$|\vec{q}| \equiv q = 2\left(\frac{2\pi}{\lambda}\right)\sin\left(\frac{\theta}{2}\right) = \frac{4\pi}{\lambda}\sin\left(\frac{\theta}{2}\right) \tag{2.14}$$

In XRD experiment, a beam of X-ray which contains single wave length light is scattered by the polycrystalline sample. The detector can be either 1-dimensional or 2-dimemsional, while the second one has been used more frequently as the demand increases and the detection technique has been increasingly improved. Based on the mechanism illustrated above, single crystal is preferred when using XRD to determine the unit cell parameters. Not only the scattering sample itself, the choice of orientation towards incoming beam can also determine the results of XRD patterns. Figure 2.2(a) and (b) illustrates the scattering results compared between sheet-like crystal and rod-like crystal where the latter one is proposed as crystal structure of most fiber systems. However, forming polymers into a single crystal structure is extremely difficult especially for those with higher molecular weight. Several endeavors have been made since 1950 by carefully growing the crystal structure from solutions. The compensate strategy widely accepted today is applying drawing before forming the crystal structure, making fiber like structure with long c axis to eliminate the effect of disorder in crystal orientation, therefore the scattering beam can produce better characterization the molecular structure [26].

Because the scattering X-ray is different between elements due to the refractive index which determined by the election density, C, H, O and N which are the most common atom types in polymers are not good scatterers of X-rays. This limitation can be overcome by using synchrotron radiation which can provides a large order greater magnitude with better resolution of the scattering pattern. Another way to improve the quality of scattering pattern is to choose samples with ordered structure in a long range and this method is more commonly used in laboratories.

Radial distribution function (RDF), also known as pair correlation function (PCF), reflects the functional relationship between the probability of occurrence of other particles in any designated "central" particle and the radius r. As shown in Figure 2.3 [104], taking an atom as the center of observation, draw a layer of concentric spherical shells in units of Δr, and then calculate the density of atoms in each shell (particle number n(r) / volume V). Therefore, RDF can be defined as

$$g(r) = \frac{n(r)}{\rho_0 V} \approx \frac{n(r)}{4\pi r^2 \rho_0 \delta r} \tag{2.15}$$

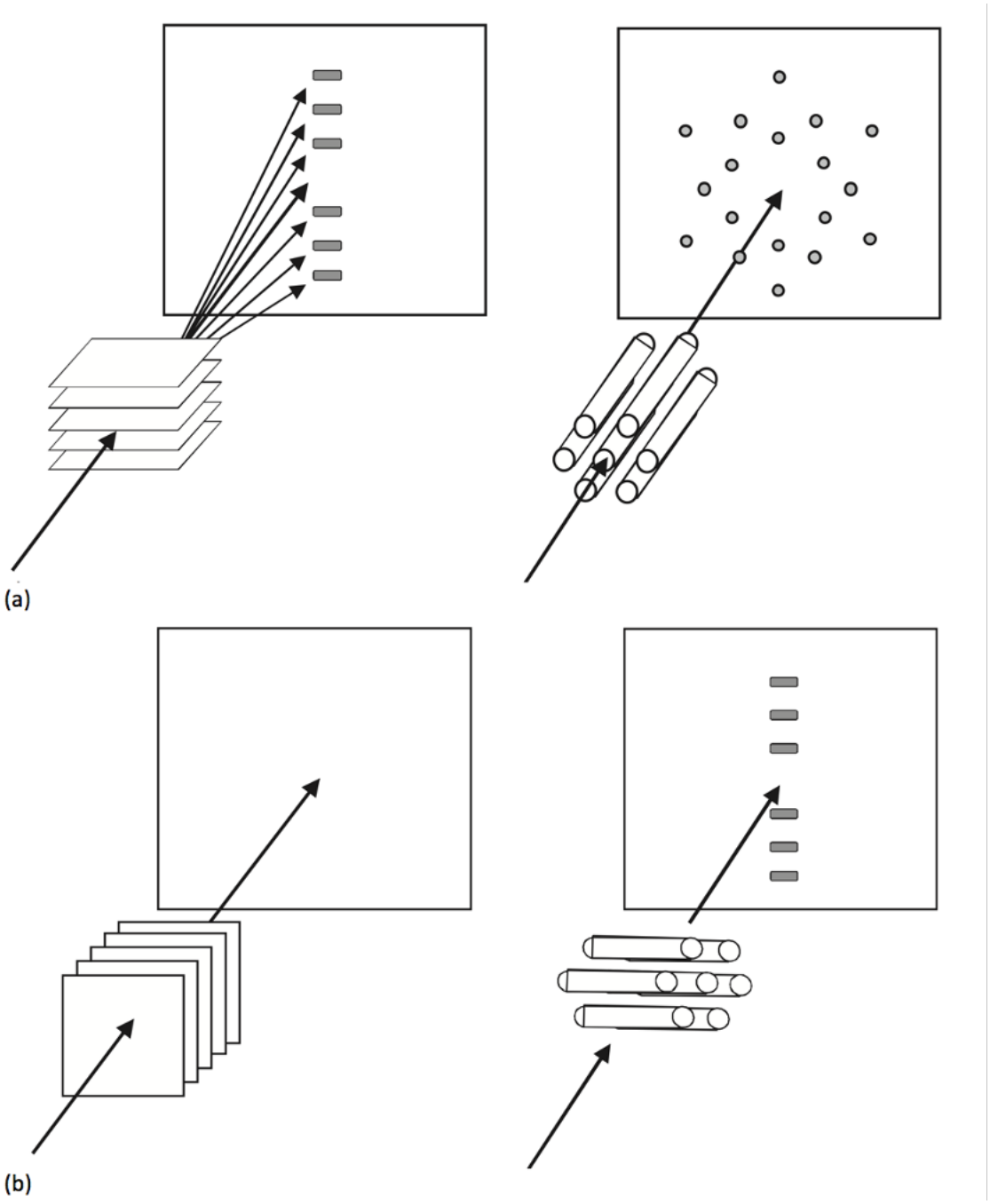

Figure 2.2. Diffraction patterns on an area detector for (a) a set of parallel sheets viewed edge-on, and a hexagonal array of rods viewed end-on and (b) the sheets viewed through and the rods viewed edge-on. Figure adapted from Ref. [26].

where r is the distance to the center of the atom, δr is the shell thickness, n(r) is the number of particles in the sphere, and ρ_0 is the average number density which can be obtained by total number of particles divided by volume.

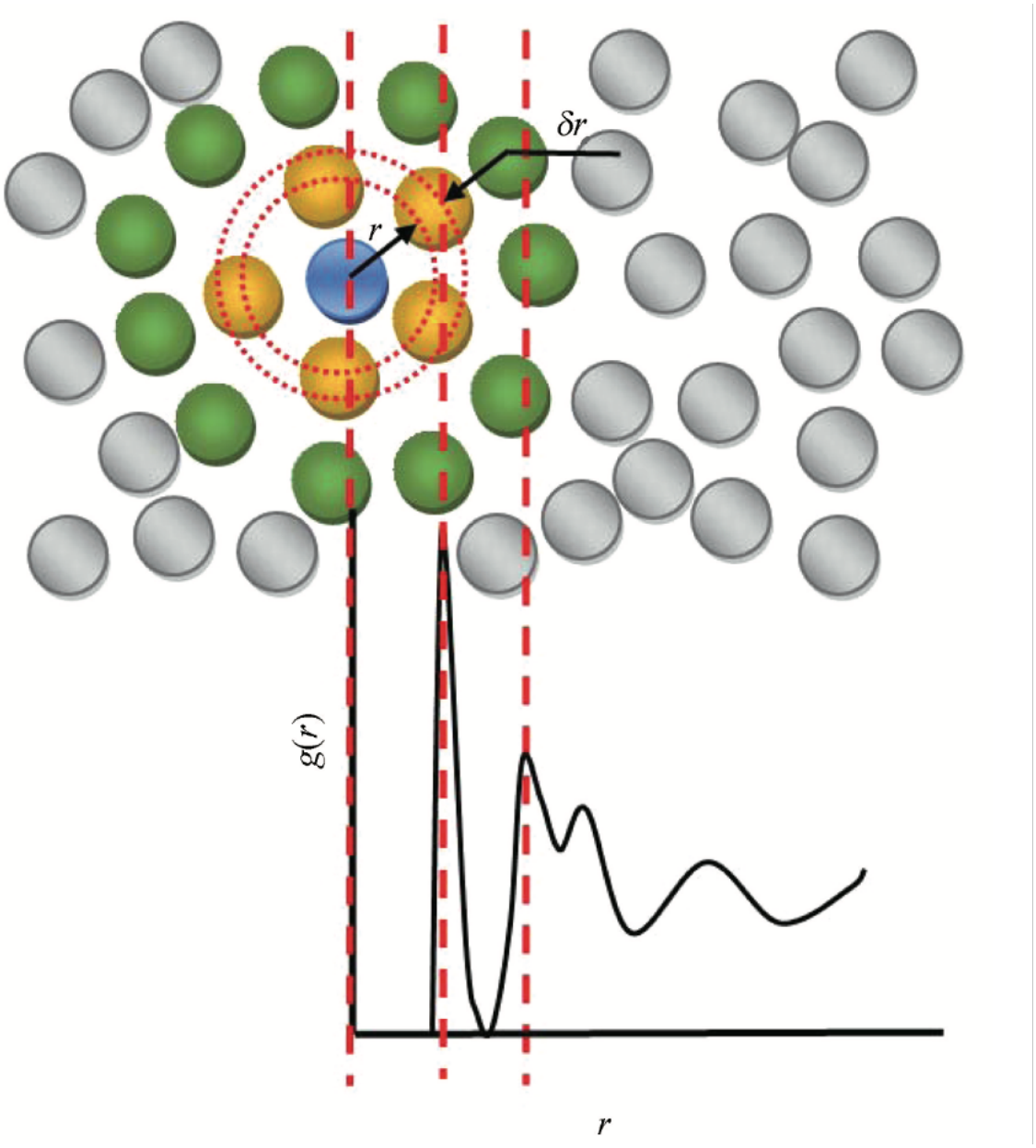

Figure 2.3. Diagram of the relationship between the PDF and the atomic structure. Figure adapted from Ref. [104].

Static structure factor (SSF) is an important bridge to connect the experimental analysis and simulation model of molecular structures. This can be obtained from diffraction intensity by

$$S(q) = \frac{I(q)}{Nf^2(q)} \tag{2.16}$$

where q is defined previously in Eq. (2.14), I(Q) is the diffraction intensity and f(Q) is the correlation factor for different elements and *N* is the atom number of the sample material. S(q) - 1 and g(r) - 1 are connected with each other through Fourier transform (FT), where SSF gives atomic information in reciprocal space while RDF gives that in real space. The three-dimensional FT

$$S(q) - 1 = \int \exp(i\vec{q}\cdot\vec{r})\,\rho[g(r)-1]d\vec{r} \tag{2.17}$$

Because g(r) is a spherically averaged, the three-dimensional variable can be converted into a one-dimensional variable which is only related to the radius r. Thus, Eq. (2.17) is converted to a radius integral FT. The relationship between the structure factor and distribution function can be expressed as

$$S(q) = 1 + 4\pi\rho \int_0^\infty \frac{\sin qr}{qr}[g(r) - 1]r^2 dr \tag{2.18}$$

The analysis of the structure factor is based on the peak position, the shape of the peak.

2.4.2 Molecular modeling of amorphous polymer structures

MD simulation as a complement to experiment effect of investigating polymer structures can give more direct and detailed information about structure evolution and molecular mechanism during heating or cooling process. MD simulation characterizes the space-time high mobility domains of various bulk polymers, thin plates and isolated chains when the liquid sample is cooled during the glass transition process, showing the universality in dynamics of supercooled polymers in nanoscale systems [105]. And these investigations can only be done with a reasonable molecular model, otherwise the simulation cannot provide reliable analysis. However, building an accurate

molecular model for polymers is not as easy as metals or small molecule systems which usually have short relaxation time. Several experimental results showed that the relaxation time of polymers is depend on 3.4 order of the molecular weight [26]. That means if the molecule weight becomes 100 times larger, the relaxation time would be increase about 10^6 times. In that case, simple strategies like melting crystalline structure to amorphous state which can be used for metal liquids becomes time consuming and wasted of computation resources for getting polymer structures [103]. Several specific algorithms must be applied for generating amorphous polymer structure. The following paragraphs introduces *Polymatic* [106] as an example.

Polymatic generation algorithm is based on simulated polymerization and 21-step MD equilibration. Simulated polymerization reaction starts with small molecules (such as monomers or short chains), which are randomly filled into the simulation box. These small molecules can contain 1 or 2 functional groups to form linear structure, or 3 or 4 functional groups to form branched, cross linked or networked structure. This strategy is suited to both single backbone polymers and ladder structure polymers. For those more entangled polymers with high glass transition temperature (T_g), *Polymatic* starts with short chains at low density around 0.1 g/cm^3 with chains are far away from each other. The bonding of simulated polymerization is carefully selected based on the distance of active atoms, spatial alignment and prevention of crosslinking at early stage in which linear polymerization is dominated. This process is followed by minimization to avoid simulation failure caused by sudden energy change. Then, the whole system undergoes 21-step equilibration as demonstrated in Table 2.1 [106].

This algorithm has been exampled by various properties measurements which includes thermal expansion properties, XRD characterization, T_g, density, porosity and gas absorption isotherms. They all show reasonable agreement with the experimental results. Figure 2.4 specifically shows the structure factor comparison between different polymers [106].

2.4.3 Molecular modeling of crystalline polymer structures

MD simulations have also been utilized in several polymer crystalline structure studies. The MD prediction of polyetherketoneketone (PEKK) characterizes the effect of terephthaloyl chloride to isophthaloyl chloride (T/I) on broad properties, including the lattice parameters and the stability of the PEKK crystal structure, and helps clarify inconsistencies of the unit cell in the literature [107]. Several molecular modelling studies have also been carried out to predict the

polyacrylonitrile (PAN) structures including chain conformation [108,109], crystal morphology [110–112] and its stability [109,112]. Conformational energy calculations using PCILO (perturbed configuration interaction with localized orbitals) indicated that due to inter-molecular interactions, single-chain conformations with low energy are not favorable in crystalline regions [108,109]. Simulated XRD studies of PAN imply that the diffuse scattering in equatorial direction are due to the rotational disordered about the chain axes [110]. Therefore, an hexagonal or pseudo-hexagonal packing of rigid-rod polymer structures is generally accepted [110–112].

Table 2.1. 21-step MD equilibration scheme. Table reproduced from Ref. [106]. T_{max} = 600K, T_{final} = 300K, $P_{max} = 5 \times 10^4$ bar and P_{final} = 1 bar.

Step	Ensemble	Conditions	Length (ps)
1	NVT	T_{max}	50
2	NVT	T_{final}	50
3	NPT	T_{final}, $0.02 \times P_{max}$	50
4	NVT	T_{max}	50
5	NVT	T_{final}	100
6	NPT	T_{final}, $0.6 \times P_{max}$	50
7	NVT	T_{max}	50
8	NVT	T_{final}	100
9	NPT	T_{final}, P_{max}	50
10	NVT	T_{max}	50
11	NVT	T_{final}	100
12	NPT	T_{final}, $0.5 \times P_{max}$	5
13	NVT	T_{max}	5
14	NVT	T_{final}	10
15	NPT	T_{final}, $0.1 \times P_{max}$	5
16	NVT	T_{max}	5
17	NVT	T_{final}	10
18	NPT	T_{final}, $0.01 \times P_{max}$	5
19	NVT	T_{max}	5
20	NVT	T_{final}	10
21	NPT	T_{final}, P_{final}	800

However, a clear picture of PAN crystal molecular structure is still vague and molecular modelling of densely packed ensemble of PAN chains are desired to investigate the chain conformation under the influence of both intra- and inter-molecular interactions [110]. In the next chapter I will introduce our work on using MD to characterize how the tacticity and chain conformations affect the molecular structure of crystalline or pseudo-crystalline PAN structure

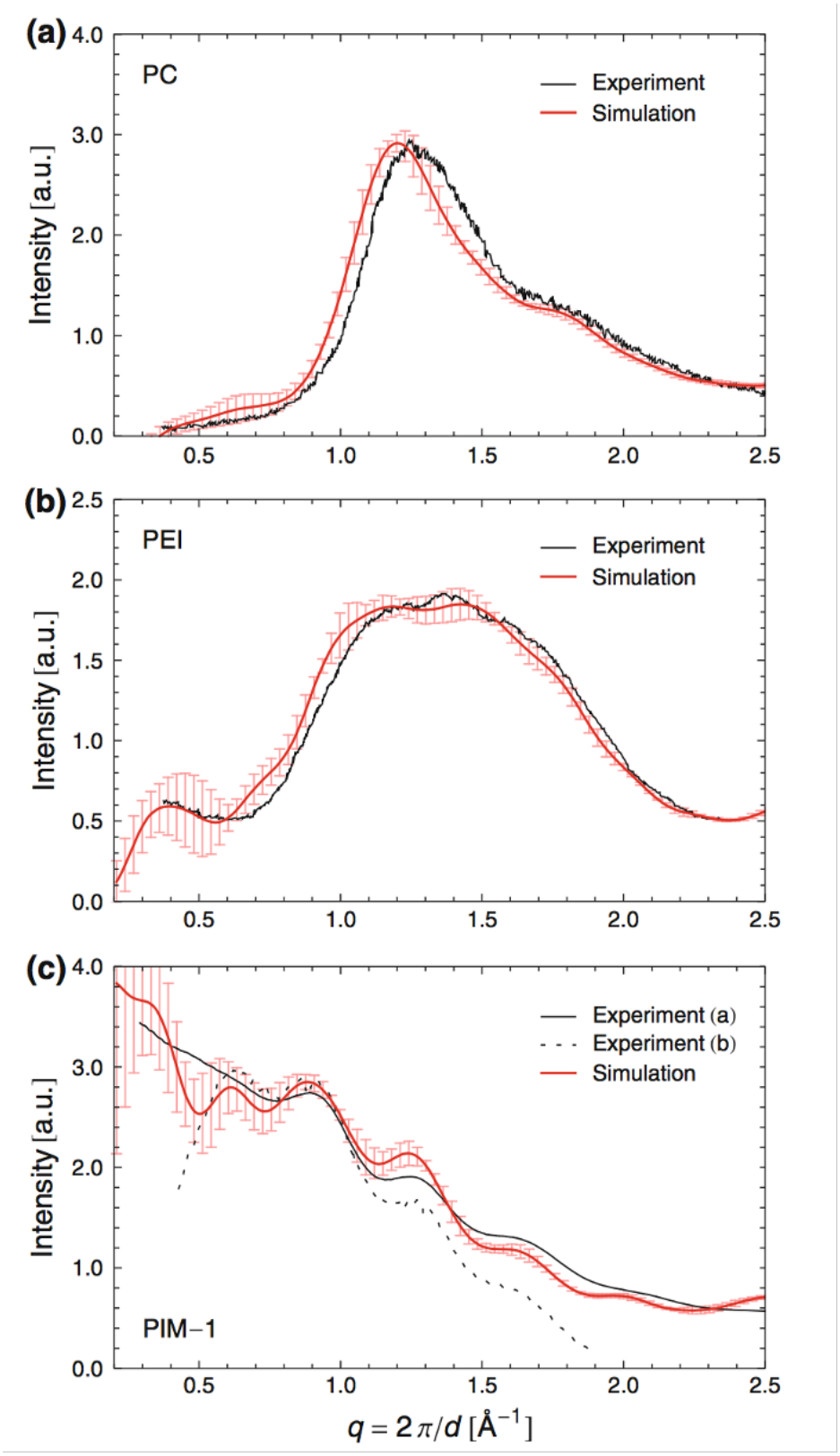

Figure 2.4. Simulated structure factors for (a) polycarbonate, (b) polyetherimide, and (c) PIM-1 shown in comparison with wide-angle X-ray scattering data. Figure adapted from Ref. [106].

and, by comparing predicted and experimental XRD patterns, establish molecular models for the various spun PAN fibers obtained under different conditions.

3. CRYSTALLINE AND PSEUDO-CRYSTALLINE PHASES OF POLYACRYLONITRILE FROM MOLECULAR DYNAMICS

3.1 Introduction

The structure of the PAN precursor, known to seriously affect the microstructure of the final CF and thus its performance, depends both on composition and spinning processing. Several requirements for a good PAN fiber precursor composition has been characterized. For example, the introduction of copolymers into the polymerization helps reduce the thermal degradation and accelerate the reactions involved in stabilization. [113] 0.5 mol % itaconic acid and 1.5 mol % 2-ethylhexyl acrylate are incorporated into PAN precursors, each of these component can decrease the initial cyclization temperature and shows significant improvement on PAN fibers orientation and physical performance, respectively [114]. Also, the addition of carbon nanotubes as a reinforcement of PAN fiber composite has recently attracted significant interest. R. Andrews demonstrated that 1.8 vol % graphitized multiwall carbon nanotubes give around 40% improvement in strength, modulus and yield properties of the final carbon fiber [115]. Other important factors of the PAN precursor include the molecular weight and its distribution [116] and polymerization process [117].

The early development of our understanding PAN molecular structure started with X-ray diffraction (XRD) studies [118–120] which provided key insight into the molecular structure of PAN fiber as well as the detailed chain conformation [108,121]. Figure 3.1 demonstrates the scattering pattern of pure PAN fiber precursors [122]. Based on diffraction information and the polar nature of the CN groups in PAN, crystalline regions have been proposed by Henrici-Olivé, S Olivé to consist of helical conformation with a diameter of 0.6 nm which is the most accepted chain model (Figure 3.2a) [123]. Then the pseudo-hexagonal (orthorhombic) cell has been introduced by Z. Bashir [120] (Figure 3.2b). Investigations of spun PAN CF precursors, especially in drawn state, indicate a two-phase structure consisting of crystalline and amorphous regions [118,119]. The crystalline regions, which represent more than 55% of the material by volume [10], arrange in lamellar structures. These chains are believed to be folded and aligned in lamellar structure which is vertical to the fiber axis. Separating the crystalline regions are amorphous regions which contains a large fraction of the copolymers, defects, entanglement, ends, loops and other disorder structures and exists between lamellas (Figure 3.2c) [118]. The alignment

of these lamellar determines the micro texture of the fiber cross section area which varies from radical to onion like. Most PAN-based CF has center texture whether isotropic or oriented differently from the outer skin (Figure 3.2d). [124,125] For molecular modeling in simulation, the only effort on PAN structures so far begins with stabilized fiber with a ladder molecule and is likely only contains 30% of structure formed during stabilization. [126,127] Regarding the role of tacticity on the molecular structure of the crystalline phase in PAN fibers, several nuclear magnetic resonance (NMR) studies [110,128] show that PAN chains are atactic but contains a significant stereoblock configuration of isotactic or syndiotactic diads with concentration depending on the polymerization method. Minagawa et al. [128] showed that up to 87% isotactic concentration could be reached under canal polymerization while anionic and radical polymerization results in higher atactic concentrations. However, the role of tacticity on molecular structure of the spun fibers is still not well understood.

Several molecular modelling studies have been carried out to predict the PAN structures including chain conformation [108,109], crystal morphology [110–112] and its stability [109,112]. Conformational energy calculations using PCILO (perturbed configuration interaction with localized orbitals) indicated that due to inter-molecular interactions, single-chain conformations with low energy are not favorable in crystalline regions [108,109]. Simulated XRD studies of PAN imply that the diffuse scattering in equatorial direction are due to the rotational disordered about the chain axes [110]. Therefore, an hexagonal or pseudo-hexagonal packing of rigid-rod polymer structures is generally accepted [110–112]. However, a clear picture of PAN crystal molecular structure is still vague and molecular modelling of densely packed ensemble of PAN chains are desired to investigate the chain conformation under the influence of both intra- and inter-molecular interactions [110].

In this chapter, I will introduce our work on characterizing how tacticity and the arrangement of torsional angles along the backbone affect packing of the chains and lattice parameters and, by comparing predicted and experimental XRD patterns, establish molecular models for the various spun PAN fibers obtained under different conditions.

3.2 Methods and simulation details

Our approach to predict the molecular structure of PAN crystalline regions consists of two main steps: i) Generating PAN chains with various helicities as initial structures. In order to avoid

end effects, these chains are periodic along their axes; ii) Packing individual, parallel chains into a 3D periodic cell with a hexagonal arrangement and fully relaxing the simulation cell.

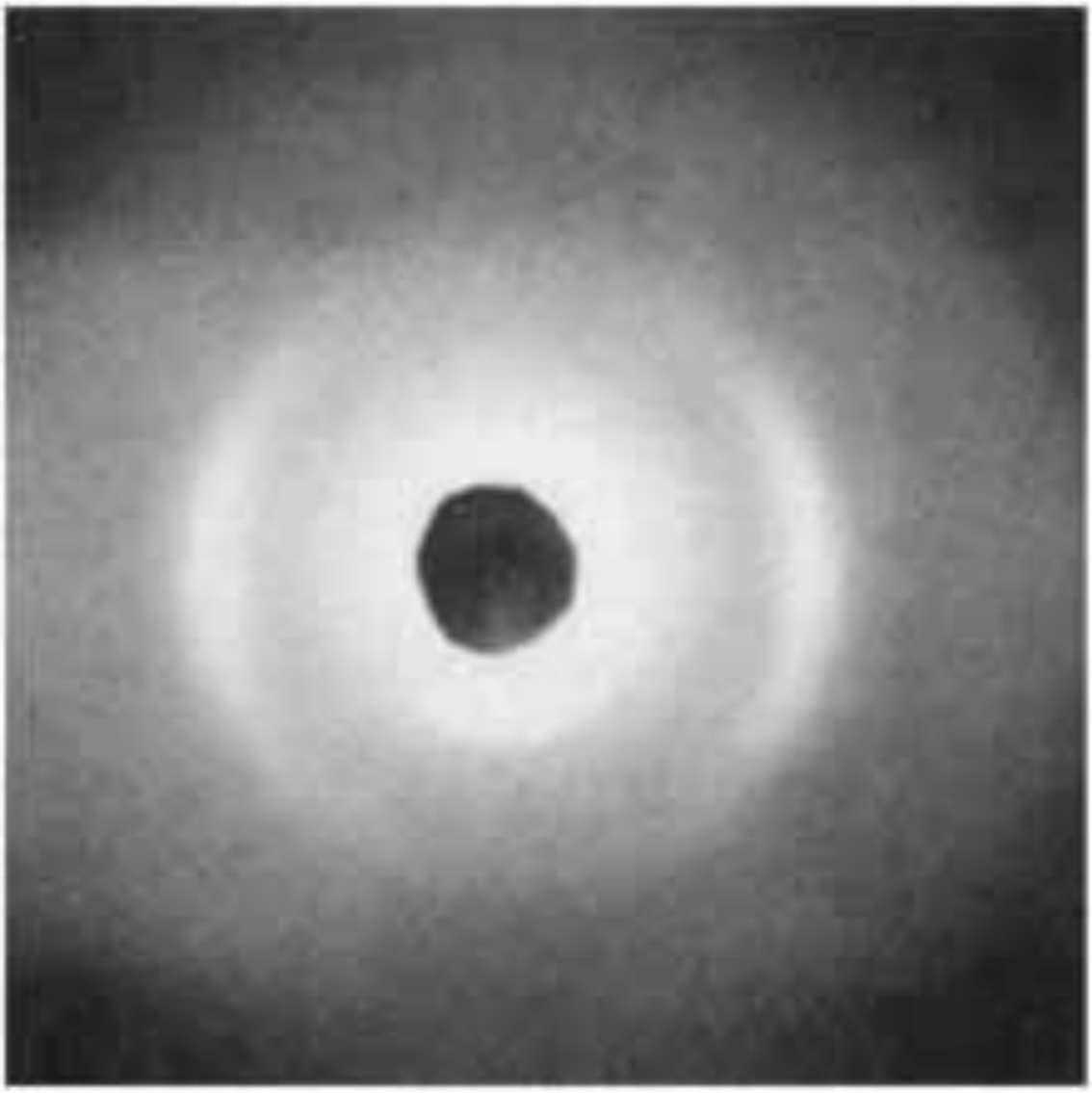

Figure 3.1. X-ray diffraction photographs of pure PAN precursors. Figure taken form Ref. [122].

3.2.1 Generating PAN chains with various helicities

The chain conformation of polymers, including helicity, is governed by the arrangement of torsional angles along the backbone [129]. In our case, backbone atoms are carbon with sp^3 hybridization, thus they favor *trans* (*t)* and *gauche* (*g±*) conformations where dihedral angles are

180° and ±60° respectively. PAN polymer helices can then be generated by different patterns of *t* and *g* conformations.

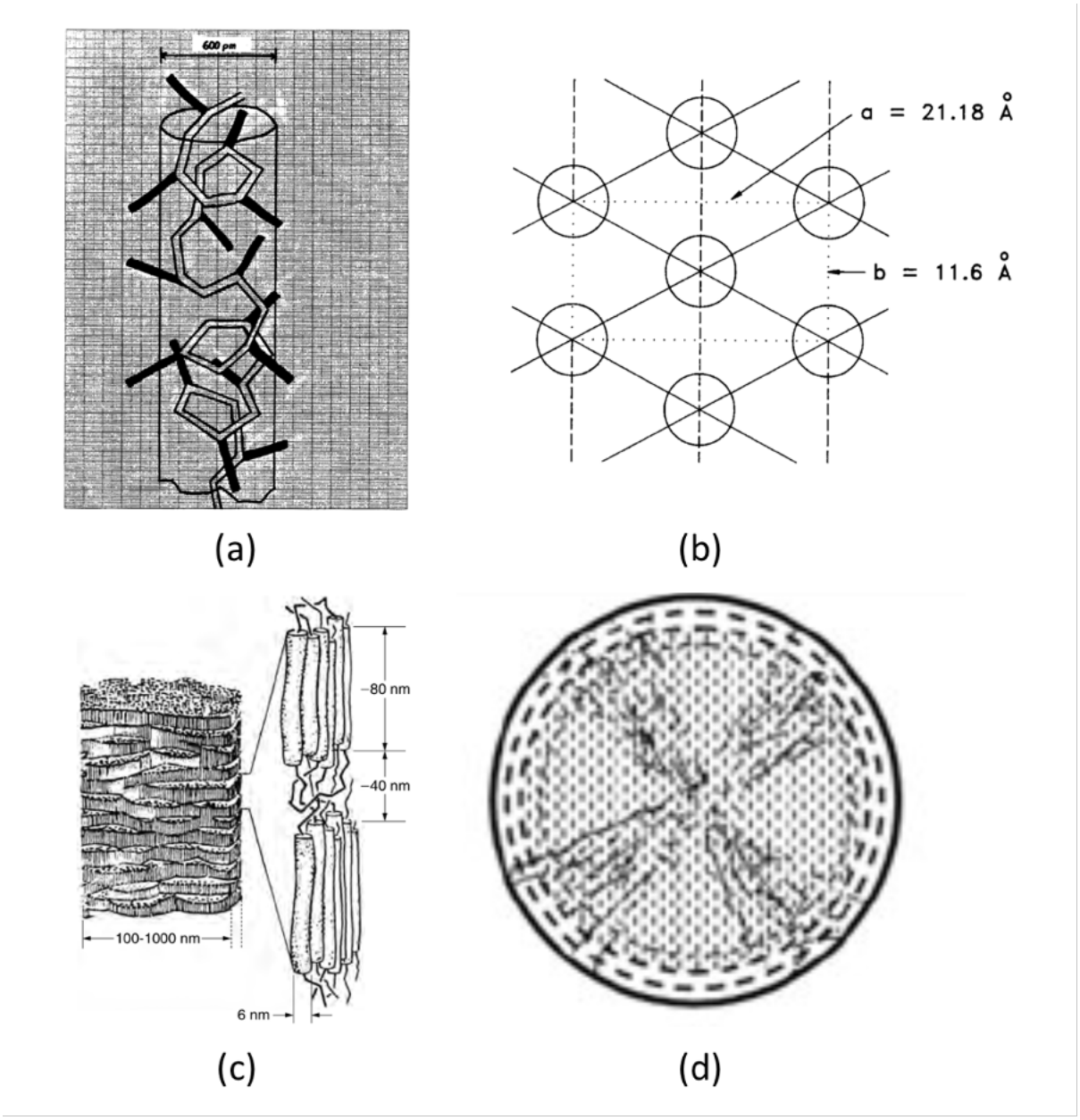

Figure 3.2. (a) Helical chain conformation model of PAN molecule, figure adapted from Ref. [123]. (b) Orthorhombic cell of PAN crystal, figure adapted form Ref. [120]. (c) Molecular Structure model of PAN fiber, figure adapted from Ref. [118]. (d) schematic representation of cross-sectional micro textures, figure adapted from Ref. [125].

We used PolymerModeler [130,131] tool in nanoHUB.org [132] to generate the initial PAN chain structures of various helicities, tacticities and chrialities. PolymerModeler builds polymer chains adding one monomer at a time, with the desired torsional angle, removing the head atom of the new monomer and the tail of the previous one and creating a chemical bond between the backbone atoms. The connection configuration can be specified by bond length, bond angle and dihedral angle [130]. In this study, we use two propionitrile molecule sets as the monomers, see Figure 3.3, by choosing different head and tail atoms we achieve different conformations and tacticities. Only molecule set (a) is used when building isotactic structures; molecule sets (a) and (b) are alternated for syndiotactic structures and randomly chosen with 0.5 probability each set for atactic structures. By choosing different head atoms, we can control the *t* or *g* conformation for skeletal connection where the central bond is located inside the monomer. For skeletal connections where the central bond is located between the monomer, we fix the torsion angles and apply only to torsions between monomers. In this work, for simplicity we choose two *t*-*g*(±) conformations as a repeat unit to generate different chain conformations. Detailed input torsion angles are shown in Table 3.1 where in chain conformation '***T***' indicates *t* conformation, '***G***' indicates *g*+ conformation and '***G'***' indicates *g*- conformation and in chirality '+' indicates the structure is right-handed and '**-**' indicates left-handed.

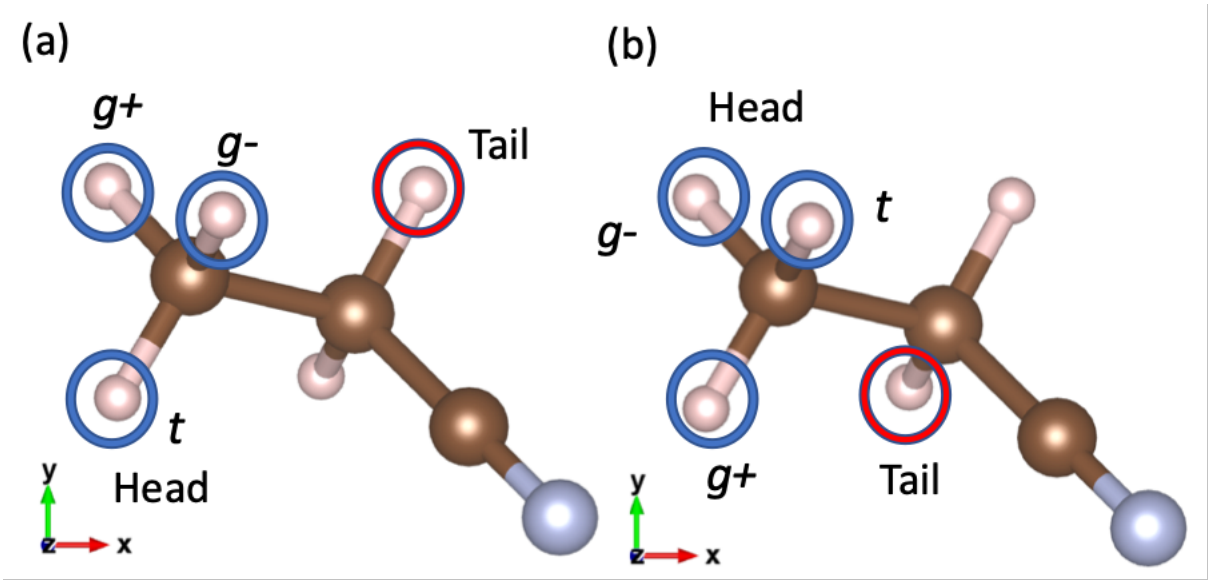

Figure 3.3. Two sets of head and tail atoms for propionitrile molecule. Only set (a) is used when building isotactic structures; set (a), set (b) alternatively for syndiotactic structures and randomly with 0.5 probability each set for atactic structures. Figure adapted from Ref. [133].

Table 3.1. Input torsion angle and nomenclature of resulting structures with the simulation lattice and box size information. Table adapted from Ref. [133].

Tacticity	Torsion angle inside monomers	Torsion angle between monomers	*trans* ratio (%)	Backbone repeat unit along *c* axis (# of C atoms)	Nomenclature	Chriality	Simulation lattice				Simulation box size					
							a (Å)	*b* (Å)	*c*		*a*		*b*		*c*	
									# of monomers	Length (Å)	# of units	Length (Å)	# of units	Length (Å)	# of units	Length (Å)
atactic	60°	60°	0	4	G_4	+	11.98	6.92	18	31.90	3	35.94	5	34.58	1	31.90
	60°	-60°			NP (not possible)											
	-60°	60°														
	-60°	-60°			G'_4	-	11.98	6.92	18	31.90	3	35.94	5	34.58	1	31.90
	60°	180°	50	6	$(GT)_3$	+	11.15	6.44	15	30.69	3	33.45	5	32.19	1	30.69
	180°	60°														
	-60°	180°			$(G'T)_3$	-										
	180°	-60°														
	180°	180°	100	2	T_2	*	10.07	5.82	12	30.08	3	30.22	6	34.90	1	30.08
isotactic	60°	60°	0	4	G_4	+	11.98	6.92	2	3.54	3	35.94	5	34.58	9	31.90
	60°	-60°			NP											
	-60°	60°														
	-60°	-60°			G'_4	-	11.98	6.92	2	3.54	3	35.94	5	34.58	9	31.90
	60°	180°	50	6	$(GT)_3$	+	11.15	6.44	3	6.14	3	33.45	5	32.19	5	30.69
	180°	60°			$(TG)_3$											
	-60°	180°			$(G'T)_3$	-										
	180°	-60°			$(TG')_3$											
	180°	180°	100	2	T_2	*	10.07	5.82	1	2.51	3	30.22	6	34.90	12	30.08
syndiotactic	60°	60°	0	4	G_4	+	11.98	6.92	2	3.54	3	35.94	5	34.58	9	31.90
	60°	-60°			NP											
	-60°	60°														
	-60°	-60°			G'_4	-	11.98	6.92	2	3.54	3	35.94	5	34.58	9	31.91
	60°	180°	50	6	$(GT)_3$	+	11.15	6.44	3	6.14	3	33.45	5	32.19	5	30.69
	180°	60°														
	-60°	180°			$(G'T)_3$	-										
	180°	-60°														
	180°	180°	100	2	T_2	*	10.07	5.82	1	2.51	3	30.22	6	34.90	12	30.08

After removing the *g*+, *g*- combinations which do not to generate extended structures because of overlapping atom positions after two monomers [labeled NP (not possible) in Table 3.1] and accounting for identical configurations generated by different combination of *t-g* conformations, like atactic $\boldsymbol{(TG)_3}$, $\boldsymbol{(TG')_3}$ and syndiotactic $\boldsymbol{(TG)_3}$, $\boldsymbol{(TG')_3}$, we obtain a total of 17 different chain conformations, 5 for atactic, 7 for isotactic and 5 for syndiotactic. Atomic snapshots of chain conformation structures are shown in Figure 3.4. Structures with all *g*+ conformation have two monomers as a repeat unit with total of four C atoms, therefore we denote them $\boldsymbol{G_4}$ and $\boldsymbol{G'_4}$ for its chiral all *g*- conformations. Structures consisting of alternating *t* and *g* conformations result in chains with a repeat unit of three monomers (six C atoms). However, for isotactic chains, different arrangements of torsions will result in different chain conformations, see Figure 3.4(b). In order to distinguish these conformations, we use $\boldsymbol{(G'T)_3}$ and $\boldsymbol{(TG')_3}$ with its corresponding structures shown in Table 3.1 and Figure 3.4(b) where $\boldsymbol{(GT)_3}$ and $\boldsymbol{(TG')_3}$ are mirror image of each other and $\boldsymbol{(TG)_3}$ and $\boldsymbol{(G'T)_3}$ are mirror image of each other. Atactic and syndiotactic systems with alternating torsion angles of 60° (or -60°), 180° result in the same conformation regardless of the torsion angle location (Table 3.1 and Figure 3.4(a) & (c)). Structures with all *t* conformations do not have chirality and result in a repeat unit of one monomer (two C atoms), this is also known as planar zig-zag configuration.

3.2.2 Packing and relaxation

To study condensed phases of PAN crystals we pack the various types chains into a hexagonal lattice with $\mathbf{a} = \sqrt{3}\mathbf{b}$, see Figure 3.5. This represents closed packed structures as proposed by Z. Bashir based on XRD study [120]. The initial density of the simulation cells is set to 1.2 g/cm^3 based on the range of densities reported experimentally 1.17-1.22 g/cm^3 [134]. Detailed simulation lattice information are illustrated in Table 3.1. For isotactic and syndiotactic structures, we built 10 samples for each chain conformation with random rotations of the chains about their axes to average (examples shown in the first row of Figure 3.5), while for atactic structures with same backbone helix, the analysis is averaged over 10 samples with chains having different iso-syn sequence (see Table 3.2). Then we did canonical MD at 300 K for 50 ps followed by isothermal-isobaric MD at 300 K and 1 atm for 1 ns to relax the structures and simulation cells using Nosé-Hoover barostat and thermostat [135] as implemented in LAMMPS [136] with

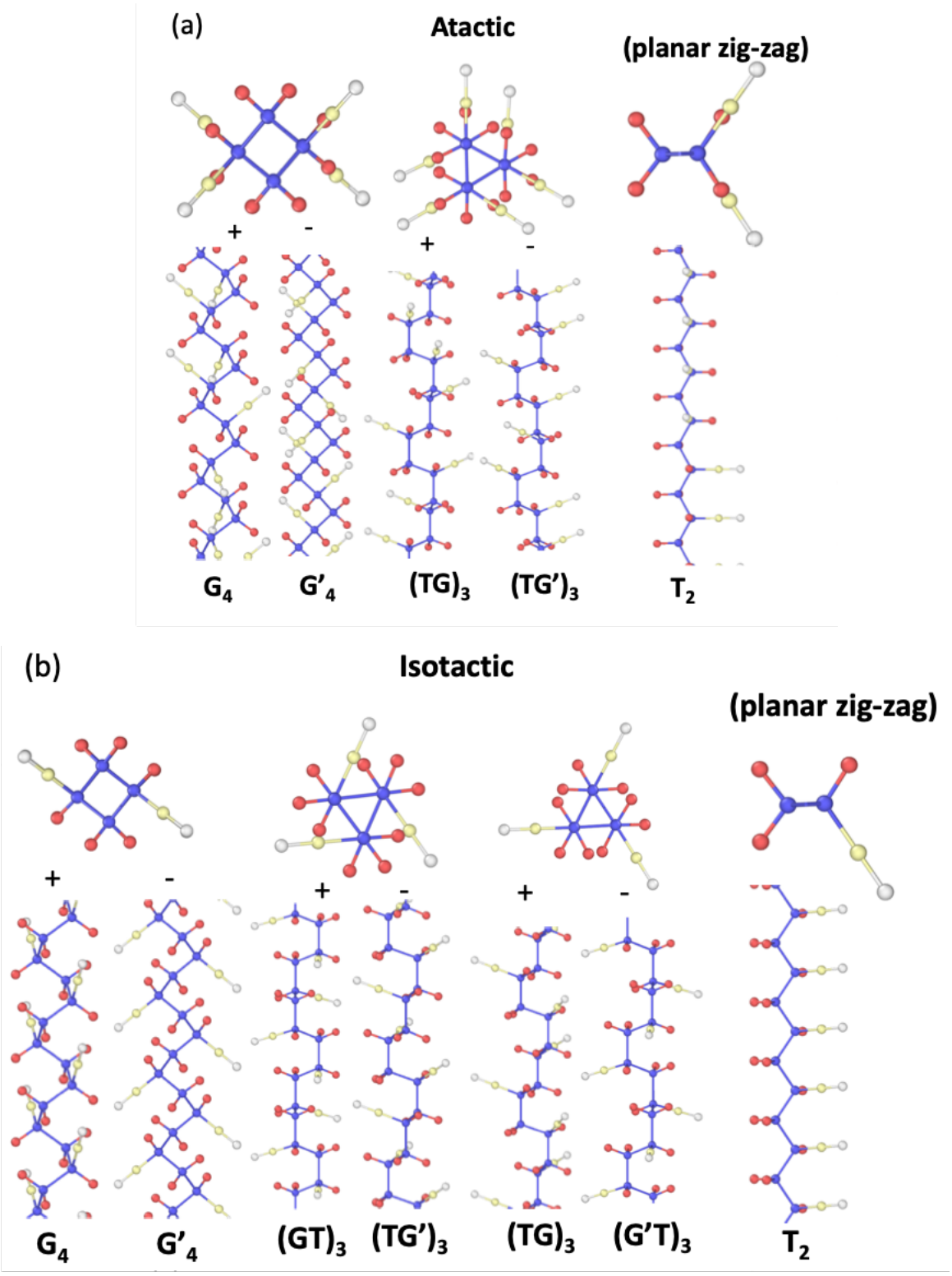

Figure 3.4. Various helix structures of (a) atactic, (b) isotactic and (c) syndiotactic chains. Above: view along the chain; bottom: side view of the chain. Figure adapted from Ref. [133].

Figure 3.4. continued

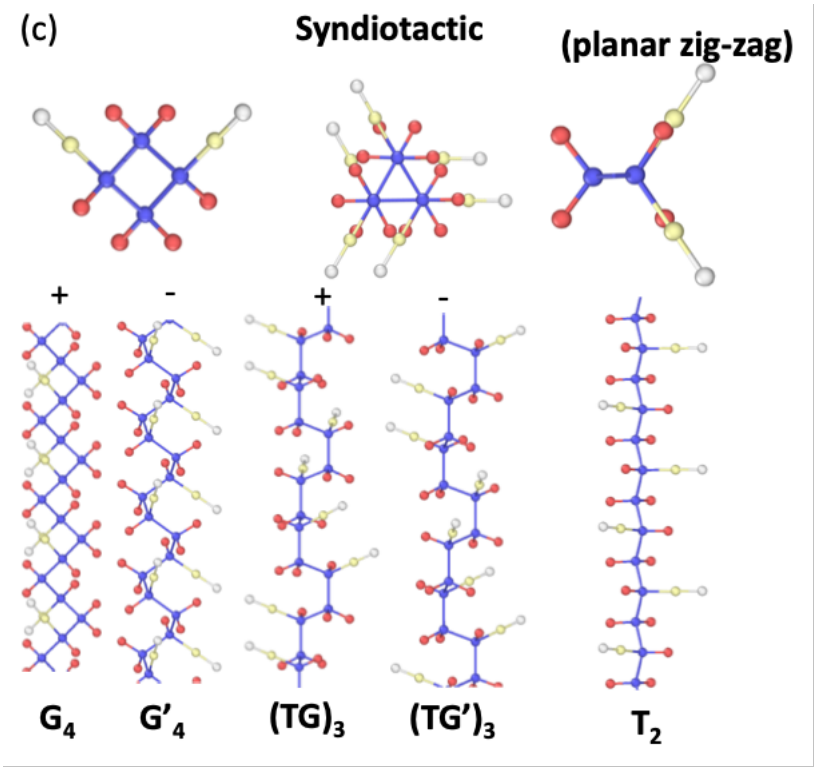

relaxation time of 4 ps for thermostat setting during canonical MD and 1 ps and 0.1 ps for barostat and thermostat settings respectively during isothermal-isobaric MD.

After 50 ps canonical MD of structural relaxation, the initial orientation effects among 10 samples each backbone helix structure category for isotactic and syndiotactic structures and initial iso-syn sequence effects for atactic structures are no longer observed as shown in Figure 3.6(a), (b). All structures are sufficiently relaxed within 50 ~ 300 ps isothermal-isobaric MD, see Figure 3.6(c), (d), while we continued our relaxation time to 1 ns and got structural information and did analysis using frames from the final 500 ps steps.

3.2.3 Interatomic potential and atomic charges

We describe atomic interactions using the DREIDING [89] force field with charges obtained using charge equilibration (QEq) [137–139]. The QEq parameters we use in this study, shown in Table 3.3, are taken from [140] are based on Bultinck et al. [139] The energy expression used for QEq includes electronegativity χ_i^*, the hardness of atom η_i^* and the shielded Coulomb

constant J_i^0 in reciprocal of distant unit Å [141]. For electrostatics calculation we use Particle-Particle-Particle-Mesh (PPPM) algorithms [142,143].

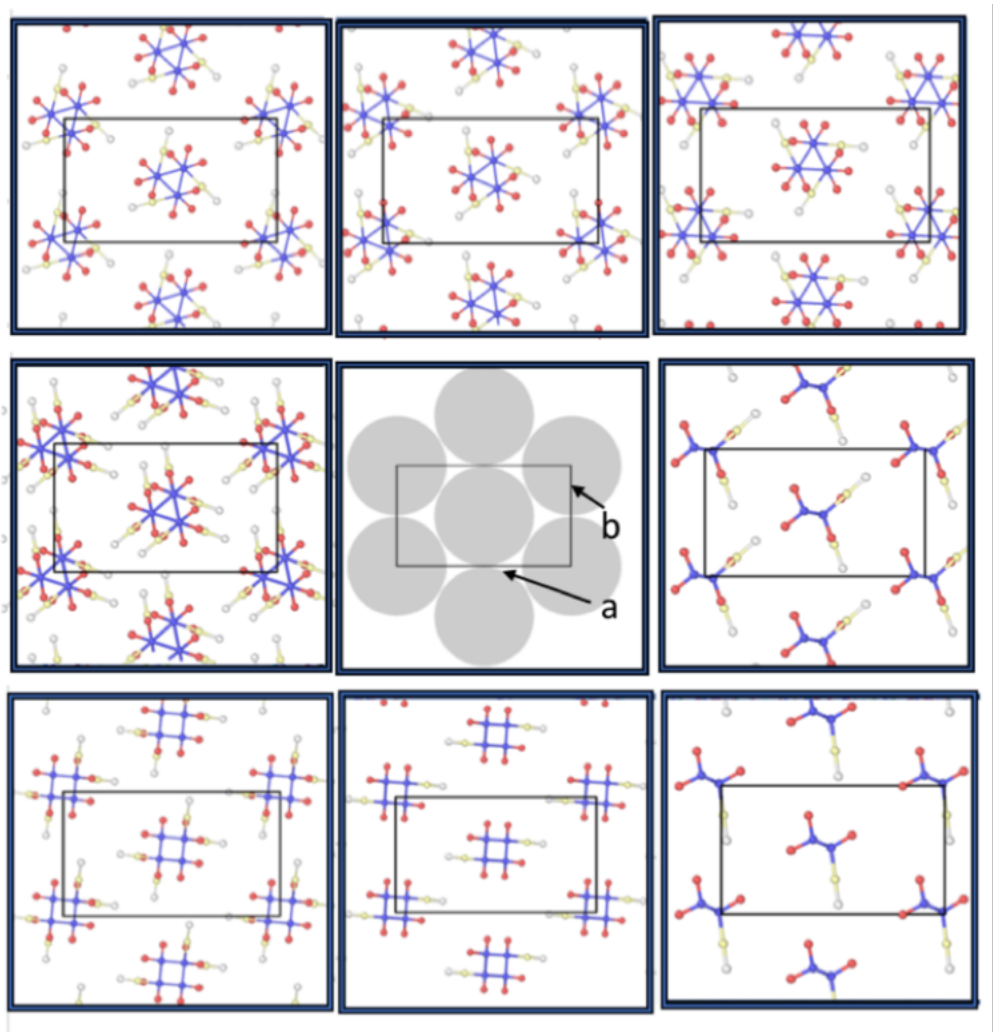

Figure 3.5. Hexagonal cell of PAN crystal (center) and top views of several samples packing in hexagonal cell as initial structures. The first row shows the 3 samples of different rotations about their axes for isotactic ***(GT)₃*** chain configuration. Other samples are syndiotactic ***(GT)₃*** (center left), atactic ***T₂*** (planar zig-zag) (center right), atactic ***G₄*** (bottom left), isotactic ***G₄*** (bottom middle) and isotactic ***T₂*** (planar zig-zag) (bottom right). Figure adapted from Ref. [133].

3.2.4 Structure data analysis

SFF is key to validate our predicted structures against experiments. Based on Eq. (2.17), for a multicomponent system like PAN, we obtain the partial pair distribution function $g_{\alpha\beta}(r)$ from MD trajectory and do a FT of $g_{\alpha\beta}(|\mathbf{r}|) - 1$:

Table 3.2. Simulated random sequence information for atactic structures.

Backbone structure	Monomer length	Sample index	Random sequence	iso-ratio	syn-ratio
G_4	18	0	i-i-i-i-s-s-s-i-i-s-i-i-s-i-s-s-i-s	0.556	0.444
		1	s-i-i-i-i-s-i-i-i-i-i-i-i-i-s-s-i	0.778	0.222
		2	s-i-i-s-i-s-s-s-i-s-s-s-i-i-i-i-i-i	0.556	0.444
		3	s-i-s-i-s-s-s-i-s-i-i-s-i-i-i-i-s-i	0.556	0.444
		4	i-s-i-s-i-i-s-s-s-s-s-s-s-i-i-s-s	0.333	0.667
		5	s-s-i-i-i-s-i-s-i-i-i-i-i-s-s-i-s-s	0.556	0.444
		6	s-s-i-i-s-s-s-i-i-i-s-s-s-s-i-i-i-s	0.444	0.556
		7	s-i-s-i-i-i-i-i-s-i-s-s-s-s-s-i-s-s	0.444	0.556
		8	s-i-s-i-i-s-i-s-s-s-i-s-s-s-s-i-s-s	0.333	0.667
		9	i-i-s-i-i-i-s-i-i-i-i-i-i-i-s-s-i-i	0.778	0.222
G'_4		0	s-i-i-i-s-s-s-s-s-s-s-i-s-i-i-s-s-s	0.333	0.667
		1	s-s-s-i-s-s-s-s-s-s-i-i-s-s-i-i-s-i	0.333	0.667
		2	i-i-s-i-i-s-i-s-s-s-i-s-i-s-i-i-s-i	0.556	0.444
		3	i-i-s-i-s-i-s-s-i-s-i-i-s-i-i-i-s-s	0.556	0.444
		4	s-i-s-i-i-s-s-s-s-i-i-s-i-s-i-i-i-i	0.556	0.444
		5	i-i-i-i-s-s-i-i-s-i-i-i-i-i-s-i-i-i	0.778	0.222
		6	i-s-i-s-s-s-i-i-i-i-i-i-s-s-i-s-i-s	0.556	0.444
		7	s-s-s-s-s-i-i-i-i-i-s-s-s-i-i-i-s-s	0.444	0.556
		8	i-s-s-s-s-s-s-i-i-i-s-i-s-s-i-s-s-s	0.333	0.667
		9	i-s-i-s-s-s-i-s-s-s-i-s-i-s-s-i-i-i	0.444	0.556
$(TG)_3$	15	0	s-i-i-s-s-s-i-s-s-i-i-s-i-s-i	0.467	0.533
		1	i-i-i-s-i-i-i-i-i-i-i-i-i-s-i	0.867	0.133
		2	i-i-s-s-i-i-i-i-s-s-s-s-i-s-s	0.467	0.533
		3	s-s-i-i-i-s-s-s-i-i-s-i-s-s-i	0.467	0.533
		4	i-s-s-s-i-i-s-i-s-s-s-i-i-i-s	0.467	0.533
		5	s-s-s-i-s-s-i-s-s-s-i-s-i-s-i	0.333	0.667
		6	i-i-i-i-s-i-i-i-i-i-i-s-i-i-i	0.867	0.133
		7	s-i-s-s-s-s-s-s-i-i-i-s-i-i-i	0.467	0.533
		8	s-i-i-i-i-s-s-i-i-s-s-s-s-i-s	0.467	0.533

Table 3.2. continued

(TG)₃	15	9	i-s-i-i-i-i-s-s-i-i-s-s-s-i-i	0.6	0.4
(TG')₃	15	0	i-s-s-i-s-i-s-s-s-s-i-s-i-i-i	0.467	0.533
		1	s-s-s-s-i-i-i-i-s-i-s-s-i-s-i	0.467	0.533
		2	i-i-s-s-s-s-s-s-i-s-i-s-s-i-s	0.333	0.667
		3	i-s-i-i-i-s-s-i-i-s-s-i-i-s-i	0.6	0.4
		4	i-s-s-i-s-s-s-s-i-s-i-i-s-i-i	0.467	0.533
		5	i-s-i-i-i-s-s-i-i-s-s-i-s-i-i	0.6	0.4
		6	i-s-i-i-i-s-i-s-i-s-s-i-i-i-s	0.6	0.4
		7	s-i-s-i-s-s-i-s-i-i-s-i-i-i-i	0.6	0.4
		8	s-s-i-s-s-s-i-s-s-s-i-s-i-i-s	0.333	0.667
		9	i-i-s-i-s-i-i-i-s-s-s-i-s-s-s	0.467	0.533
T₂	12	0	s-s-i-i-i-s-i-i-i-i-s-i	0.667	0.333
		1	i-s-i-i-i-s-s-s-i-s-i-s	0.5	0.5
		2	s-s-s-s-s-s-s-i-i-i-i-s	0.333	0.667
		3	s-i-i-s-s-s-s-s-s-s-s-s	0.167	0.833
		4	s-i-i-s-s-s-i-i-s-s-s-s	0.333	0.667
		5	i-s-s-s-i-i-s-s-i-i-i-s	0.5	0.5
		6	s-s-s-i-i-s-i-i-i-s-s-i	0.5	0.5
		7	i-i-i-s-s-i-s-i-s-s-s-i	0.5	0.5
		8	s-s-i-i-i-i-s-i-i-s-i-i	0.667	0.333
		9	i-i-s-i-i-i-s-s-i-i-s-i	0.667	0.333

$$S_{\alpha\beta}(\mathbf{q}) - 1 = \int \exp(i\mathbf{q}\cdot\mathbf{r})\, \rho \left[g_{\alpha\beta}(|\mathbf{r}|) - 1 \right] d\mathbf{r} \tag{3.19}$$

where **q** is the wavevector in reciprocal space, ρ is the average number density which can be obtained by total number of particles divided by volume and **r** is the position in respect to the reference [144].

Because $g_{\alpha\beta}(r)$ is spherically averaged, the three-dimensional variable can be converted into a one-dimensional variable which is only related to the radius r. Thus, Eq. (3.19) is converted

to a radius integral Fourier transform. The relationship between the structure factor and distribution function can be expressed as

$$S_{\alpha\beta}(q) = 1 + 4\pi\rho \int_0^{\infty} \frac{\sin qr}{qr} [g_{\alpha\beta}(r) - 1] r^2 dr \qquad (3.20)$$

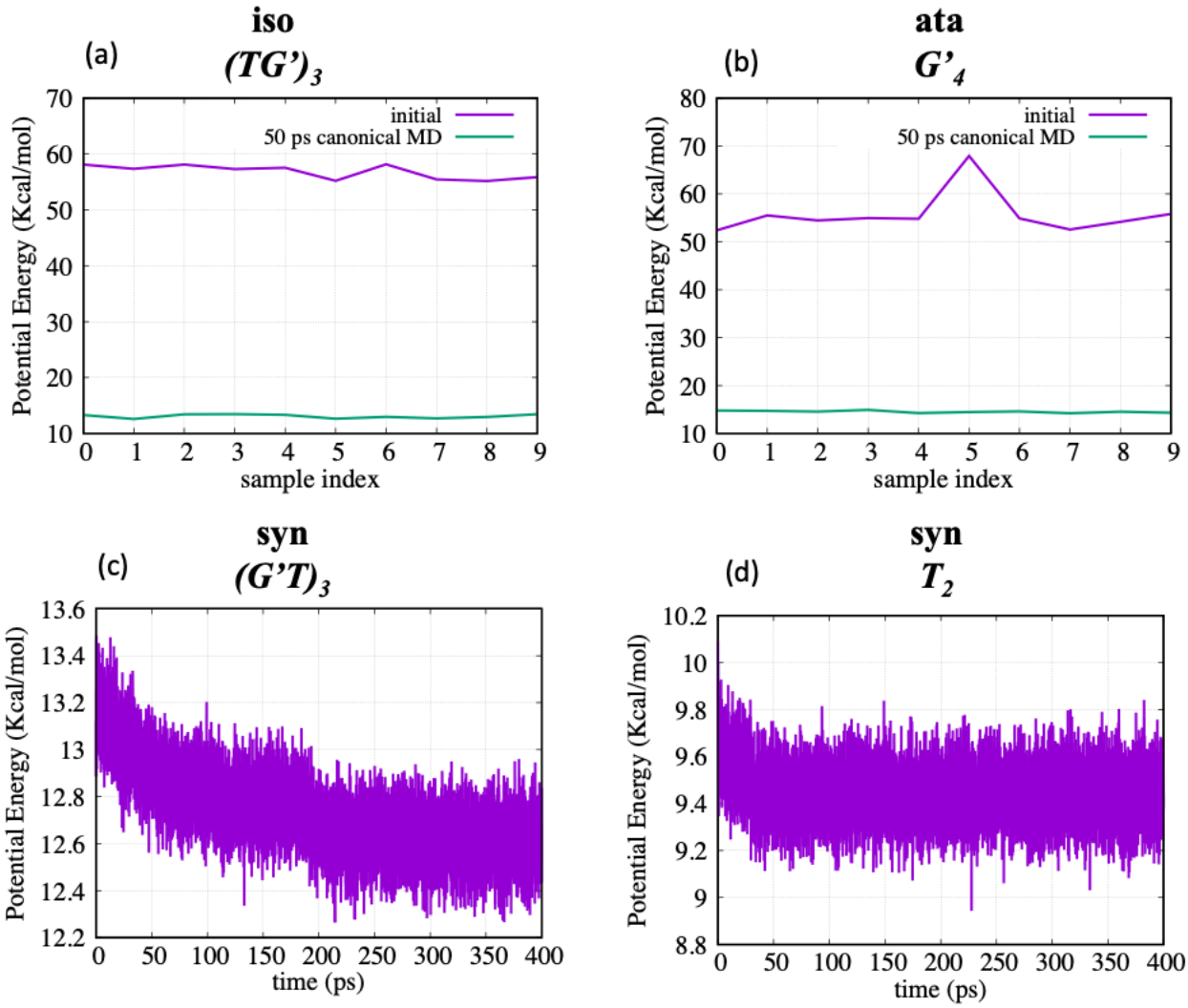

Figure 3.6. Potential energy comparison among (a) 10 isotactic ***(TG')₃*** samples and (b) 10 atactic ***G'₄*** samples before and after 50 ps canonical MD; potential energy evolution during first 400 ps for syndiotactic sample (c) ***(G'T)₃*** and (d) ***T₂***.

Calculations for pair SSFs for one of the isotactic systems are shown in Figure 3.7. Out of the calculated partial SSF we can obtain the total SSF by

$$S(q) = \frac{\sum_{\alpha,\beta} c_\alpha c_\beta f_\alpha(q) f_\beta(q) S_{\alpha\beta}(q)}{\sum_{\alpha,\beta} c_\alpha c_\beta f_\alpha(q) f_\beta(q)} \tag{3.21}$$

as shown in Figure 3.7 where c_α, c_β are the concentration of the species and $f_\alpha(q)$, $f_\beta(q)$ are the X-ray form factors [145].

Table 3.3. QEq parameters. Table reproduced from Ref. [133].

Atom type	χ_i^* (eV)	η_i^* (eV)	J_i^0 ($Å^{-1}$)
H	1.0	17.95	2.4931
C	5.25	9.0	1.2500
N	8.8	9.39	1.3041

After we obtain the SSF S(q) of a system, we can obtain the scattering function si(q) defined as

$$si(q) = q[S(q) - 1] \tag{3.22}$$

3.3 Molecular structures and validation

All the initial structures were successfully relaxed and resulted in stable configurations. While the relaxation under isobaric, isothermal conditions results in structural changes, including the loss of crystalline order in ***c*** axis in many cases, the character of the initial structure is retained to a certain degree. Figure 3.8 shows atomistic snapshots of selected structures. In all cases we find the hexagonal packing arrangement is preserved and the chains remain parallel to each other. Out of the 17 systems, 14 lost chain axis periodicity and resulted in pseudo-crystalline structures; examples are shown in Figure 3.8(a). The other three systems, isotactic ***(TG)$_3$*** and ***(G'T)$_3$***, and syndiotactic planar zig-zag (***T$_2$***) (Figure 3.8(b)) retain their chain axis periodicity.

The following sub-sections discuss the characterization of the resulting structures and detailed structure information like cell parameters, densities and resulting *trans* ratios and comparison of the simulated XRD patterns and scattering functions with the experimental data.

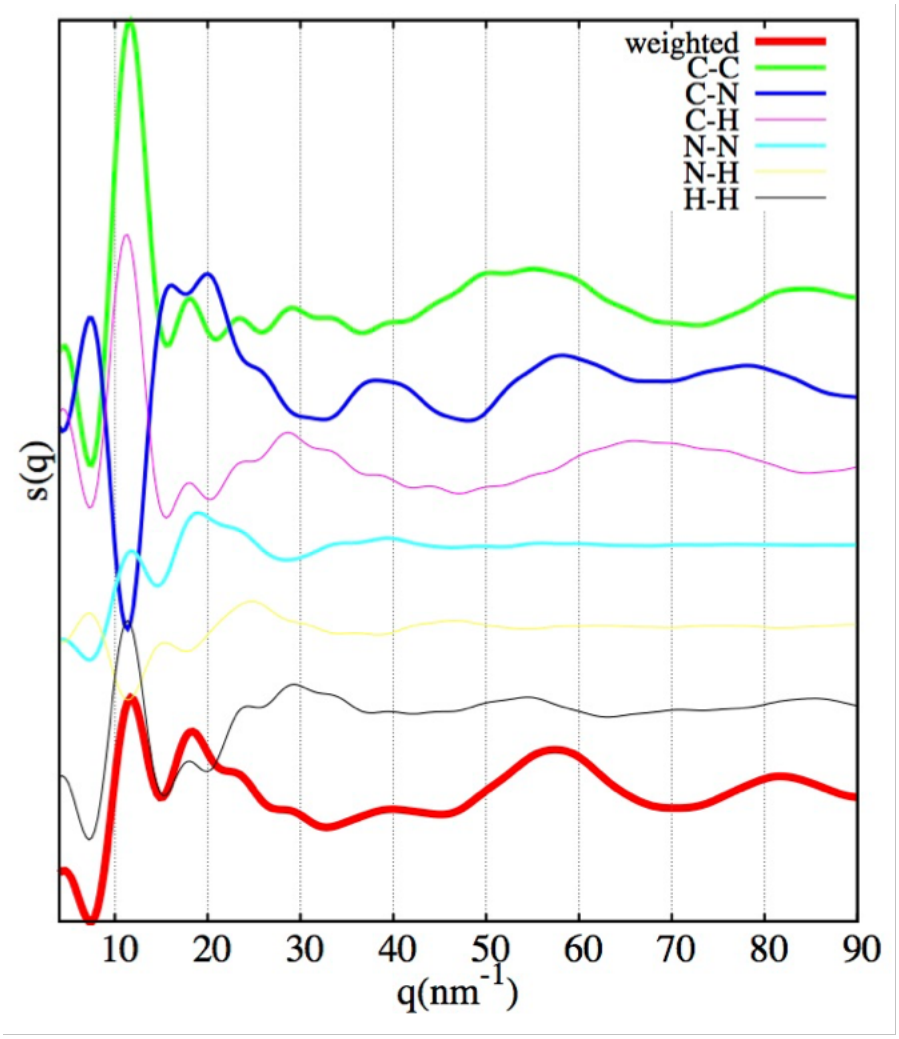

Figure 3.7. Pair static structure factors and weighted static structure factor. Figure adapted from Ref. [133].

3.3.1 Density and chain conformations

After relaxation, the densities of all structures are in range of 1.14 - 1.21 g/cm^3 (see Table 3.4 and Figure 3.9(a)) which is excellent agreement with the experimental range 1.17 - 1.22 g/cm^3 [134]. Except the syndiotactic planar zig-zag conformation (***T*$_2$**), the *trans* ratios of all other structures evolve during thermalization, see Figure 3.9(b). This is more pronounced for the structures starting with ***G*$_4$** or ***T*$_2$** conformations. Since the relaxed chain conformation for pseudo-crystalline structures is no longer the same as its initial structure, we adopt a new nomenclature by using its tacticity, chirality and final *trans*/*gauche* ratio with subscript ***p*** indicating pseudocrystallinity, and subscript ***c*** indicating ***c***-axis ordered structures (see Table 3.4).

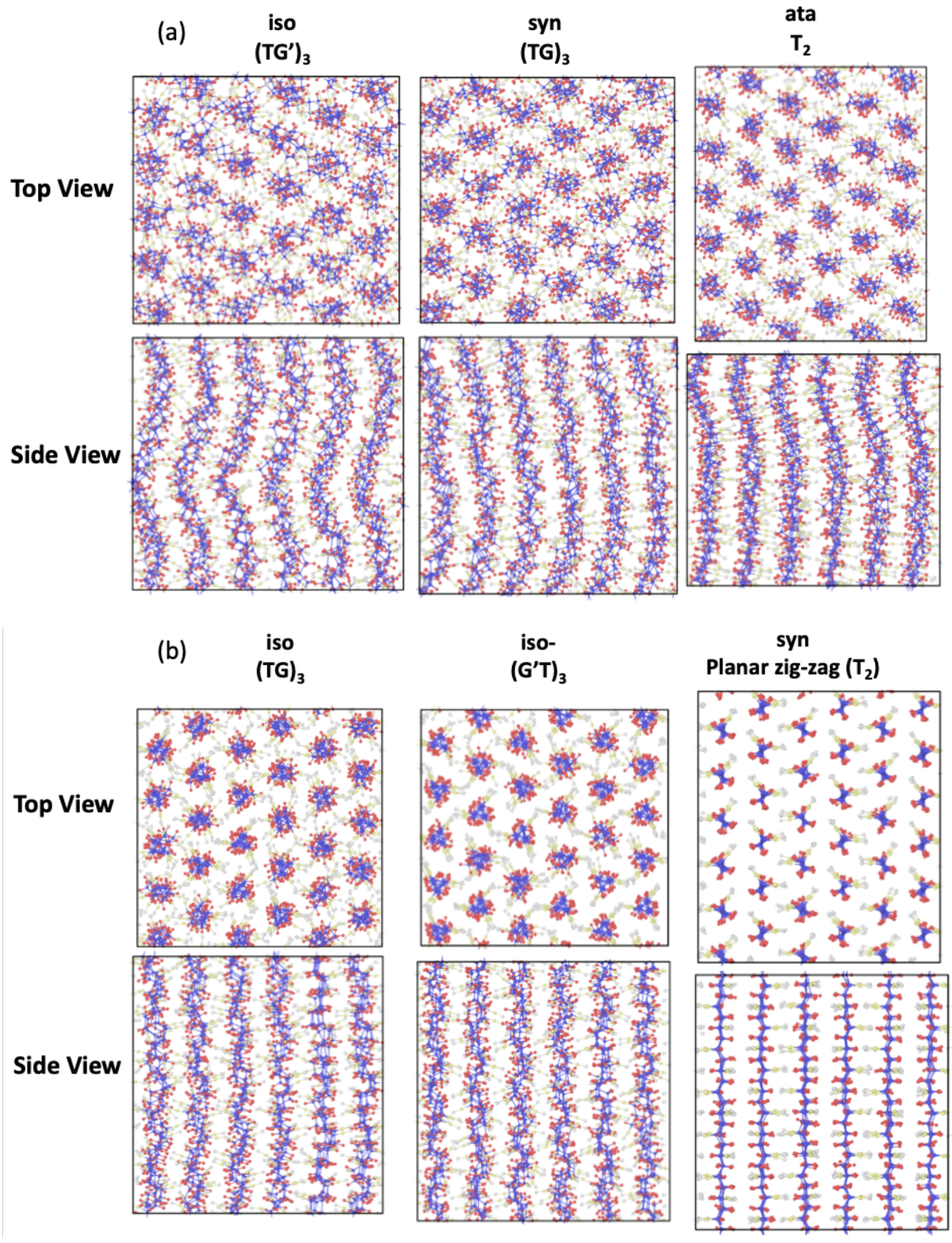

Figure 3.8. (a) Sample started with isotactic ***(TG')₃***, syndiotactic ***(GT)₃*** and atactic ***T₂*** as pseudo-crystalline structures and (b) isotactic ***(TG)₃***, isotactic ***(G'T)₃*** and syndiotactic planar zig-zag (***T₂***) as samples of ***c***-axis-ordered structures. Figure adapted from Ref. [133].

Table 3.4. New nomenclature, density, XRD and proposed lattice information. Table adapted from Ref. [133].

Tacticity	Initial Structure	*trans* Ratio		New nomenclature	*d*-Spacings (Å)	Lattice/Cell[a]	Lattice Constants (Å)			Densities (g/cm^3)
		Initial	Resulting				*a*	*b*	*c*	
atactic	G_4	0%	25%	$a+(T_{25}G_{75})_p$	5.57, 3.20	H/O	11.14	6.40	*	1.167±0.009
	G'_4		26%	$a-(T_{26}G_{74})_p$	5.62, 3.37	H/O	11.23	6.74	*	1.165±0.009
	$(TG)_3$	50%	54%	$a+(T_{54}G_{46})_p$	5.35, 3.10	H/O	10.70	6.20	*	1.17±0.02
	$(TG')_3$		53%	$a-(T_{53}G_{47})_p$	5.48, 3.07	H/O	10.96	6.14	*	1.164±0.005
	T_2	100%	86%	$a(T_{86}G_{14})_p$	5.27, 3.00	H/O	10.53	6.01	*	1.142±0.004
isotactic	G_4	0%	35%	$i+(T_{35}G_{65})_p$	5.62, 3.24	H/O	11.23	6.49	*	1.16±0.01
	G'_4		32%	$i-(T_{32}G_{68})_p$	5.66, 3.39	H/O	11.32	6.77	*	1.17±0.02
	$(GT)_3$	50%	48%	$i+(T_{48}G_{52})_p$	5.39, 3.09	H/O	10.78	6.17	*	1.150±0.003
	$(TG')_3$		47%	$i-(T_{47}G_{53})_p$	5.52, 3.16	H/O	11.05	6.31	*	1.150±0.003
	$(TG)_3$		52%	$i+(T_{52}G_{48})_c$	5.44, 4.22, 3.12	H/O	10.87	6.25	6.70	1.161±0.005
	$(G'T)_3$		52%	$i-(T_{52}G_{48})_c$	5.48, 4.25, 3.20	H/O	10.96	6.31	6.65	1.163±0.006
	T_2	100%	67%	$i(T_{67}G_{33})_p$	5.27, 3.07	H/O	10.53	6.14	*	1.161±0.004
syndiotactic	G_4	0%	35%	$s+(T_{35}G_{65})_p$	5.57, 3.26	H/O	11.14	6.52	*	1.160±0.007
	G'_4		28%	$s-(T_{28}G_{72})_p$	5.57, 3.20	H/O	11.14	6.40	*	1.166±0.007
	$(TG)_3$	50%	51%	$s+(T_{51}G_{49})_p$	5.52, 5.23, 3.23, 3.10	PH/O	11.05	6.20	*	1.19±0.02
	$(TG')_3$		52%	$s-(T_{52}G_{48})_p$	5.52, 5.23, 3.24, 3.18	PH/O	11.05	6.37	*	1.172±0.008
	T_2	100%	100%	$s(T_{100})_c$	10.23, 5.12, 5.00, 4.60, 3.83, 3.63, 3.59, 3.41, 3.07, 2.93, 2.87, 2.76, 2.57, 2.29, 2.13	O/O	10.23	5.73	5.16	1.164±0.004

[a] H = hexagonal; O = orthorhombic; PH = pseudo-hexagonal.

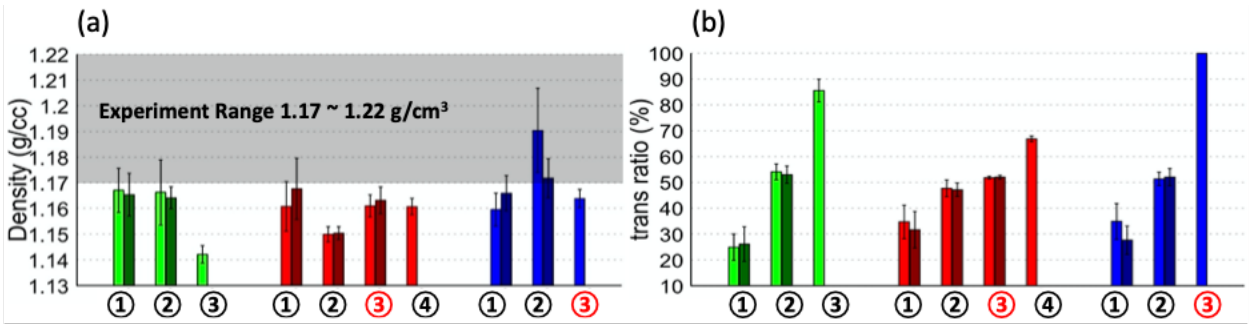

Figure 3.9. (a) Density and (b) *trans* ratio of all the systems. Each value is the average over 10 systems started with same chain conformation but different rotation of the chain axes, each system also averaged over 5000 frames within a 500 ps MD simulation at 300K and 1 atm. ***c**-axis-ordered structures are highlighted using red color.* Figure adapted from Ref. [133].

Torsion angle distribution analysis of skeletal bonds after relaxation for these pseudo-crystalline structures indicates that even though the structures lost chain axis periodicity and resulted in changed *trans* ratio, the torsion angle distribution along the chains remains similar to the initial structures. Several sample analyses are shown in Figure 3.10.

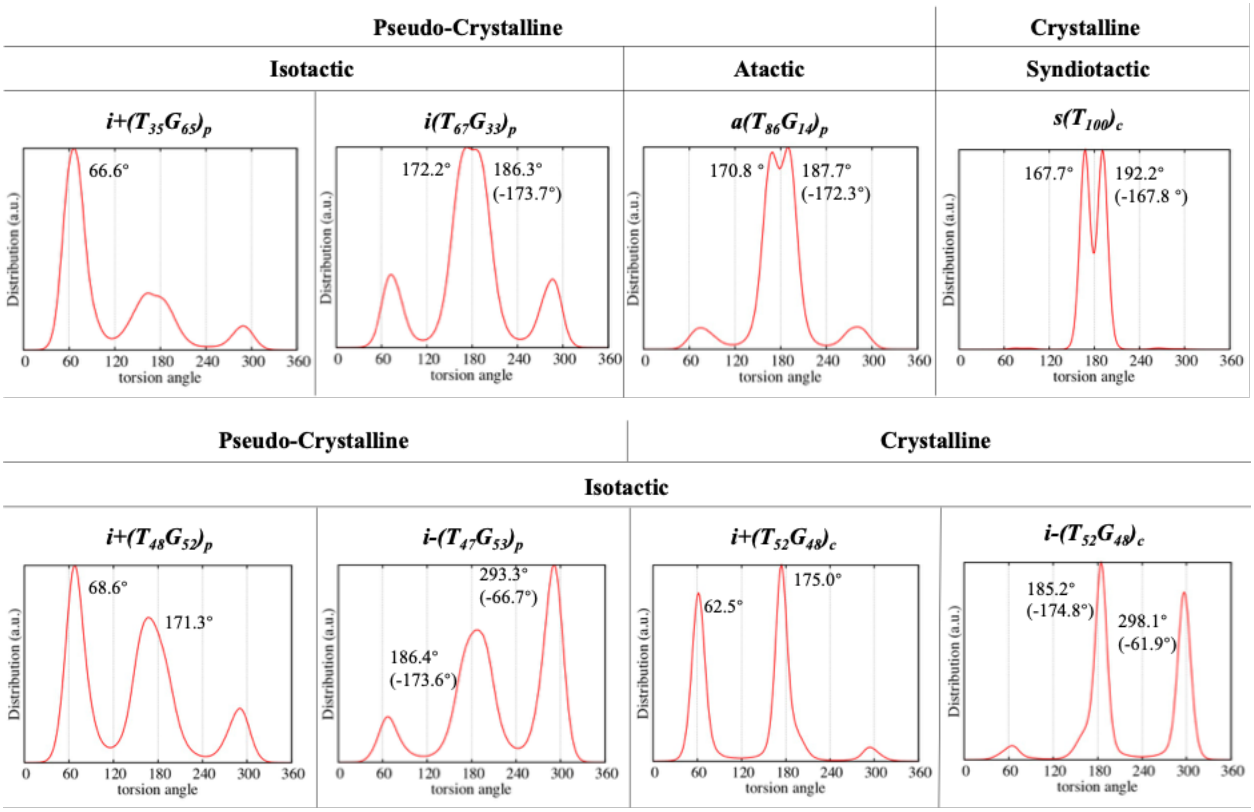

Figure 3.10. Torsion angle distribution. Figure adapted from Ref. [133].

We find that peaks around ±60° and 180° are broader if the structures lost chain axis periodicity. Also, the peaks of torsion angle distribution deviate from the ideal ±60° and 180° values and for high *trans* ratio structures the distribution around 180° splits into two peaks. This mismatch between the torsion angle might be caused by the intra- and inter-molecular interactions especially the C ≡ N dipoles and it becomes more obvious in ***c***-axis-ordered syndiotactic planar zig-zag conformation (***s*(T$_{100}$)$_c$**) as the peaks of the torsion angle distribution narrow.

In order to characterize the sequence of the *t(±)* conformations for these three high *trans* ratio structures, we performed a torsion angle correlation analysis. We calculated the probability of finding *t(±)* conformation at the nearest neighbors of a certain torsion isomer (see Figure 3.11). We found that with varying tacticities, the sequence distribution of the *t(±)* conformations are very different for these three high *trans* ratio structures. For atactic ***a*(T$_{86}$G$_{14}$)$_p$**, the *t*+ and *t*- seem to be equally random distributed along the chain and for isotactic ***i*(T$_{67}$G$_{33}$)$_p$**, the sequence tends to be *t*+, *t*- alternatively. While, for syndiotactic ***s*(T$_{100}$)$_c$** structure, which also considered as ***c***-axis-ordered planar zig-zag, the sequence is {*t*+,*t*+,*t*-,*t*-}. This indicates that syndiotactic planar zig-zag conformation actually has a unit of two monomers along ***c*** axis which is about 5.16 Å.

3.3.2 Diffraction patters: molecular packing

The good agreement between the predicted densities and experiments provides an initial validation of our approach, we now perform a detailed structural comparison of the predicted structure with experimental ones. We compare calculated XRD patterns for all the predicted structures with experimental results. As expected, the experimental values depend on processing conditions and our various structures with varying *trans* ratios and tacticities correspond to distinct experimental conditions. The theoretical values are extracted from our predicted structures using the LAMMPS [136] built-in command [146] with wavelength of incident radiation 1.54 Å, results are averaged 100 frames of atom position trajectory within a 500 ps MD simulation at 300 K and 1 atm for each selected system. Figure 3.12 shows the predicted XRD patterns for all structures.

For most cases, see Table 3.4, Figure 3.12(a)-(c) and Figure 3.13(a)-(d), we find two main peaks with position and relative intensity consistent with a hexagonal cell pattern. In the syndiotactic structures ***s*+(T$_{51}$G$_{49}$)$_p$** and ***s*-(T$_{52}$G$_{48}$)$_p$**, the main two peaks split into d_{200} and d_{110} for the first peak and d_{310} and d_{020} for the second peak. [Figure 3.13(e)(f)] This is due to the distortion of the hexagonal lattice with $\mathbf{a} > \sqrt{3}\,\mathbf{b}$. The cell parameter ***a*** of all structures is in range of

10.53 ~ 11.32 Å and ***b*** in range of 6.01 ~ 6.77 Å. And as *trans* ratio increases, the cell parameters ***a*** and ***b*** decrease as the chain becomes narrower and more extended. The simulated XRD pattern for $a(T_{86}G_{14})_p$ and $i(T_{67}G_{33})_p$, with d_{200} ~ 5.27 Å, and d_{020} ~ 3.00 Å or 3.07 Å [Figure 3.12(c)], show good agreement with as-spun PAN nanofibrous yarn [147] with d_{200} ~ 5.21 Å, d_{020} ~ 3.02 Å. While the density of $a(T_{86}G_{14})_p$ is relatively low (1.142 ± 0.004 g/cm^3), the predicted isotactic structures with high *trans* ratios are good models for the crystalline region of PAN precursor fibers.

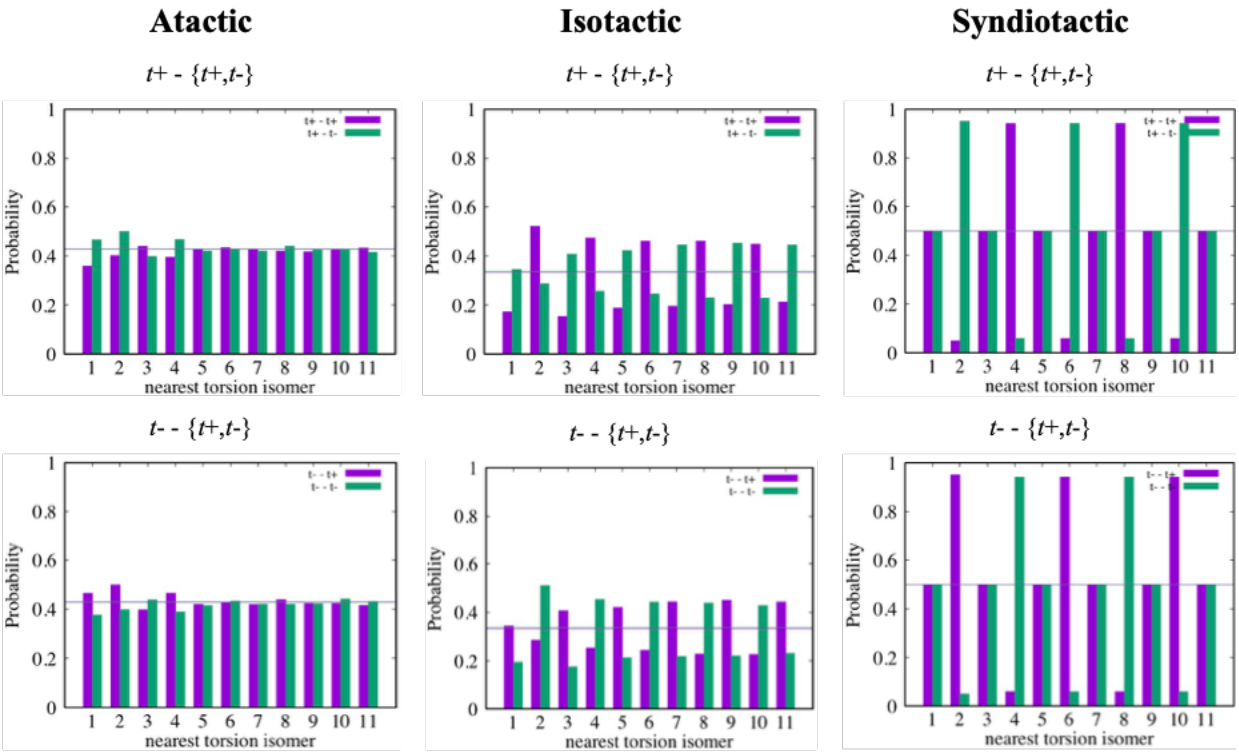

Figure 3.11. *t(±)* conformation correlation analysis for high *trans* ratio structures. *Overall probability of finding a certain t(±) conformation is label as a straight line in all the plots.* Figure adapted from Ref. [133].

Interestingly, the calculated XRD pattern for low *trans* ratio structures (Figure 3.12(a), with d_{200} in range of 5.57 ~ 5.66 Å and d_{020} in range of 5.20 ~ 5.39 Å) show good agreement with those of PAN nanoparticles obtained by in situ emulsion sonication technique [148] that exhibit d_{200} ~ 5.81 Å, d_{020} ~ 3.43 Å. Finally, pseudo-crystalline structures with *trans* ratio around 50% match the unit cell parameters reported by H. Rein cited by W. Kast. [149] with d_{200} ~ 5.34 Å, d_{020} ~ 3.09 Å in 1949. This experimental work is early in the development of PAN fibers before

they were widely used as carbon fiber precursors; our simulations indicate that these PAN samples were not fully drawn or stretched.

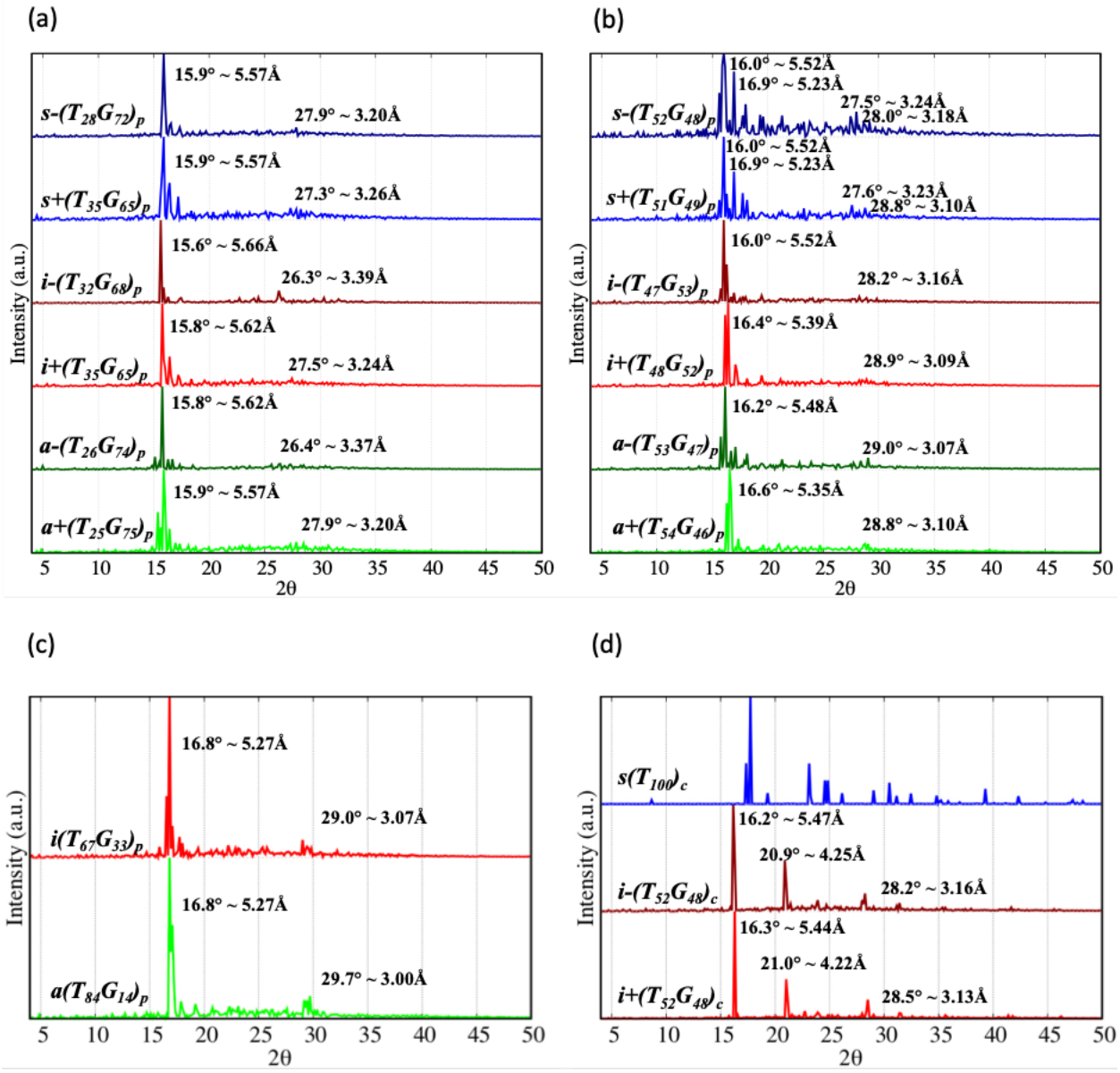

Figure 3.12. Simulated XRD pattern for (a) pseudo-crystalline structures started with $\boldsymbol{G_4}$ (*trans* ratio 0%) conformations; (b) pseudo-crystalline structures started $\boldsymbol{(TG)_3}$ (*trans* ratio 50%) conformations; (c) pseudo-crystalline structures started $\boldsymbol{T_2}$ (planar zig-zag, *trans* ratio 100%) conformations and (d) three ***c***-axis-ordered structures. Figure adapted from Ref. [133].

For the ***c***-axis-ordered structures $\boldsymbol{i\text{+}(T_{52}G_{48})_c}$ and $\boldsymbol{i\text{-}(T_{52}G_{48})_c}$, another peak, $\boldsymbol{d_{111}}$, emerges due to the chain periodicity along the chain axis, see Figure 3.12(d) and Figure 3.13(g). While,

additional peaks appear for syndiotactic planar zig-zag ($s(T_{100})_c$) [Figure 3.12(d)]. An orthorhombic cell with a = 10.23 Å, b = 5.73 Å and c = 5.16 Å best fits these peaks with indexes and corresponding d-spacings given in Table 3.5.

A few experimental results [150–152] are consistent with this type of pattern, and debate about these patterns has been ongoing for half a century [153,154]. Efforts following the initial publications were unable to reproduce these XRD patterns and speculated that the patterns with additional peaks are due to co-crystallization of the solvent [153,154]. Our results show that such multi-peak-fingerprint could be naturally in syndiotactic PAN samples and may not be due to co-

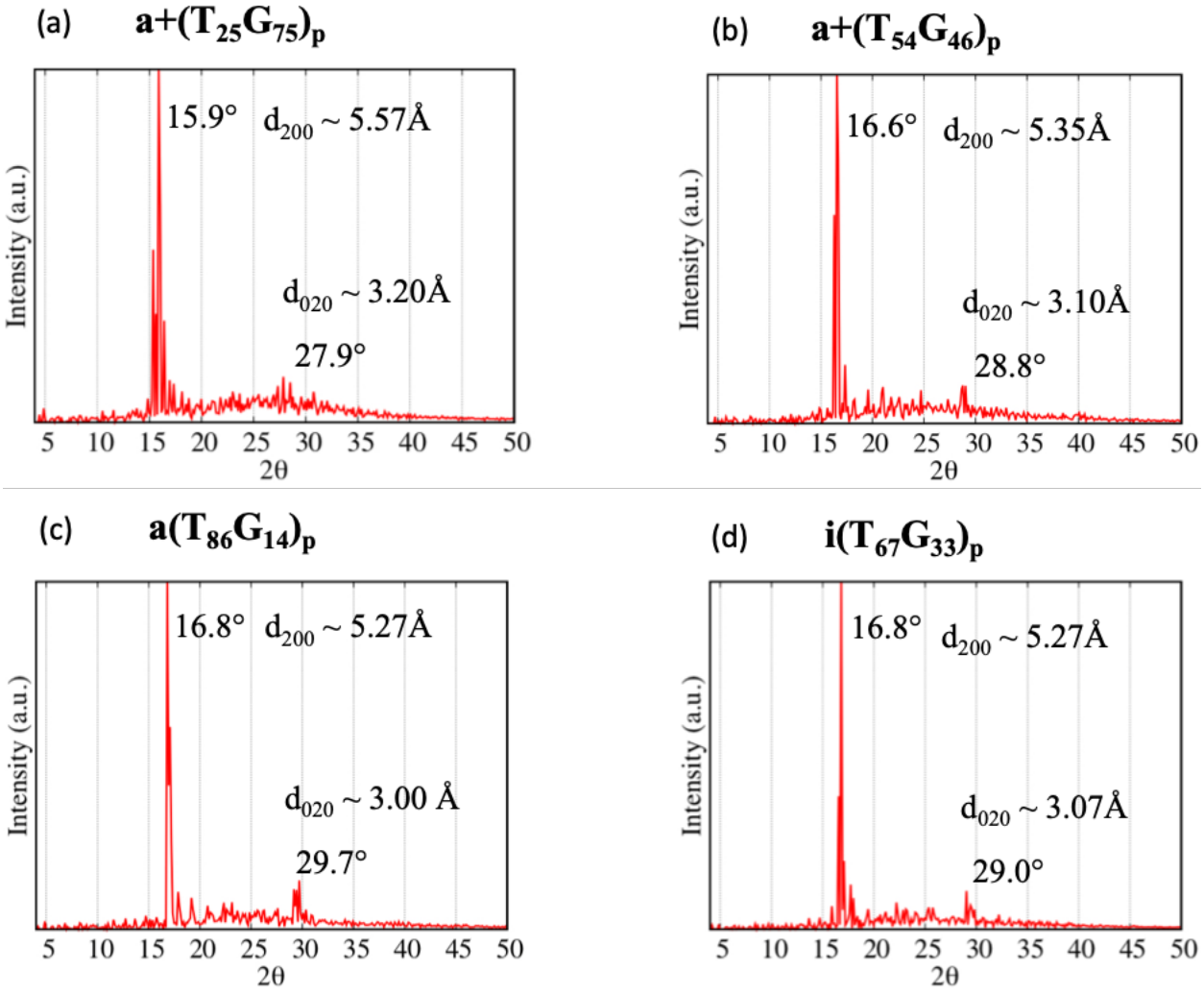

Figure 3.13. Simulated XRD pattern for (a) $a+(T_{25}G_{75})_p$, (b) $a+(T_{54}G_{46})_p$, (c) $a(T_{86}G_{14})_p$, (d) $i(T_{67}G_{33})_p$, (e) $s+(T_{51}G_{49})_p$, (f) $s-(T_{52}G_{48})_p$, (g) $i+(T_{52}G_{48})_c$ and (h) syndiotactic planar zig-zag ($s(T_{100})_c$).

Figure 3.13. continued

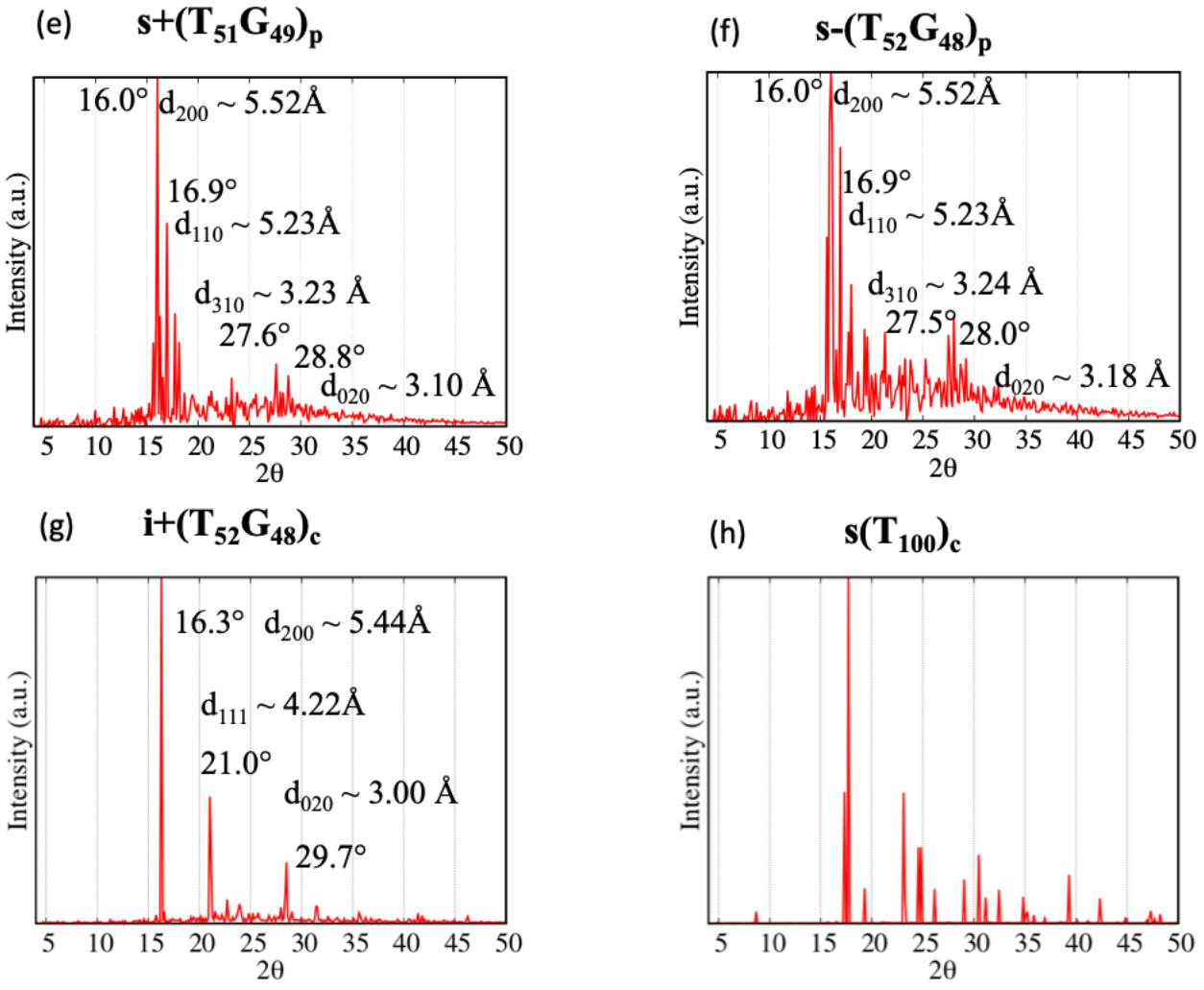

crystallization with the solvent. Quite interestingly, NMR studies in Kumamaru F., etc. [150] clearly indicated that their sample contains more syndiotactic diads than isotactic ones, which is not very usual [128]. Furthermore, Colvin et al. [151] also suggested the probability of syndiotactic configuration to account for their XRD patterns. Although Klement J. J. et al. [152] did not provide tacticity information, the pattern with total of 13 reflections is already very unique compared with other 'standard' two-peak pattern associated with the hexagonal polymorph and also has been questioned for co-crystallization [153,154]. Detailed XRD pattern and ***d***-spacings comparison of these experimental work and our syndiotactic planar zig-zag sample is illustrated in Figure 3.14 and Table 3.6. These all had proposed a large orthorhombic cell almost twice as ours. Based on

our observation of the structure [Figure 3.8(b) syn Planar zig-zag (T_2)] and indexing (Table 3.5), we believe that a small unit cell is more appropriate.

Table 3.5. Index and ***d***-spacing for syndiotactic planar zig-zag $s(T_{100})_c$. Table reproduced from Ref. [133].

Index	*d*-spacing in Å
100	10.23
200	5.12
110	5.00
101	4.60
011	3.83
101	3.63
111	3.59
300	3.41
211	3.07
310	2.93
020	2.87
120	2.76
002	2.57
112	2.29
411	2.13

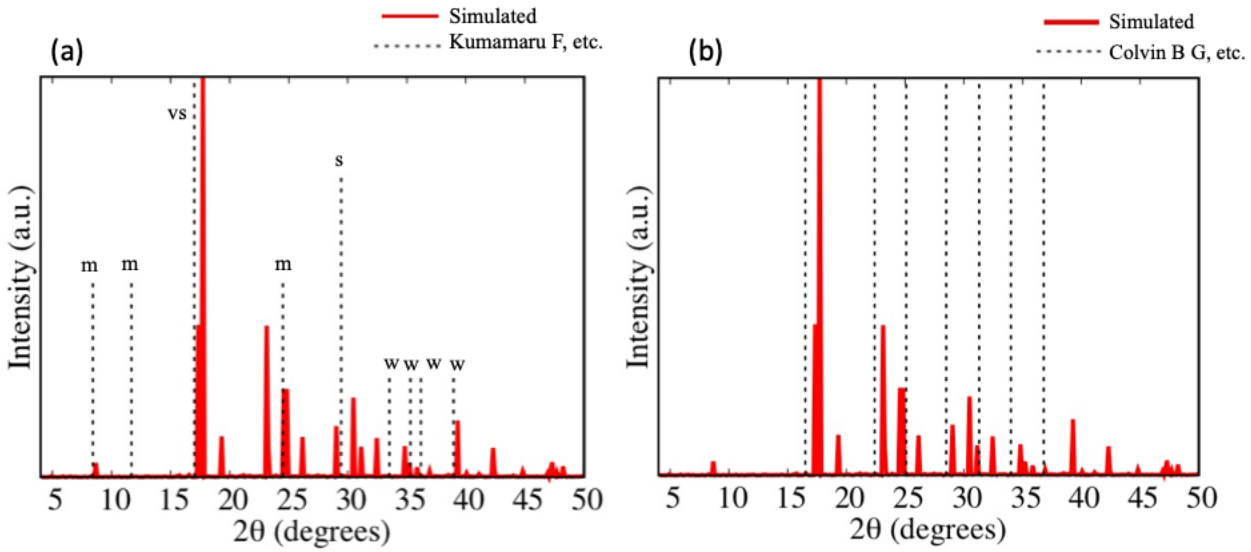

Figure 3.14. XRD pattern comparison of syndiotactic planar zig-zag conformation with experimental work from (a) Kumamaru F., etc. [150] and (b) Colvin B. G., etc. [151] *Black dash lines are representing the peak positions and relative intensities are shown as vs-very strong, s-strong, m-medium, w-weak in (a), but not shown in (b) due to lack of intensity information in its original paper.* Figure adapted from Ref. [133].

Table 3.6. Comparison among the ***d***-spacing of PAN with multi-peak patterns from experiment with ours. Table reproduced from Ref. [133].

Reference	Unit Cell in Å			d-spacing in Å
	a	b	c	
[150]	21.0	11.9	5.04	10.50, 7.57, 5.21, 3.63, 3.03, 2.67, 2.54, 2.48, 2.31
[151]	21.48	11.55	7.096	5.37, 3.96, 3.54, 3.13, 2.85, 2.63, 2.44, 1.774
[152]	21.18	11.60	*	10.07, 7.81, 5.36, 5.05, 3.91, 3.64, 3.14, 3.02, 2.90, 2.87, 2.65, 2.53, 2.03
Our work	10.23	5.73	5.16	10.23, 5.12, 5.00, 4.60, 3.83, 3.63, 3.59, 3.41, 3.07, 2.93, 2.87, 2.76, 2.57, 2.29, 2.13

Current PAN polymerization methods do not produce large syndiotactic stereoregular structures thus recent experiment work did not produce the multi-peak XRD pattern. Studies show that free-radical polymerization as commercial manufacture adopted method mainly produces atactic configurations [11,128] and other methods like canal-polymerization produces isotactic ones [128,155]. This seems very surprising as the nature of $C \equiv N$ dipoles would prefer anti-parallel arrangements just as syndiotactic stereos. It is still not clear why syndiotactic PAN is difficult to produce during these types of polymerization process. Our simulations indicate that drawn PAN precursors with high syndiotactic yield would result in more stable structure in crystalline region and may potentially lead to a higher degree of crystallinity after spinning and stretching, but this assumption requires further experimental work to validate. Moreover, whether high syndiotactic concentration would improve the mechanical properties of the final product is also a question that needs to be answered.

3.3.3 Diffraction patters: chain conformation

In order to further characterize the structures and compare with experiments we now go beyond chain packing and unit cell properties. Figure 3.15 shows the calculated scattering function with wavevectors appropriate to characterize the intra-molecular structure for all samples with experimental comparison [108]. Experimental data were obtained using wide-angle X-ray scattering (WAXS) in order to capture the detailed information about chain conformations [108].

Samples resulted in pseudo-crystalline structures are in excellent agreement with experimental data, both in terms of the peak positions and the relative intensities. Based on scattering functions, it is very difficult to distinguish between tacticities and chiralities for pseudo-crystalline PAN structures using XRD methods (Figure 3.15(a)-(c)). While, due to the periodicity

along ***c*** axis without considering any amorphous interruption, XRD patterns of ***i+(T52G48)c***, ***i-(T52G48)c*** and ***s(T100)c*** are having too much sharp peaks compared with the experiment sample (Figure 3.12(d)). Therefore, we believe that most of the experimental samples are consists of pseudo-crystalline structures without any ***c*** axis periodicity.

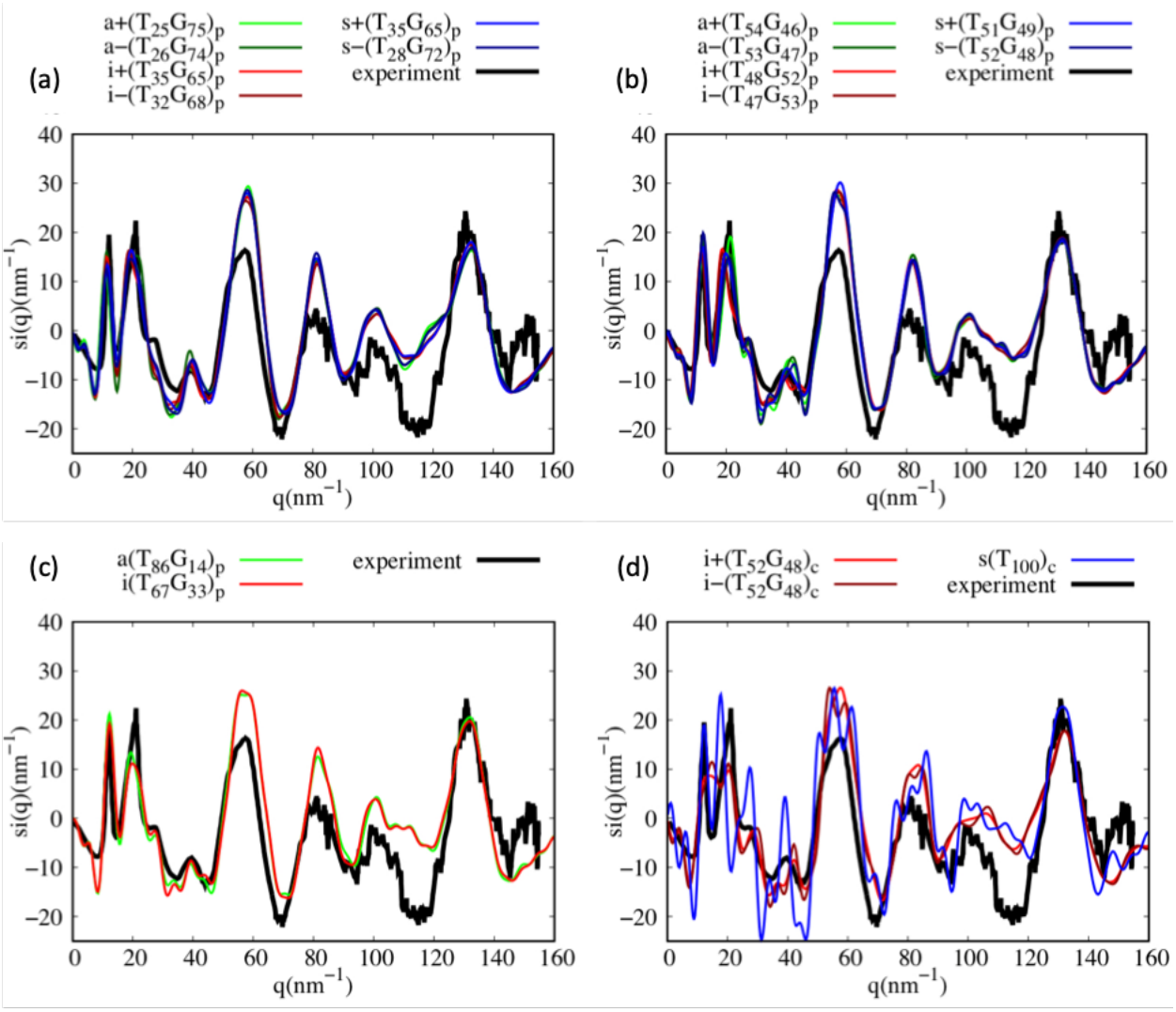

Figure 3.15. Calculated scattering function for (a) pseudo-crystalline structures started with ***G4*** (*trans* ratio 0%) conformations; (b) pseudo-crystalline structures started ***(TG)3*** (*trans* ratio 50%) conformations; (c) pseudo-crystalline structures started ***T2*** (planar zig-zag, *trans* ratio 100%) conformations and (d) three ***c***-axis-ordered structures. All samples are with experimental comparison from Ref. [108]. Figure adapted from Ref. [133].

3.4 Stability and mechanical properties

3.4.1 Stability

We now focus on the energetics of the structures to understand their relative stability. Figure 3.16 compares the energetics of all the structures; the total potential energy (first row) is divided into covalent (second row), electrostatics (third row) and van der Waals (fourth row). Each of the energy components are divided into intra-molecular (center column) and inter-molecular (right column). Each value is the average over 10 systems started with same backbone helix structure, and each system also be averaged over 5000 frames within a 500 ps MD simulation at 300K and 1 atm. The structures that remain periodic along the ***c*** axis after relaxation [$\boldsymbol{i+(T_{52}G_{48})_c}$, $\boldsymbol{i-(T_{52}G_{48})_c}$ and syndiotactic planar zig-zag ($\boldsymbol{s(T_{100})_c}$)] exhibit the lowest energy within their tacticity families. It turns out that the $\boldsymbol{i+(T_{52}G_{48})_c}$ and $\boldsymbol{i-(T_{52}G_{48})_c}$ structures are very stable as single chain conformations but the packing does not significantly lower the energies. However, syndiotactic planar zig-zag ($\boldsymbol{s(T_{100})_c}$) conformation is not only very favorable as single chain but also very favorable in terms of inter-molecular packing. Other than these ***c***-axis-ordered structures, the potential energy of the pseudo-crystalline crystalline PAN decreases as *trans* ratio increases, indicating that drawing can reduce the energy of the crystalline regions in spun PAN fibers. The covalent energy is the main contribution of the potential energy and has the similar trend with the potential energy. One of the other contributions comes from electrostatics energy and overall it decreases as the *trans* ratio increases. Van der Waals interactions contribute the least to the energy difference between structures and they tend to stabilize structure with low *trans* ratios. From energetics point of view, especially from electrostatics energies, atactic and isotactic high *trans* ratio structures are very unfavorable in terms of single chain conformations, but the packing lowers the electrostatics energies significantly and makes them result in relatively low energy structures.

3.4.2 Mechanical properties

It is widely believed that stretching helps improve stiffness of the precursor as well as the final carbon fiber processed from it [15,16,156]. In most of the cases, stretching, as a modification method of amorphous region in spun fiber, helps reduce the filament diameter of a PAN precursor, improve the orientation of the molecular chains, reduce the bulk volume allowing a quicker fiber heat-up rate with better control of a possible exotherm and limit the formation of skin-

Figure 3.16. Total, intra- and inter-molecular potential, covalent, electrostatics and van de Waals energy of all the systems. The total energies are the sum of the intra- and inter-molecular energies and the potential energy is the sum of 3 others energy terms. ***c**-axis-ordered structures are highlighted using red color.* Figure adapted from Ref. [133].

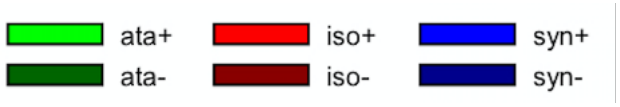

ata: ①+:***a+(T$_{25}$G$_{75}$)$_p$***, -:***a-(T$_{26}$G$_{74}$)$_p$***, ②+:***a+(T$_{54}$G$_{46}$)$_p$***, -:***a-(T$_{53}$G$_{47}$)$_p$***, ③***a(T$_{86}$G$_{14}$)$_p$***;

iso: ①+:***i+(T$_{35}$G$_{65}$)$_p$***, -:***i-(T$_{32}$G$_{68}$)$_p$***, ②+:***i+(T$_{48}$G$_{52}$)$_p$***, -:***i-(T$_{47}$G$_{53}$)$_p$***, ③+:***i+(T$_{52}$G$_{48}$)$_c$***, -:***i-(T$_{52}$G$_{48}$)$_c$***, ④***i(T$_{67}$G$_{33}$)$_p$***;

syn: ①+:***s+(T$_{35}$G$_{65}$)$_p$***, -:***s-(T$_{28}$G$_{72}$)$_p$***, ②+:***s+(T$_{51}$G$_{49}$)$_p$***, -:***s-(T$_{52}$G$_{48}$)$_p$***, ③***s(T$_{100}$)$_c$***

Figure 3.16. continued

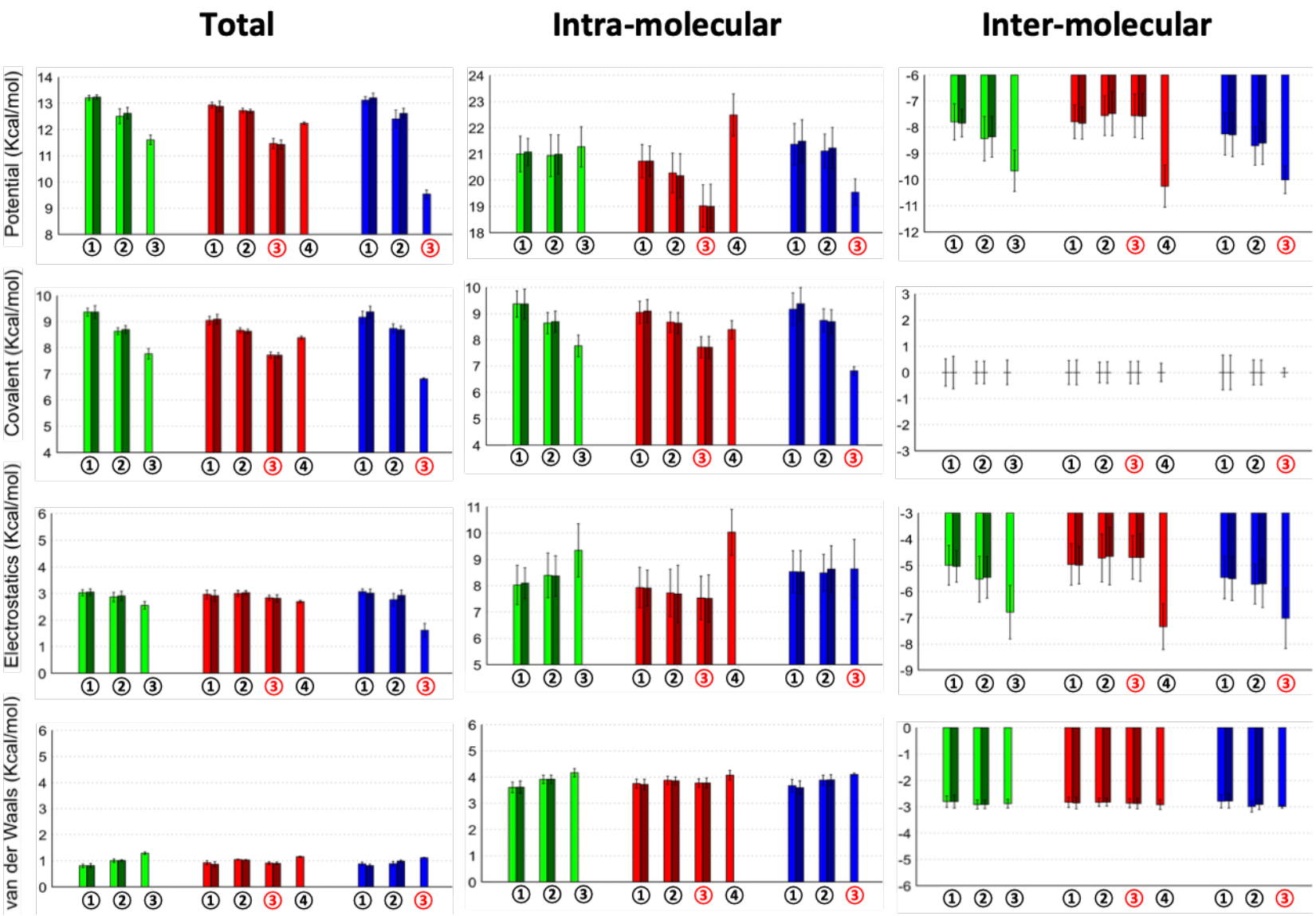

core [11,157]. Since the simulations provide interesting information regarding the correlation between the *trans* ratio of the chains and the XRD pattern as well as several experimental studies on drawn PAN fiber precursors [119,154] also observed similar evolution of XRD patterns during stretching, we assume that stretching during spinning and subsequent processing would also has a key effect on crystalline region.

We use the calculation method described by [158] to calculate the tensile and transverse modulus but only elongation information was used when calculating tensile modulus. Raw data with tensile modulus and transverse modulus versus trans ratio is shown in Figure 3.17. Each data point in Figure 3.18 are average over the range separated by the grey dash lines in Figure 3.17.

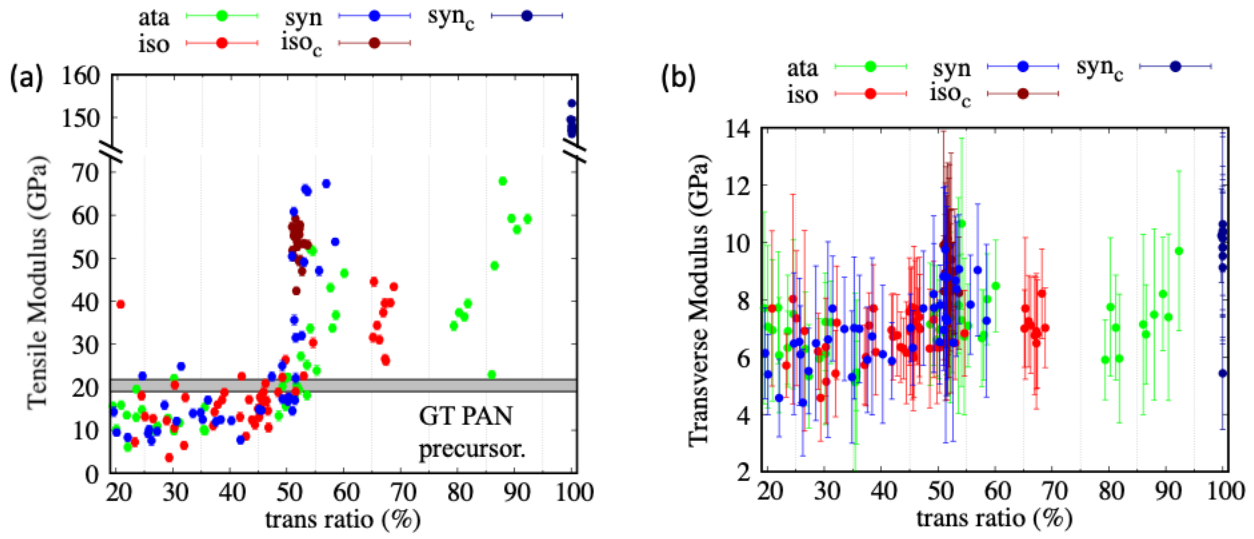

Figure 3.17. (a) Tensile modulus and (b) transverse modulus versus trans ratio. Grey region in (a) represents the experimental comparison from Ref. [14].

After calculation of the tensile modulus for all the systems from stress-strain curves, we plot it as function of the *trans* ratio in Figure 3.18(a). The simulation results are compared with the Georgia Tech (GT) gel-spun PAN precursors modulus of 20.7 ± 1.1 GPa [14]. Despite the ***c***-axis-ordered isotactic structure having large stiffness of 54 ± 4 GPa and syndiotactic even higher at 148 ± 2 GPa, all other structures are in range of 10 - 60 GPa, which is reasonable compared with GT PAN precursors without considering amorphous region. We find a clear trend that the stiffness of the crystalline region increases with increasing *trans* conformations. This is a further validation that high *trans* ratio is the underlying reason behind the precursor high stiffness. Based on our

results and several experimental observations before and after stretching, we speculate that another function of stretching during spinning and subsequent processing is to help extend the chain to higher *trans* ratio and improve the chain conformation to its all *trans* form which is usually refer to planar zig-zag conformation. With the backbone configuration of this planar zig-zag form similar to the main product of stabilization process – the ladder structures [6], we believe such chain conformations could facilitate the stabilization reactions and improve the mechanical properties of the final product by forming more ladder structures during stabilization.

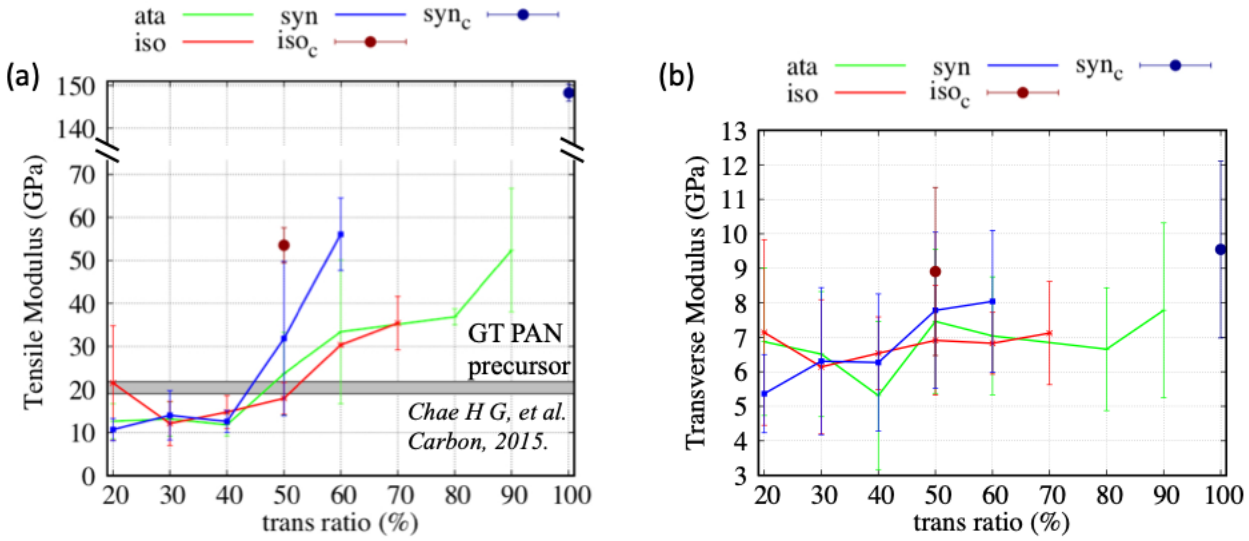

Figure 3.18. (a) Tensile modulus and (b) transverse modulus versus *trans* ratio. Grey region in (a) represents the experimental comparison from Ref. [14]. Figure adapted from Ref. [133].

In order to further validate the effect of stretching in crystalline region, we use isothermal, isobaric MD at four different conditions ---- 400 K with 20 MPa stretching, 400 K with 200 MPa, 450 K with 20 MPa and 450 K with 200 MPa. Stretching is applied along fiber axis (***c*** direction) for 1 ns and 1 atm condition is used at ***a***, ***b*** direction. Temperature conditions are using stretching conditions in Ref. [15]. While stretching conditions are usually considered as commercial secrets, see patents cited in Ref. [7], we are using less than one half of the tensile strength reported in Ref. [156].

We analyzed the trans ratio evolution during stretching under these conditions for all structures and selected results are shown in Figure 3.19. We found that for ***c***-axis-ordered structures, stretching does not change the *trans* ratio especially for syndiotactic planar zig-zag

structure $s(T_{100})_c$ (see Figure 3.19(d)-(f)). But for pseudo-crystalline structures starting from low and medium trans ratios, stretching would increase the trans ratio of the backbone conformations (Figure 3.19(a),(b)) while the trans ratio would drop for structures starting with high trans ratio (Figure 3.19(c)). Since the simulation time scale is limited to nanoseconds, based on that, we plot the trans ratio evolution for all the structures under different conditions. Figure 3.20 shows the trans ratio evolution for all the pseudo-crystalline structures under 450 K with 200 MPa stretching. By evaluating the gap between medium and high trans ratios, we could speculate the final trans ratio range under different stretching conditions. Results are shown in Figure 3.21. This could be considered that for pseudo-crystalline structures stretching does have impact on chain conformations, particularly *trans* ratios, in crystalline region and resulting *trans* ratios would vary under different stretching conditions with various tacticities.

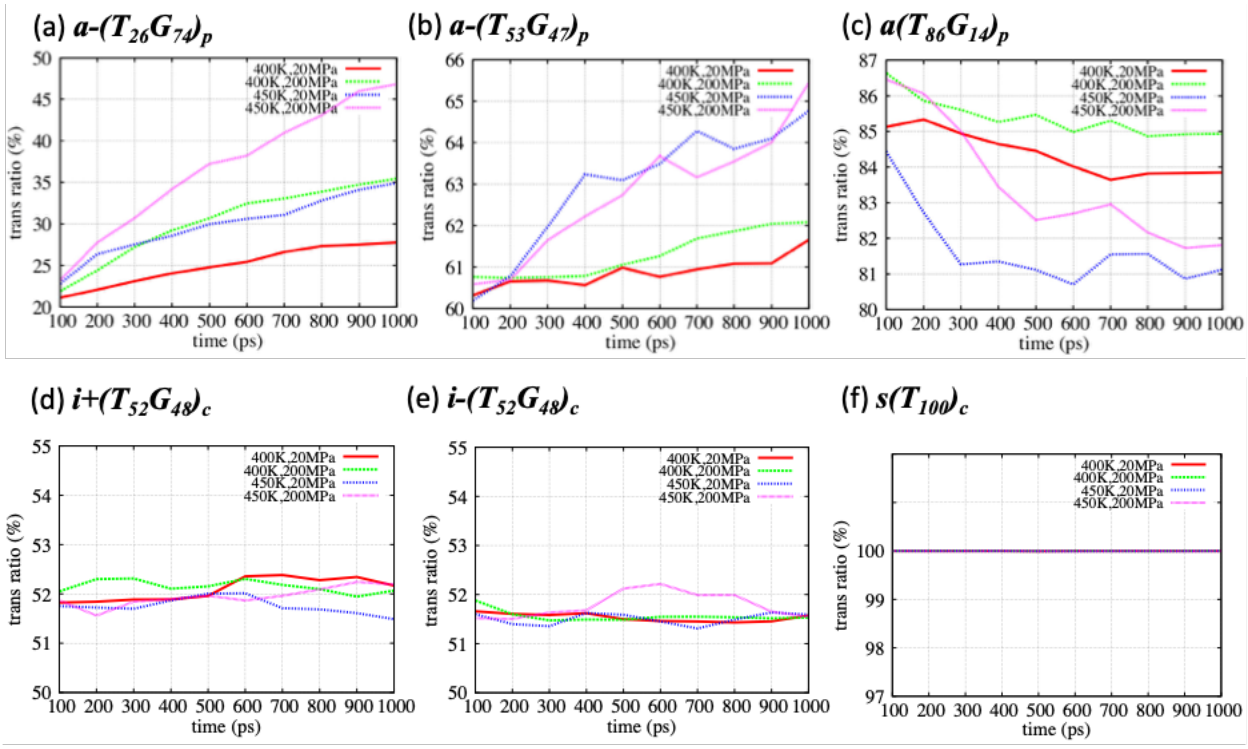

Figure 3.19. *trans* ratio evolution under different stretching conditions for (a) $a\text{-}(T_{26}G_{74})_p$, (b) $a\text{-}(T_{53}G_{47})_p$, (c) $a(T_{86}G_{14})_p$, (d) $i\text{+}(T_{52}G_{48})_c$, (e) $i\text{-}(T_{52}G_{48})_c$ and (f) $s(T_{100})_c$.

We also computed the transverse modulus of the structures and plot it versus *trans* ratio in Figure 3.18(b). The predicted transverse modulus for pseudo-crystalline structures are in range of $3 \sim 11$ GPa, while for isotactic ***c***-axis-ordered structures the modulus is at 9 ± 3 GPa and

syndiotactic ***c***-axis-ordered structures slightly higher at 10 ± 3 GPa. We are unaware of transverse moduli of PAN fibers. The predicted transverse modulus of ladder structures during carbonization in Ref. [158] have been reported to be in range of 1.5 ~ 5.5 GPa. Since we did not find any precursors transverse modulus information, our comparison is based on our previous predicted values and experimental values of 6 ~ 10 GPa for high strength [159] and 1 ~ 3 GPa for high modulus [160] final carbon fiber products. Our predicted values for precursors are twice bigger than carbonized structures. This is probably due to the Coulomb contribution, especially from C ≡ N dipoles, of the inter-molecular interactions between PAN chains.

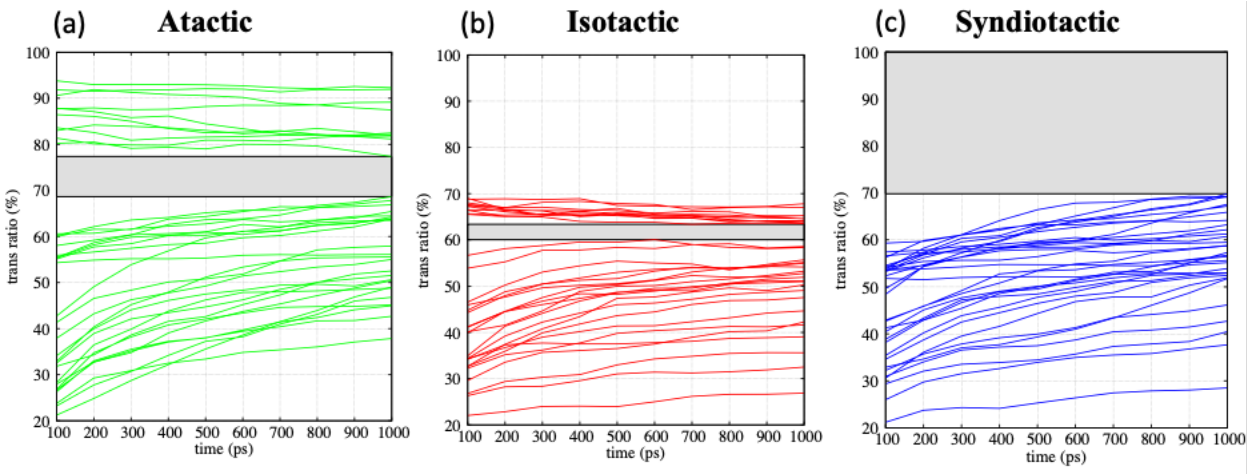

Figure 3.20. *trans* ratio evolution for (a) atactic, (b) isotactic and (c) syndiotactic pseudo-crystalline structures under 450 K with 200 MPa stretching. *Dark region represents the gap between the increasing trans ratio and decreasing trans ratio*.

3.5 Conclusion

Using MD simulations, we successfully predicted the molecular structure of the crystalline regions of spun PAN fibers of interest as carbon fiber precursor. A hexagonal lattice with pseudo-crystalline chains, with *trans* ratio in range of 65% - 85% would be a proper model. A pseudo-hexagonal (orthorhombic) cell of ***a*** = 10.54 Å and ***b*** = 6.10 Å are found. Structures with low *trans* ratios would be a rational model for crystal structure in PAN nanoparticles and models with *trans* ratios around 50% would be used to describe PAN polymers made by less drawn. Stiffness of the crystalline region increases with increasing *trans* ratio. Based on the correlations between XRD pattern and tensile modulus with *trans* ratios, we believe that stretching as modification of spun

fiber improves not only the filament diameter and molecular orientation, but also the *trans* ratio of the skeletal bonds. With higher *trans* ratios, the pre-oxidized structure would gain advantages during stabilization due to its resemblance to the resulting.

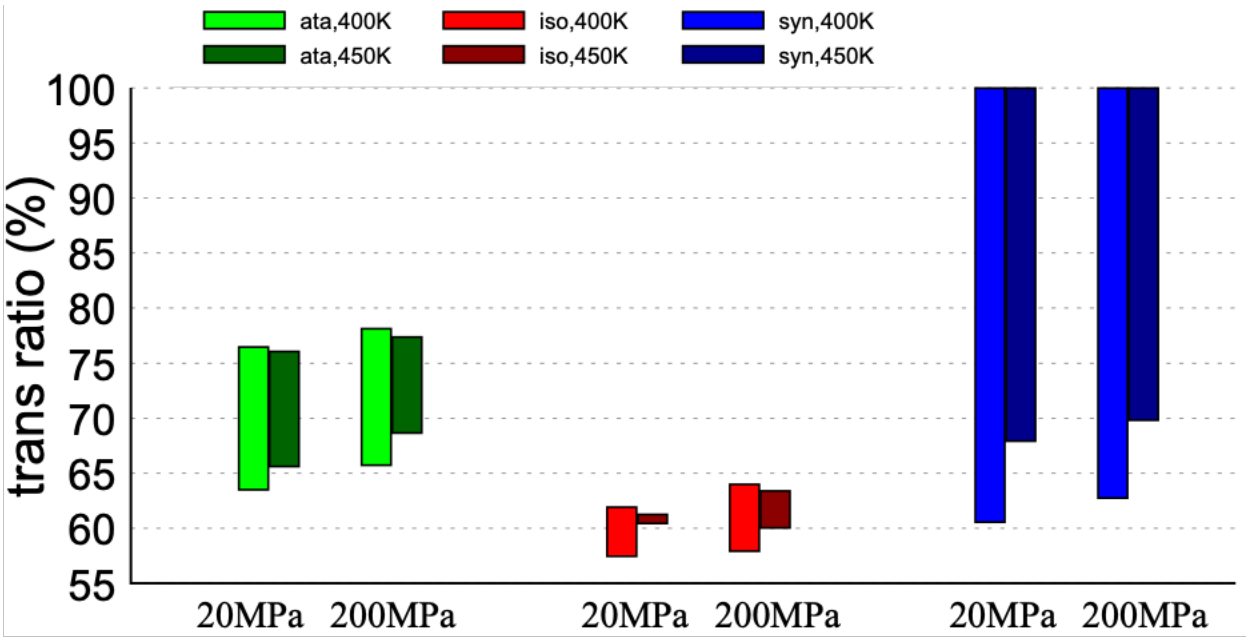

Figure 3.21. *trans* ratio gap under different stretching conditions.

During our study, we found that syndiotactic systems with planar zig-zag conformation result in ***c***-axis-ordered structure and have the lowest energy and best mechanical performance among other investigated structures. It turns out that syndiotactic planar zig-zag form is not only very favorable as single chain conformation but also very favorable in terms of inter-molecular packing. After detailed comparison with several experimental work [150–152] which have been doubted for co-crystallization with the solvent by Bashir Z., etc. [153,154], we found that the simulated XRD pattern of our syndiotactic planar zig-zag samples is in decent agreement with theirs. We suggest that the XRD pattern may be comformation-dependent and the multi-peak-fingerprint shown in their XRD patterns is probably not due to co-crystallization. It seems that the differences of the XRD pattern between syndiotactic planar zig-zag structures and other pseudo-crystalline structures have never been recognized and this could be the main reason causing the long-time discrepancy on the crystal structure of PAN. Further experimental works are required to

understand the role of syndiotactic planar zig-zag conformation in PAN-based carbon fiber processing and properties.

4. NOVEL MODE OF NON-CRYSTALLOGRAPHIC BRANCHING IN THE INITIAL STAGES OF POLYMER FIBRIL GROWTH

4.1 Introduction

Crystallization originates from the collective action of large numbers of particles and results in a microstructure that ultimately controls materials properties. Understanding this process is critical in a wide range of fields, from structural materials [161] and food processing [162], to biology [163] and medicine [164]. Recent experimental characterization breakthroughs enabled an exquisite understanding of crystal nucleation and growth [165]. However, most properties are governed by the crystalline microstructure [44] and a molecular understanding of its development during crystallization is still lacking. This gap is particularly wide in polymers that often crystallize into spherulites, a fascinating and ubiquitous polycrystalline structure formed by repeated branching of crystallites. Despite great efforts, the formation mechanism and kinetics of polymer crystallization are still not well understood, as polymer crystallized from the melt usually takes the form of spherulites. This gap stems from the lack of understanding of the molecular scale mechanisms of the crystallization and the predictive simulation of these processes. The purpose of this chapter is to introduce the current understanding of polymer crystallization kinetics and polymer spherulite formation, as well as our use of large-scale molecular dynamics (MD) simulations to capture non-crystallographic branching process, which is responsible for polymer spherulites formed during polymer process. We found that in the early stages of growth, the thickening process of the parent lamella dominates, leading to significant deformation in the nearby area. This deformation greatly changes the molecular arrangement in its vicinity and induces the nucleation with the chain orientation similar to the primary crystal grain. The predicted misalignment is in good agreement with the experiment. With ongoing debate over classic Lauritzen-Hoffman theory of polymer crystallization, we identified a novel mode of non-crystallographic branching during crystallization and provide a more fundamental understanding of the development of polycrystalline structures, including the ubiquitous spherulite. [166]

4.2 Methods and simulation details

While mechanism of polymer crystallization differs with polymer materials and complex situations, we focus our studies on PE system with consideration of quasi-2D crystallization only contains edge-on lamellae direction. PE as the simplest polymer structure having large structure flexibility that results in faster crystallization processes as compared with other polymers. None of the mechanisms associated with crystallization described here are dependent on any specific property of PE or on its structure; thus, we believe the results are general across polymers of different chemistries and architectures. Our approach to predict polymer crystallization behavior starts with generating coexistence model of PE with primary nuclei embryo in the center of simulation box and amorphous melt surrounding. To capture the effect of temperature and given a melting temperature T_m = 420 K for our model (in good agreement with experiments) we performed simulations at 400, 380, 360, and 340 K. [166]

4.2.1 Generating crystal-melt coexistence model of PE

In order to prepare the initial models for the MD simulations of crystallization, we started with perfect crystal consisting of 70 PE chains with 80 monomers (C_{160}) per chain built by replicating the orthorhombic unit cell 5 times along [100], 7 times along [010], and 40 times along [001] (chain direction), see Figure 4.1 and Table 4.1 [167]. The crystalline structures are relaxed at the desired recrystallization temperatures (340K, 360K, 380K and 400K) using isothermal-isochoric MD for 50ps followed by isobaric simulations at 1 atm at 340K for 2ns, 360K for 500ps, 380K for 500ps and 400K for 10ns to reach its stabilized state. Each sample is prepared independently and this initial thermalization will allow the perfect crystals in the simulation box do thermal expansion at each target temperature since all the subsequent simulations are performed with the length of y direction fixed. The simulations use Nosé-Hoover barostat and thermostat [168] as implemented in LAMMPS [136] with relaxation timescales of 0.1 ps for thermostat during isothermal-isochoric MD and 1 ps for barostat and 0.1 ps for the thermostat during isothermal-isobaric MD. [166]

To create the coexistence of a crystal nucleus with an equilibrated liquid, we fixed the central region (2×2 nm^2 in cross-sectional area on the x-z plane) and melted the rest of the system at 800 K using isothermal, isobaric MD with fixed simulation length along the y direction for 500

ps. Periodic boundary conditions are imposed on all three directions. The resulting cells were further replicated 3 times along x and 3 times along z direction, resulting in a model with 630 PE chains. The resulting cells (one per temperature) where further relaxed at 800 K (always keeping the atoms in the crystalline seed fixed) and deformed to a square shape in the xz plane over 500 ps. All systems were further relaxed at 800 K using isothermal-isochoric MD for 50 ps and isothermal-isobaric MD with fixed simulation box at y direction for 500 ps always with central region fixed. After generating the initial crystal-melt coexistence structure at 800 K, we cooled the liquid systems from 800 K to 500 K for 5 ns using isothermal-isobaric MD with fixed simulation box at y direction and then annealed to the desired crystallization targeted temperatures for an additional 50 ps using isothermal-isochoric MD. All initial structure data files are available at https://github.rcac.purdue.edu/StrachanGroup. [166]

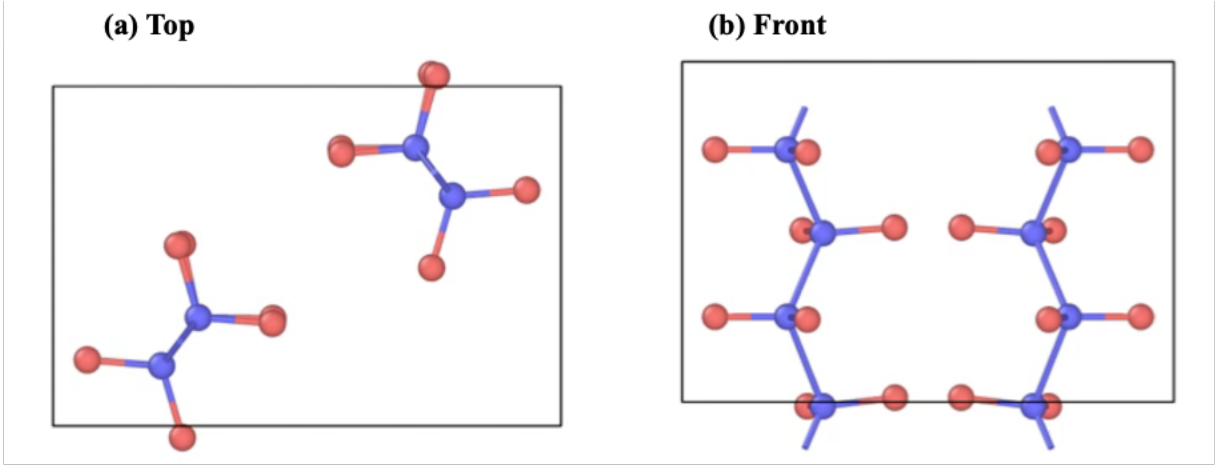

Figure 4.1. (a) Top and (b) front view of unit cell of crystalline PE

Table 4.1. Unit cell of PE [167]

Crystal class	*a*, *b*, *c* (Å)	α, β, γ (°)
Orthorhombic	7.42, 4.95, 5.10	90, 90, 90

4.2.2 Crystallization simulation

The initial state of the simulations consists of a crystallite surrounded by an undercooled liquid within a simulation cell with periodic boundary conditions and cross-sectional dimensions

of 28 × 32 nm^2 for 340 and 400 K and 38 × 24 nm^2 for 360 and 380 K, see Figure 4.2, and a thickness of approximately 3.5 nm. The sample thickness (normal to crystallization plane) corresponds to 7 times the PE crystal lattice parameter along the [010] direction. Each cell contains 630 PE chains of C_{160}, for a total of 303,660 atoms. Our selection of C_{160} for this study is motivated only in part by the fact that preparing samples with higher molecular weight is computationally more challenging. More importantly, since folding and entanglement are the basic characteristics of crystallization from the melt, the C_{160} we choose is about twice the typical PE entanglement length C_{60} ~ C_{90} [169,170], and ensures that the entanglement is captured in the crystallization dynamics. Moreover, C_{160} is long enough to show chain-folded crystals, and the typical lamella thickness is about C_{65} [171].

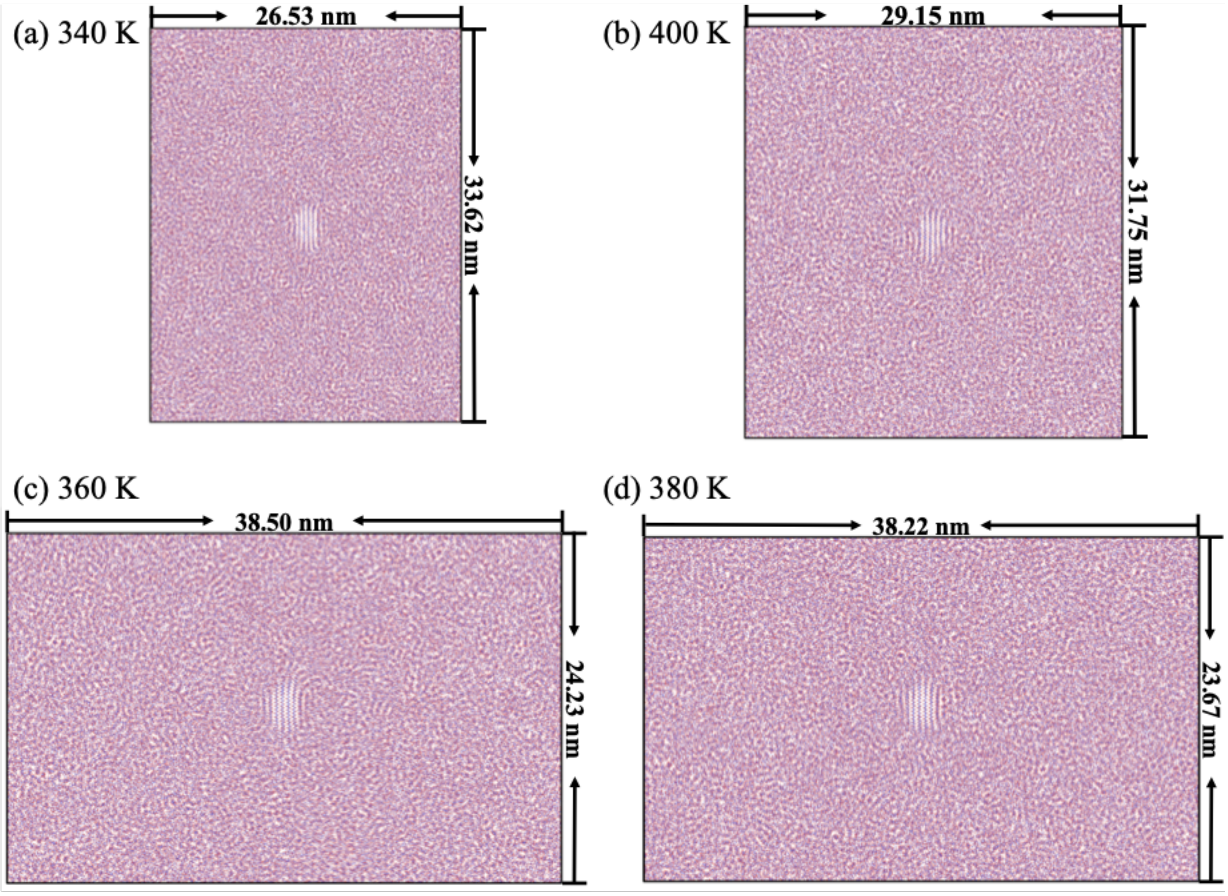

Figure 4.2. Start model with nuclei embryo (width: 2nm, height: 2nm) for (a) 340K, (b) 400K, (c) 360K and (d) 380K.

After thermalization, we model crystallization under isothermal, isobaric conditions. The cell dimensions along x and z (the plane of crystal growth) evolve independently to maintain 1 atm. The out of plane cell dimension (the smallest dimension, y) is kept fixed in order to model cylindrical crystallites growing on the x-z plane. Cell angles are maintained at 90° due to the liquid nature of the matrix. These boundary conditions do not interfere with the growth of the initial grain on the x-z plane nor with the nucleation of induced grains. We describe atomic interactions using the DREIDING [89] force field with atomic charges obtained using iterative partial equalization of orbital electronegativity developed by Gasteiger [172]. This general-purpose force field can provide semi-quantitative predictions of a wide range of polymers and thermo-mechanical properties [90–92].

4.2.3 Discussion: molecular weight dependence of crystallization kinetics and crystal morphology

The selected molecular weight (C_{160} with molecular weight of 2.2×10^3) is relatively small compared most high molecular weight samples used in experimental studies. The mechanisms of NCB are not affected by this choice. For the sake of completeness, we discuss the influence of molecular weight on crystallization kinetics and the resulting crystal morphology in order to fully evaluate our results on NCB. [166]

Crystallization nucleation rate. Experiments and MD studies have shown that homogeneous crystal nucleation is a local event, and the nucleation rate is independent of molecular weight [100,173]. For PE, Cormia et al. found that the nucleation factor,

$$I_0 = A \exp(-E_d/k_B T) \tag{4.23}$$

where E_d is the activation energy characterizing diffusion that transport chain segments to or from the nucleus, was not significantly different between PE with Mw 1.8×10^5 and n-alkane ($C_{16}H_{34}$, $C_{17}H_{36}$, $C_{18}H_{38}$, $C_{24}H_{50}$, and $C_{32}H_{66}$) [100,174,175].

Crystallization growth rate. The growth process of polymer crystallization usually involves heterogeneous nucleation and the rate decreases with molecular weight; this is attributed to the diffusivity D. Ref. [176] shows the power law relationship between the growth rate and molecular weight for heterogeneous nucleation

$$V \propto D \propto M_n^{-H} \tag{4.24}$$

where the power H = 1.7 for PE folded chain single crystals formed in the ordered phase. [166]

Crystal morphology. Finally, some flow-induced crystallization studies have observed an increase in orientation with increasing polymer molecular weight, and found that if long chains are present, polymer crystallization is more sensitive to shear flow. The long chain can maintain the anisotropic state for a long time due to its slow relaxation kinetics, while the shorter chain will relax quickly after stopping shearing. However, due to the higher entanglement density, the higher molecular weight is expected to have a shorter local order, while for lower molecular weights, the local ordering is longer due to the lower entanglement density. [177,178]

In summary, increasing the chain molecular weight in the polymers would result in slower growth but also the induced orientation would persist for longer times. These opposing effects indicate that the effect of temperature on NCB in polymer crystallization and crystal morphology transition captured in our simulation will apply to higher molecular weight polymers. [166]

4.2.4 Simulation analysis

Monomer orientation characterization. The orientation of each monomer is defined as the unit vector of separating second nearest carbon atoms along the polymer backbone. Except atoms at chain ends, we consider each C atom in the backbone has its own local orientation as

$$\mathbf{k}_n = \frac{\mathbf{r}_{n+1} - \mathbf{r}_{n-1}}{|\mathbf{r}_{n+1} - \mathbf{r}_{n-1}|} \quad \left(k_{n_z} \geq 0\right) \tag{4.25}$$

where $\mathbf{r}_n$ represents the position of the backbone C atom n. [166]

Chain alignment characterization. Chain alignment is a measure of monomer orientation with respect to its neighboring monomers. Despite head and tail atom of each PE chain, we define local alignment as

$$a_n = \frac{1}{m} \sum_{m}^{|\mathbf{r}_m - \mathbf{r}_n| < r_{cutoff},\, m \neq n} \arccos(\mathbf{k}_m \cdot \mathbf{k}_n) \tag{4.26}$$

where r_{cutoff} = 5 Å. It averages deviation angle of monomer direction of each backbone C atom with it surrounding neighbors with cutoff of 5 Å. Figure 4.3A shows the local alignment map for 360 K after 150 ns MD simulation. We found that our structures is very similar to the AFM images of the early stage of polymer crystallization [87]. Figure 4.3 compares our prediction (A) with two AFM images of the initial stages of crystallization in the BA-C8 copolymer (B). [166]

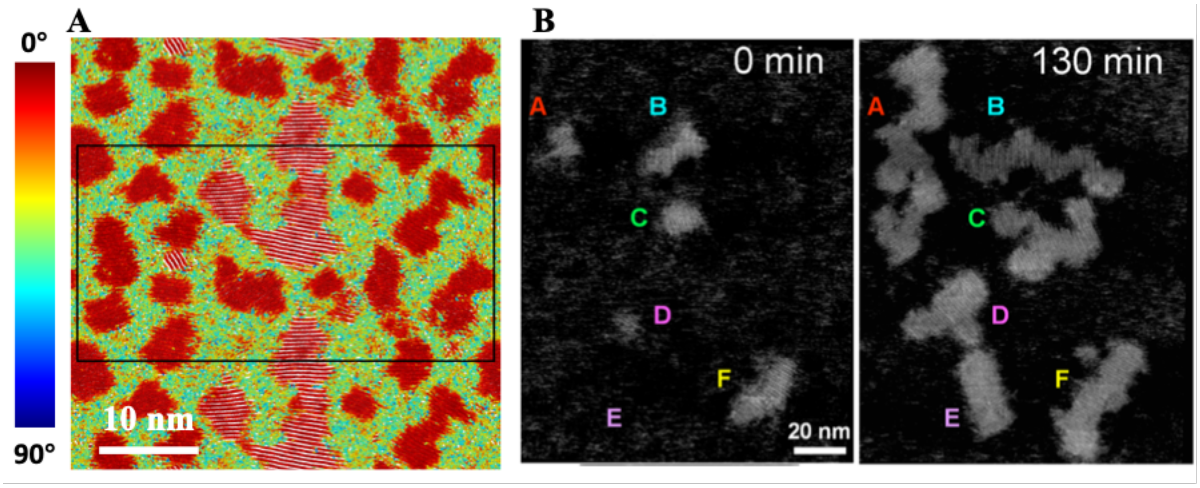

Figure 4.3. Comparison of our prediction (A) local alignment map for 360 K after 150 ns MD simulation with (B) two AFM images of the initial stages of crystallization in the BA-C8 copolymer adapted from Ref. [87].

Then we average the local monomer alignment of the whole system,

$$\bar{A} = \frac{1}{N * n} \sum_{N} \sum_{n} a_{C_{N,n}} \tag{4.27}$$

To quantify global chain alignment with respect to the primary crystallite we computed the average angle between the orientation of each monomer and that of the primary nucleus

$$\overline{K_{mon}} = \frac{1}{N * n} \sum_{N} \sum_{n} \mathbf{k}_{C_{N,n}} \cdot \hat{z} \tag{4.28}$$

where N, n represent the chain number and the monomer number of each chain respectively. [166]

Molecular orientation characterization. In order to obtain the molecular orientation, we first calculated the radius of gyration for each chain as the following

$$R_g^2 = \frac{1}{M}\sum_i m_i(\mathbf{r_i} - \mathbf{r_{cm}})^2 \begin{cases} R_{g_{xx}}^2 = \frac{1}{M}\sum_i^n m_i(x_i - x_{cm})^2 \\ R_{g_{yy}}^2 = \frac{1}{M}\sum_i m_i(y_i - y_{cm})^2 \\ R_{g_{zz}}^2 = \frac{1}{M}\sum_i m_i(z_i - z_{cm})^2 \end{cases} \tag{4.29}$$

where M represents the molecular weight of each PE chain, m_i, x_i, y_i and z_i represent the molecular weight, position along x, y and z for atom i, x_{cm}, y_{cm} and z_{cm} represent the position of center of mass along x, y and z direction. Results for 340 K and 360 K are shown in Figure 4.4 where results for mass reduced moment of inertia calculated as the following

$$\begin{cases} I_{r_{xx}} = \frac{1}{M}\sum_i m_i\left((y_i - y_{cm})^2 + (z_i - z_{cm})^2\right) \\ I_{r_{yy}} = \frac{1}{M}\sum_i m_i((x_i - x_{cm})^2 + (z_i - z_{cm})^2) \\ I_{r_{zz}} = \frac{1}{M}\sum_i m_i\left((x_i - x_{cm})^2 + (y_i - y_{cm})^2\right) \end{cases} \tag{4.30}$$

also present. We define average molecular orientation as the following

$$\overline{K_{mol}} = \left(\frac{1}{N}\sum_N R_{g_{N,zz}}\right)/\left(\frac{1}{N}\sum_N R_{g_{N,xx}}\right) \tag{4.31}$$

Crystallites identification. To characterize crystal nucleation, we first identify monomers belonging to crystalline regions based on the degree of local chain alignment and then group these monomers into crystallites by performing a cluster analysis using minimum spanning tree method. Detailed steps are as the following:

1. Disqualify 2 central C atoms if -120° < torsion angle < 120°, see Figure 4.5
2. Create clusters of crystalline C atoms $\mathbf{k}_m$, $\mathbf{k}_n$ that satisfy
    a. $|\mathbf{r}_m - \mathbf{r}_n| < r_c$ where $r_c = 5$ Å (Figure 4.6)
    b. $\arccos(\mathbf{k}_m \cdot \mathbf{k}_n) < \theta_c$ where $\theta_c = 5°$ (Figure 4.7)
3. Define all connected C atoms as an individual cluster and all other C atoms (including chain ends) as amorphous region
4. Classify clusters based on their number of C atoms N_c
    a. If $N_c \geq 50$, define as crystalline cluster (Figure 4.8);
    b. If $N_c < 50$, define as amorphous region;

We modified r_c and θ_c for analysis of our systems with $r_c = 4$ Å, 5 Å, 6 Å, 7 Å, 8 Å and $\theta_c = 5°$, 10°, 15°. Comparison for induced crystallinity is shown in Figure 4.9. [166]

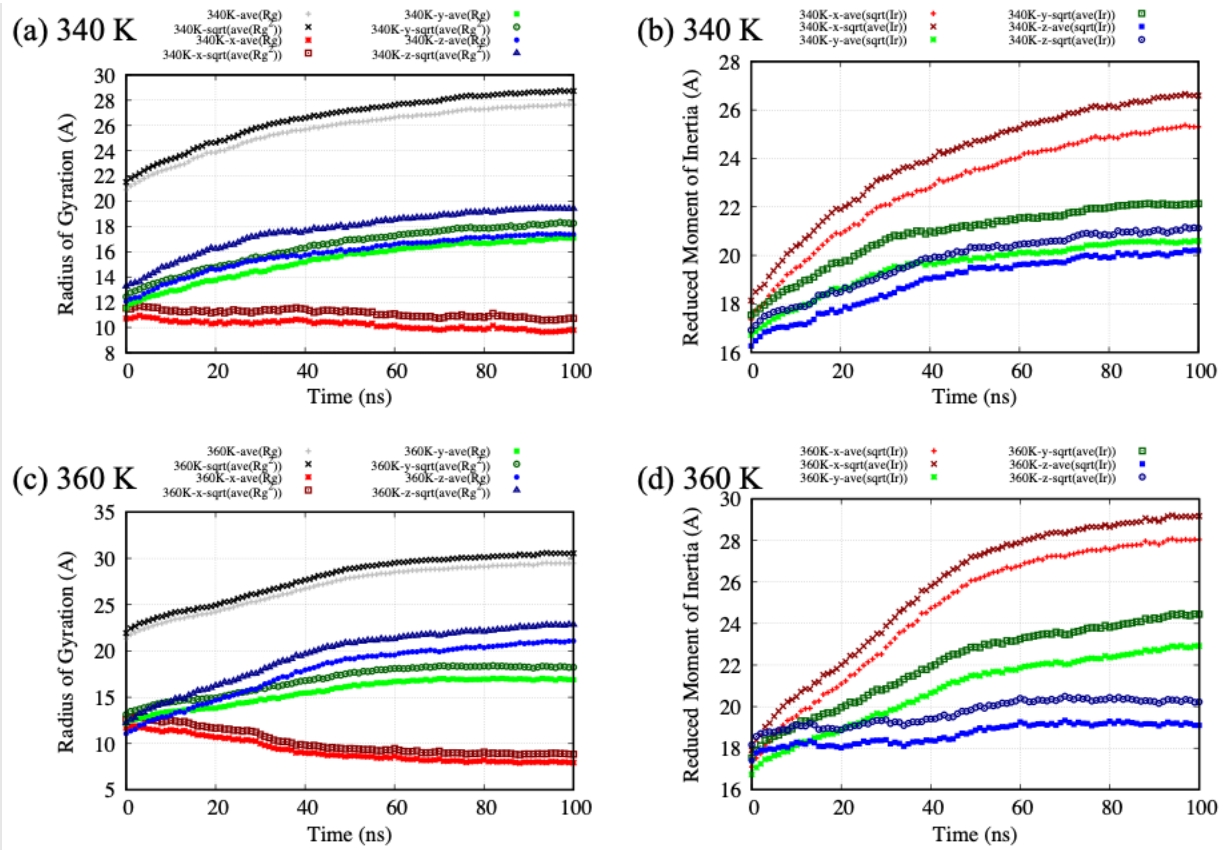

Figure 4.4. Radius of gyration and mass reduced moment of inertia for (a) (b) 340 K and (c) (d) 360K.

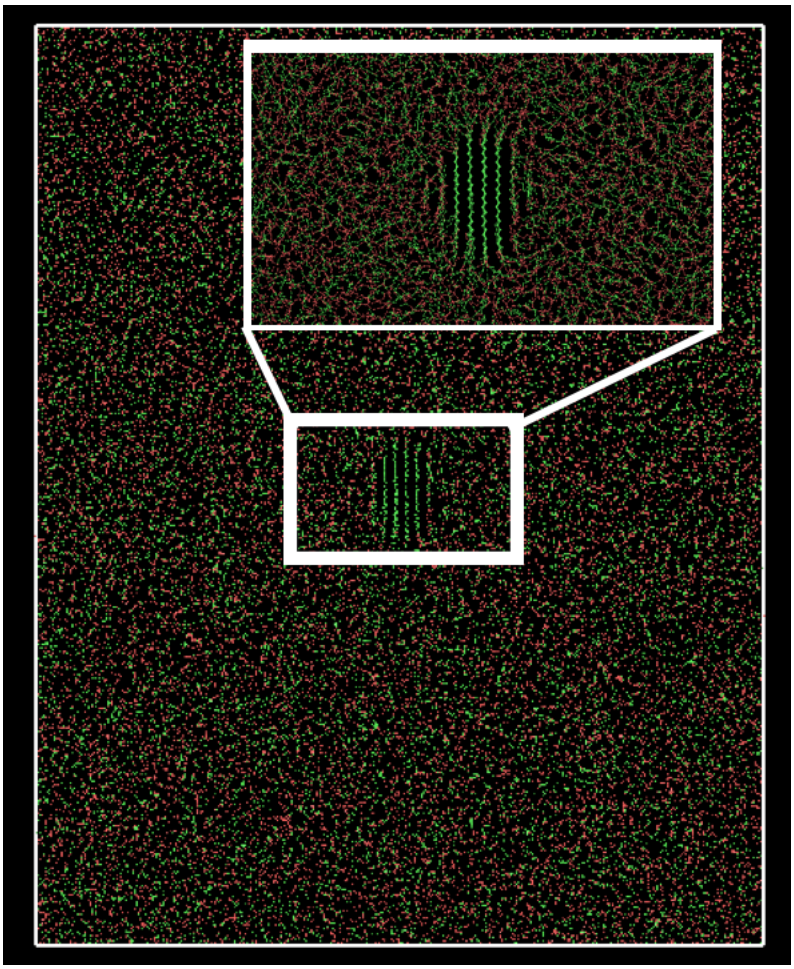

Figure 4.5. Atom snapshot of atoms after torsion selection [green atoms --- torsion < -120° or torsion > 120°, red atoms --- -120° < torsion angle < 120°]

Based on the comparison, we found that when r_c lower than 5 Å with $\theta_c = 5°$, the total number of connected atoms are significantly dropped resulting in fault analysis with very low crystallinity and when r_c larger than 5 Å with $\theta_c = 10°$ or 15°, as system crystallize with increasing connections between C atoms, more and more clusters are connected with the primary nucleus and resulting in dropping number of the C atoms in induced nucleus. Other results are not sensitive to the choice of cutoffs in space or angle. Since $r_c = 5$ Å and $\theta_c = 5°$ would give all zero induced percentage for 400 K. Therefore, all the results we chose $r_c = 5$ Å and $\theta_c = 5°$ as analysis cutoffs. [166]

Lamellae thickness calculation. Except at 400 K, where only one crystallite is identified, we selected 10 largest crystallites and calculated all the length of the chain segments inside the

crystal cluster. Then we define the lamellae thickness as the average length of 10 longest chain segment inside the crystallite. Table 4.2 illustrated the cluster size and lamellae thickness for all the clusters used in this calculation. [166]

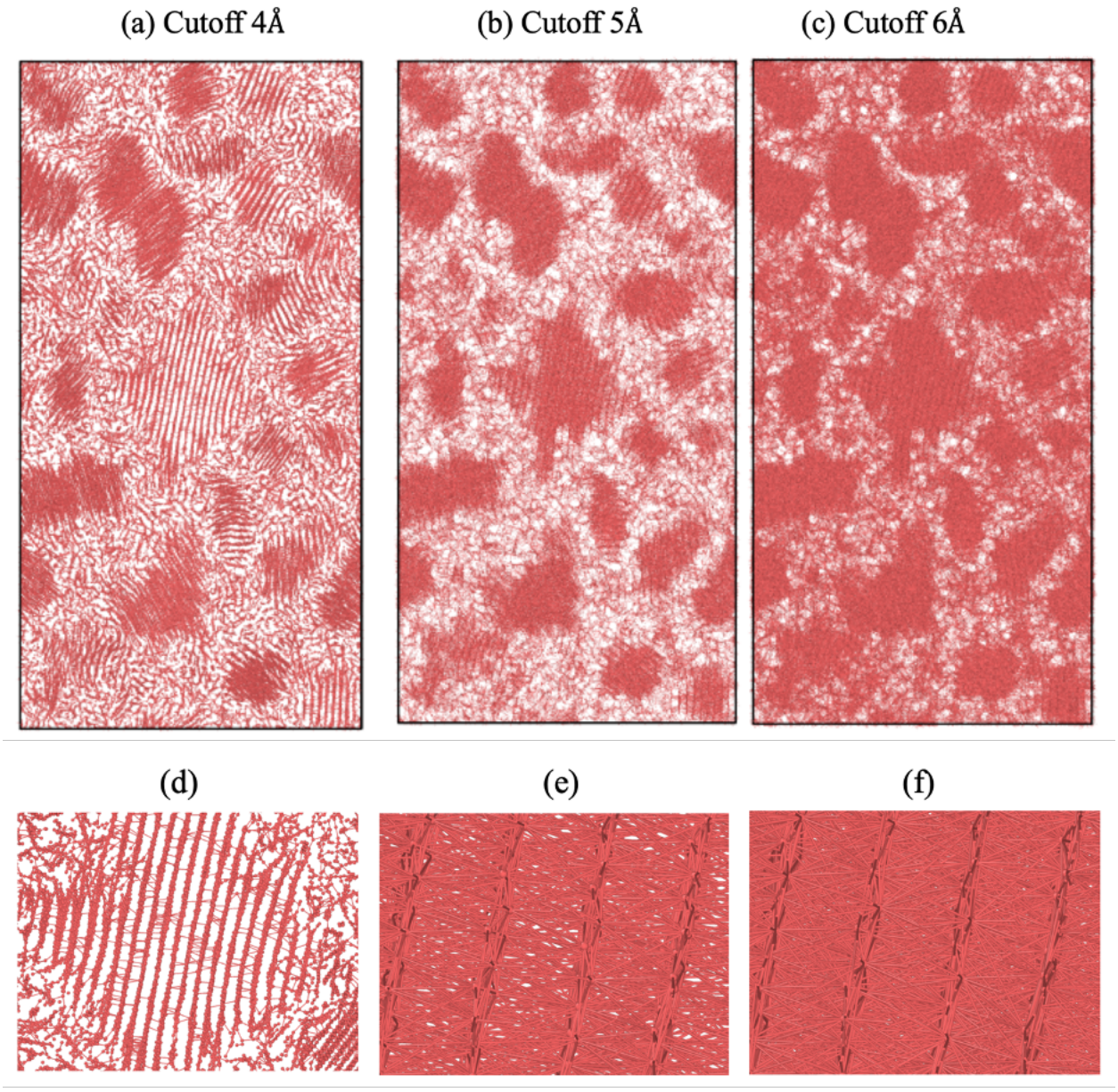

Figure 4.6. Atom snapshot of atoms after cutoff distance selection of (a) 4 Å, (b) 5 Å and (c) 6 Å. (d), (e) and (f) are zoomed snapshot at the center of (a), (b) and (c), respectively.

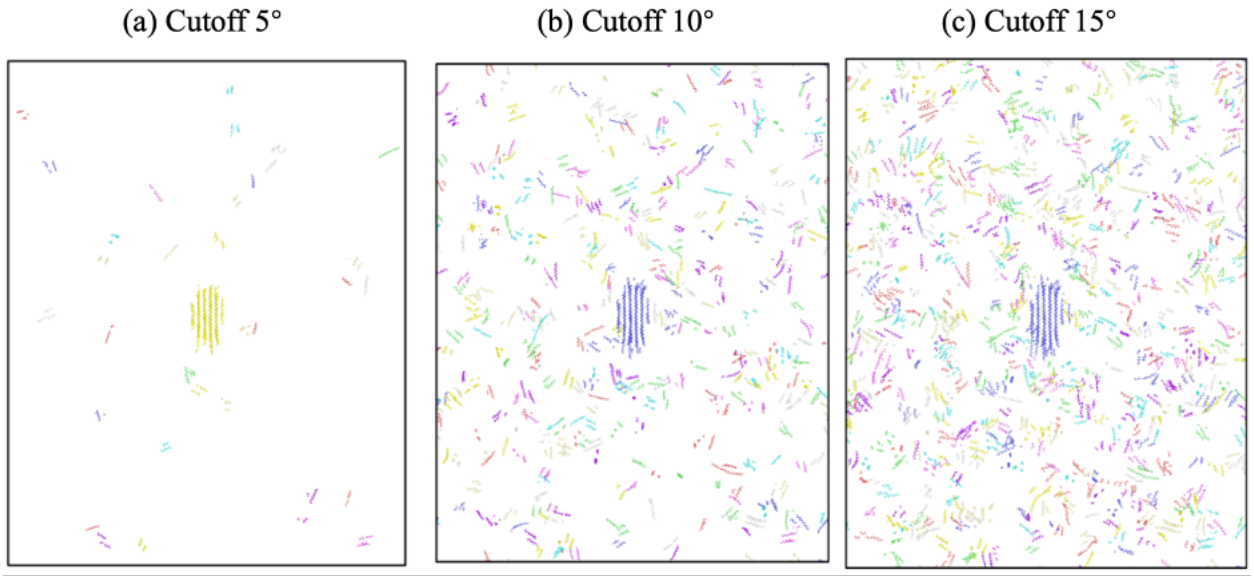

Figure 4.7. Atom snapshot of atoms after cutoff angle selection.

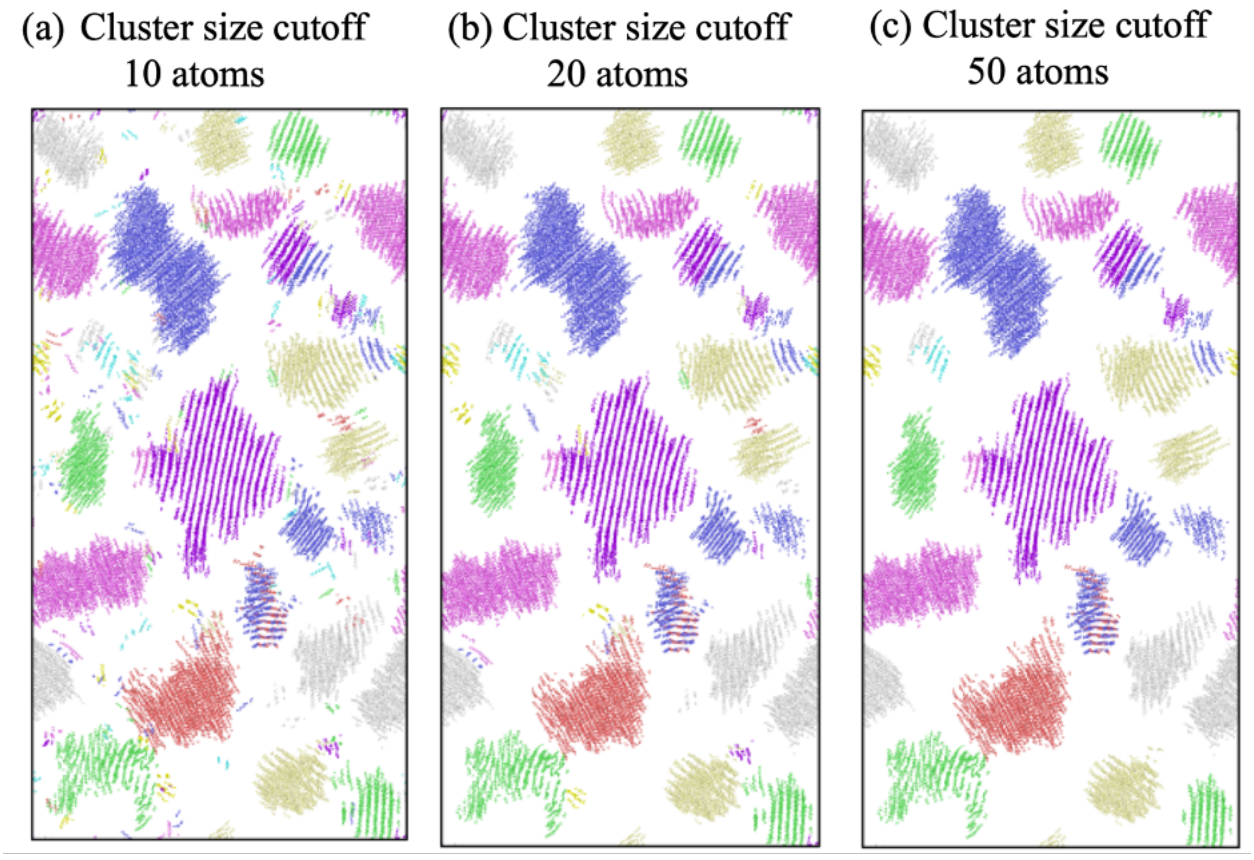

Figure 4.8. Atom snapshot of atoms after cluster size cutoff selection.

The lamella thickness predicted in the simulations is about 18 nm for 340 ~ 380 K and 21 nm slightly higher for 400 K. The simulation results are in good agreement with the experimental

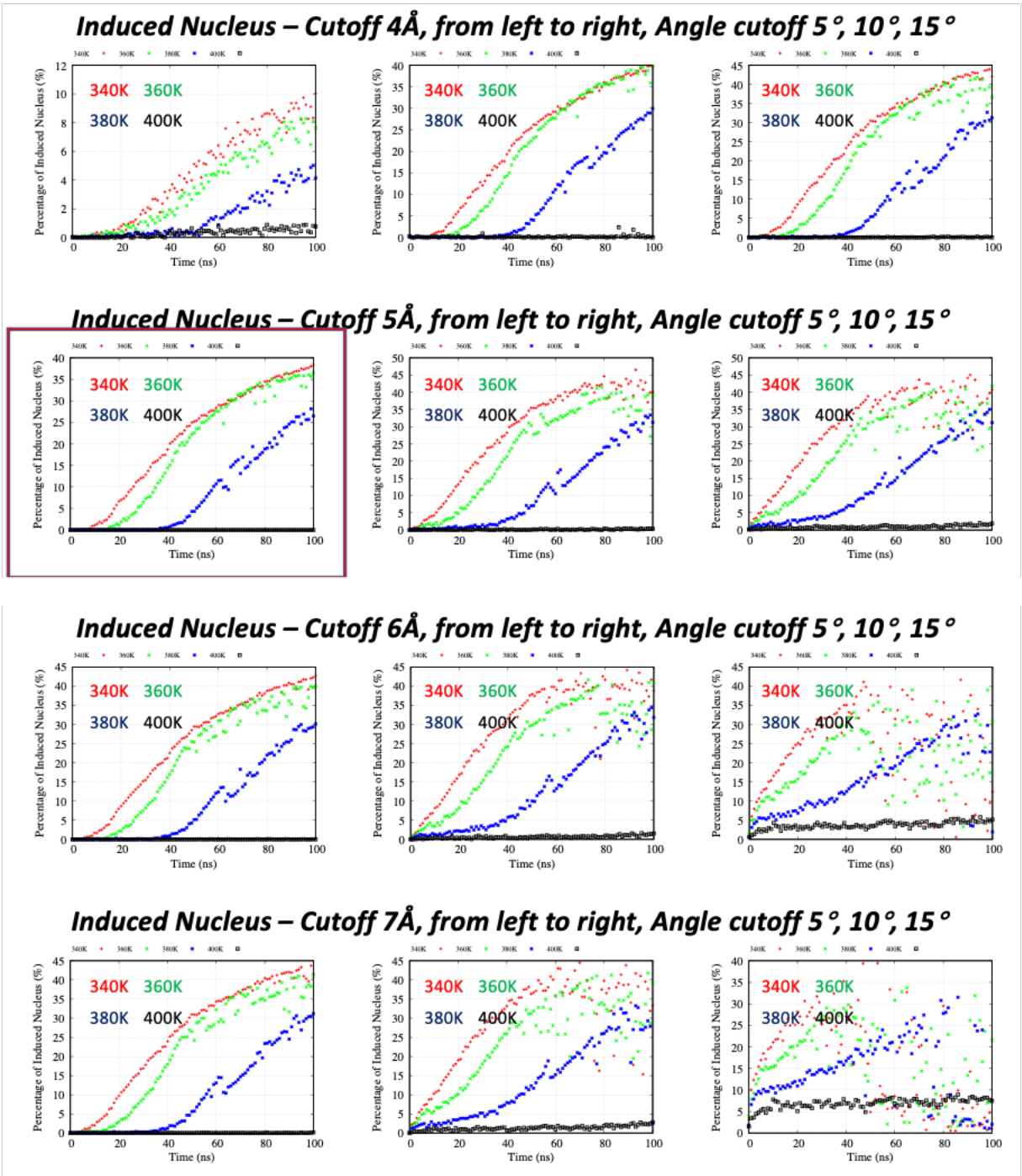

Figure 4.9. Comparison for induced crystallinity with various r_c and θ_c. Figure illustration with selected r_c = 5 Å and θ_c = 5° is highlighted in the red rectangle.

Figure 4.9. continued

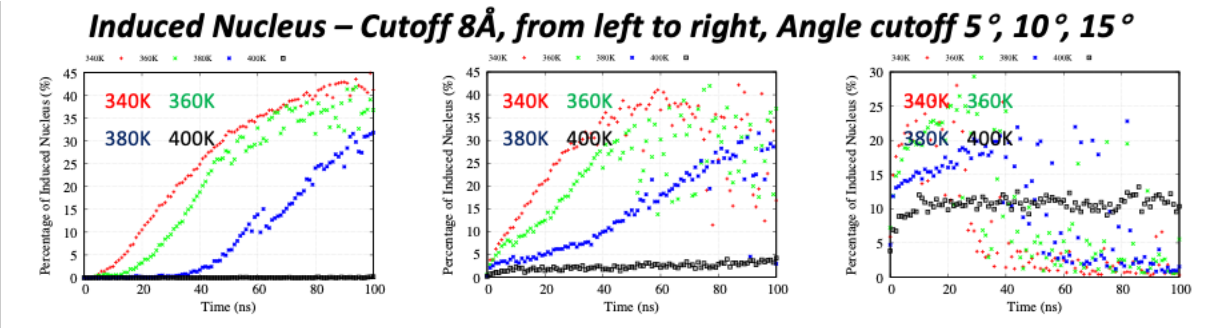

results [42].

Cluster orientation characterization. We define crystallite orientation as

$$\mathbf{K}_i = \frac{\sum_n \mathbf{k}_{i,n}}{\left|\sum_n \mathbf{k}_{i,n}\right|} \tag{4.32}$$

where $\mathbf{k}_{i,n}$ represents each backbone C atom n within the cluster i. Detailed $\mathbf{K}_i$ for all the nucleus are shown in Figure 4.10. [166]

To quantify the alignment of the chains in the liquid with those in the primary lamella we computed the average angle between the backbone direction of each monomer in the liquid and those in the primary nucleus. After obtaining the orientation of the primary nucleus, we calculated average local alignment in the liquid as

$$\Theta_L = \frac{\sum_n \arccos(\mathbf{k}_n \cdot \mathbf{K}_p)}{N_t - N_p} \tag{4.33}$$

where n represents all C atom excluding those in primary nucleus and chain ends, $\mathbf{K}_p$ represents cluster orientation of the primary nucleus, N_t, N_p represent number of C atom of the whole system (exclude chain ends) and primary nucleus, respectively. [166]

In order to obtain the orientation of induced nucleus evolution during the time, we define the induced nuclei orientation deviation as

Table 4.2. Lamellae thickness of 10 largest crystallites at each crystallization temperature

Crystallization Temperature (K)	Index	Cluster Size[a]	Lamella Thickness (nm)	Average Thickness (nm)[b]
340	0	8067	19.74	**18.37**
	1	6173	28.90	
	2	5347	14.88	
	3	4012	19.84	
	4	3723	14.59	
	5	3647	15.74	
	6	2321	12.71	
	7	1876	13.91	
	8	1628	11.35	
	9	1435	13.79	
360	0	7254	22.45	**17.61**
	1	5679	18.27	
	2	5256	16.35	
	3	4493	16.50	
	4	3804	17.97	
	5	3793	16.16	
	6	3640	14.60	
	7	3282	17.41	
	8	3209	18.20	
	9	2724	12.68	
380	0	11576	17.96	**17.79**
	1	7835	18.89	
	2	6757	20.49	
	3	6601	21.83	
	4	3777	12.86	
	5	3560	17.27	
	6	2444	12.60	
	7	2141	15.05	
	8	1768	12.52	
	9	809	8.96	

Table 4.2. continued

400	0	13034	21.05	**21.05**

a. Number of C atoms

b. Cluster size weighted average

$$\theta_D = \frac{\sum_i N_i \ * \arccos(\mathbf{K}_i \cdot \mathbf{K}_p)}{\sum_i N_i} \tag{4.34}$$

where N_i represents the number of C atom in each induced nucleus i, $\mathbf{K}_i$ and $\mathbf{K}_p$ represent cluster orientation of each induced nucleus and primary nucleus respectively. We note that the above calculations only considered vectors in x-z direction while the chain orientation in some of the induced crystallites is not normal to the y direction, i.e. their chains are not contained in the x-z plane but tilted, see last column of Figure 4.10 where we show corresponding $\mathbf{K}_i$ in y-z direction. [166]

Deviatoric strain calculation. We describe "non-volumetric" deformations since the volume of the whole system remains rather constant throughout the process [the volume of the system is only 9% lower (the crystal density is 9% higher) than that of the undercooled liquid, see Figure 4.11A]. Given the simulation boundary conditions, any state of strain in our samples can be described by a 2 × 2 tensor, which can be decomposed into a volumetric and a deviatoric component:

$$\begin{bmatrix} \varepsilon_{11} & 0 \\ 0 & \varepsilon_{33} \end{bmatrix} = \varepsilon_{vol} I + \begin{bmatrix} \varepsilon_{dev} & 0 \\ 0 & -\varepsilon_{dev} \end{bmatrix} \tag{4.35}$$

The deviatoric component is pure shear strain, this can be easily seen by rotating axes by 45° along y, which yields:

$$\begin{bmatrix} 0 & -\varepsilon_{dev} \\ -\varepsilon_{dev} & 0 \end{bmatrix} \tag{4.36}$$

From Eq. (4.35) we also get

$$\varepsilon_{hyd} = \frac{\varepsilon_{11} + \varepsilon_{33}}{2} \tag{4.37}$$

$$\varepsilon_{dev} = \frac{\varepsilon_{11} - \varepsilon_{33}}{2} \tag{4.38}$$

We note that hydrostatic strain is closely related to volume change in an object, especially when the strains are small. For large deformations

$$\varepsilon_{vol} = \frac{V_F - V_o}{V_o} = \varepsilon_{11} + \varepsilon_{33} + \varepsilon_{11}\varepsilon_{33} = 2\varepsilon_{hyd} + \varepsilon_{11}\varepsilon_{33} \tag{4.39}$$

and the product $\varepsilon_{11}\varepsilon_{33}$ is not negligible. The time evolution of volumetric strain and hydrostatic strain is shown in Figure 4.11. [166]

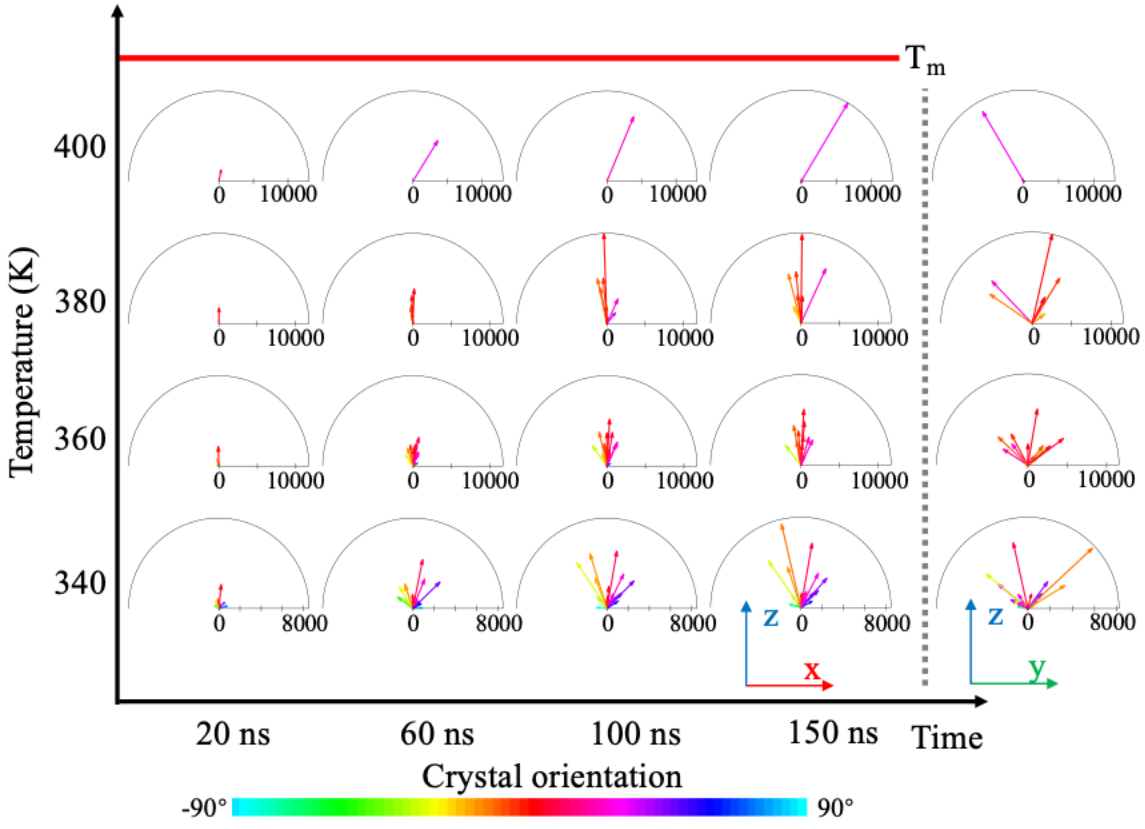

Figure 4.10. Nucleus orientation evolution during time for various temperatures. Color coding represents angle between cluster orientation and **[0,0,1]** direction. Axis for each figure embedded represents the size of the nuclei in terms of number of CH_2 included.

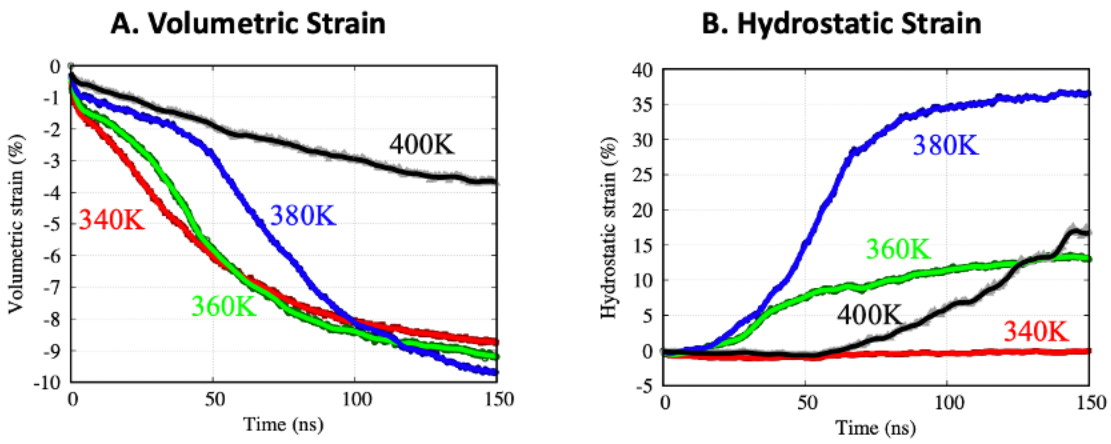

Figure 4.11. Time evolution of the (A) volumetric and (B) hydrostatic strains.

We note that measurements have shown fluid flow in crystallizing systems is associated with the volume changes that occur with crystallization. This phenomenon can be very important in the late stage of crystallization after the spherulites have impinged and this mechanism of releasing stress is suppressed, leading to the build up of huge pressures in the film that can lead to cavitation. While, the deviatoric component in our simulations is significantly larger than the volumetric one, i.e., the amounts of shear strain we observe are orders of magnitude larger than the volumetric strain associated with crystallization. Therefore, the deformation and flow we refer to is related to the need to orient polymer chains that are reeled in the crystalline lamella. [166]

4.3 Results and discussion

4.3.1 Structure evolution during crystallization

Experiments [29,47] have shown that the higher the degree of supercooling (the temperature lower than the equilibrium melting temperature T_m), the crystal morphology in the supercooled polymer develops from single crystals to spherulites. Visual inspection of the MD trajectories, see Figure 4.12, shows that the simulations capture the initial stages of the formation of fibrils and also non-trivial trends of the temperature dependence of crystallization. The resulting lamella thickness predicted varies between 10 and 30 nm in excellent agreement with experiments [42]. For relatively low undercooling, 400 K, we observe growth of the primary crystallite with no nucleation and the primary crystallite shows the same tendency to form chain

folded lamellae. Increasing the degree of undercooling results not only in the growth of primary crystallite but also in the nucleation and growth of additional lamella. Quite interestingly, for intermediate undercooling degrees (360 and 380 K) the orientation of the induced crystallites is strongly correlated with that of the primary nucleus. (Crystallites in Figure 4.12 are colored based on the orientation of their chains.) As will be shown below, the difference in orientation between the primary and induced crystallites is consistent with experimental observations for NCB responsible for the formation of spherulites. Finally, for the highest degree of undercooling studied, 340 K, a larger number of induced nuclei exhibit a broader range of angles consisting with the experimental observations of fine polycrystalline microstructures [29]. Our structures are remarkably similar to AFM images of the initial stages of polymer crystallization [87], see Figure 4.3. [166]

We note that each simulation (at different temperatures) start from vastly different liquid configurations as the thermalization prior to the crystallization simulation performed by independently quenching a sample with the crystalline seed surrounded by a liquid equilibrated at 800 K. Then each sample is thermalized for 50 ps at the appropriate temperature before starting the crystallization simulation. We believe that the fact that we observe systematic (and rather reasonable) changes both in the nucleation and growth of crystallites and in their relative orientation with varying temperature lends credence to our results and indicate that simulation cell shape does not play an important role in the observed phenomena. In Figure 4.13, you can see a clear consistent trend of temperature in independent simulations. [166]

Primary nucleus evolution during crystallization for 340 K, 360 K and 380 K are shown in Figure 4.14. We found that in the early stages of growth, the thickening process of the primary nucleus dominates, followed by the crystal growth along the lamellar direction. The thickening process greatly change the shape of the polymer chains, causing significant local deformation. Local deformation triggered induced nucleation having similar chain orientation with primary nucleation, see Figure 4.15 for selected induced nucleus evolution during crystallization at 340 K and 360 K. [166]

4.3.2 Molecular mechanisms responsible for NCB

Flow-induced crystallization. The MD simulations show surprisingly large levels of deformation during crystallization, this is apparent from evolution of the simulation cells in

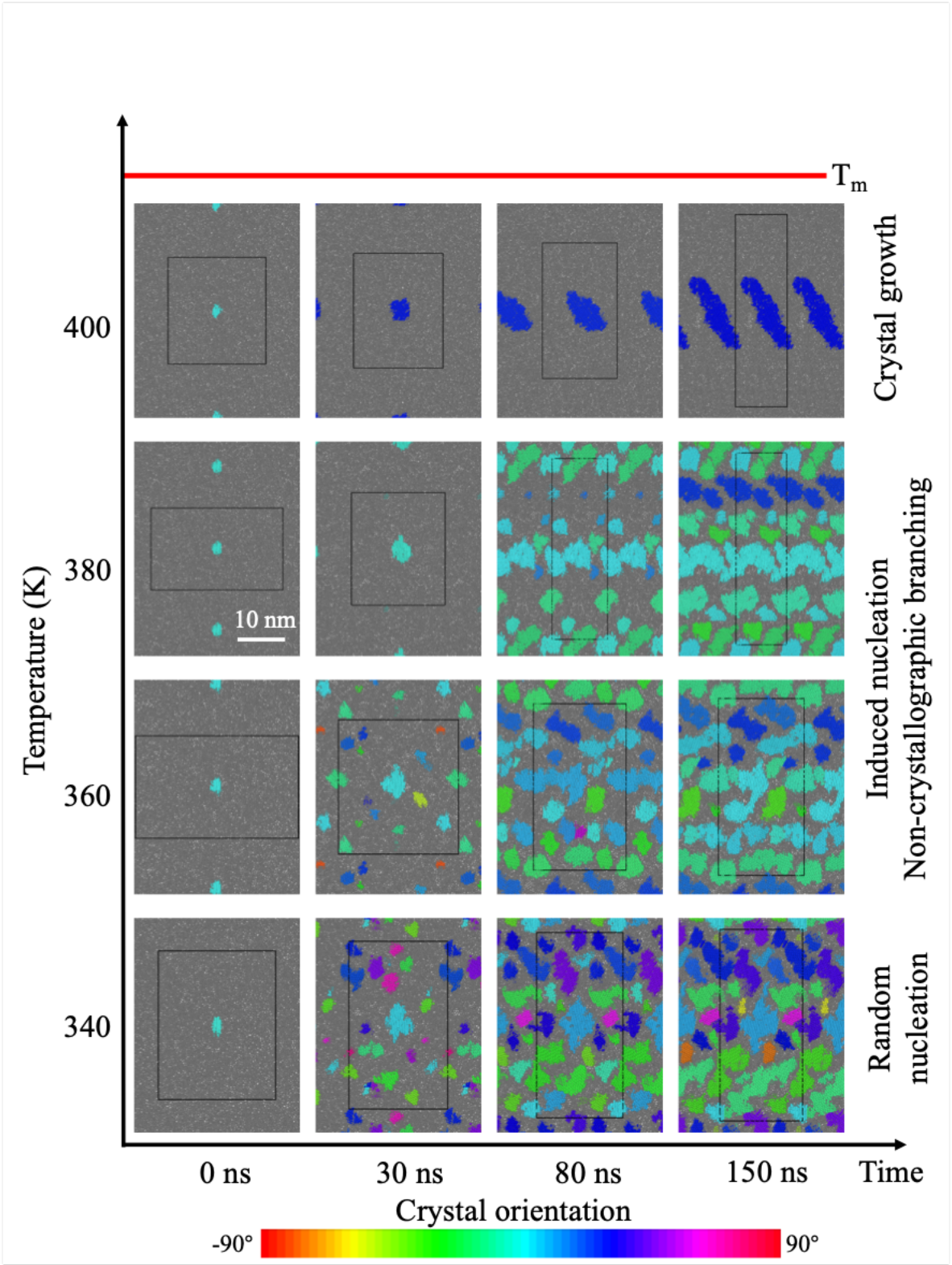

Figure 4.12. Structure evolution during crystallization. (Amorphous monomers are colored in dark grey, crystalline monomers are colored based on the colormap)

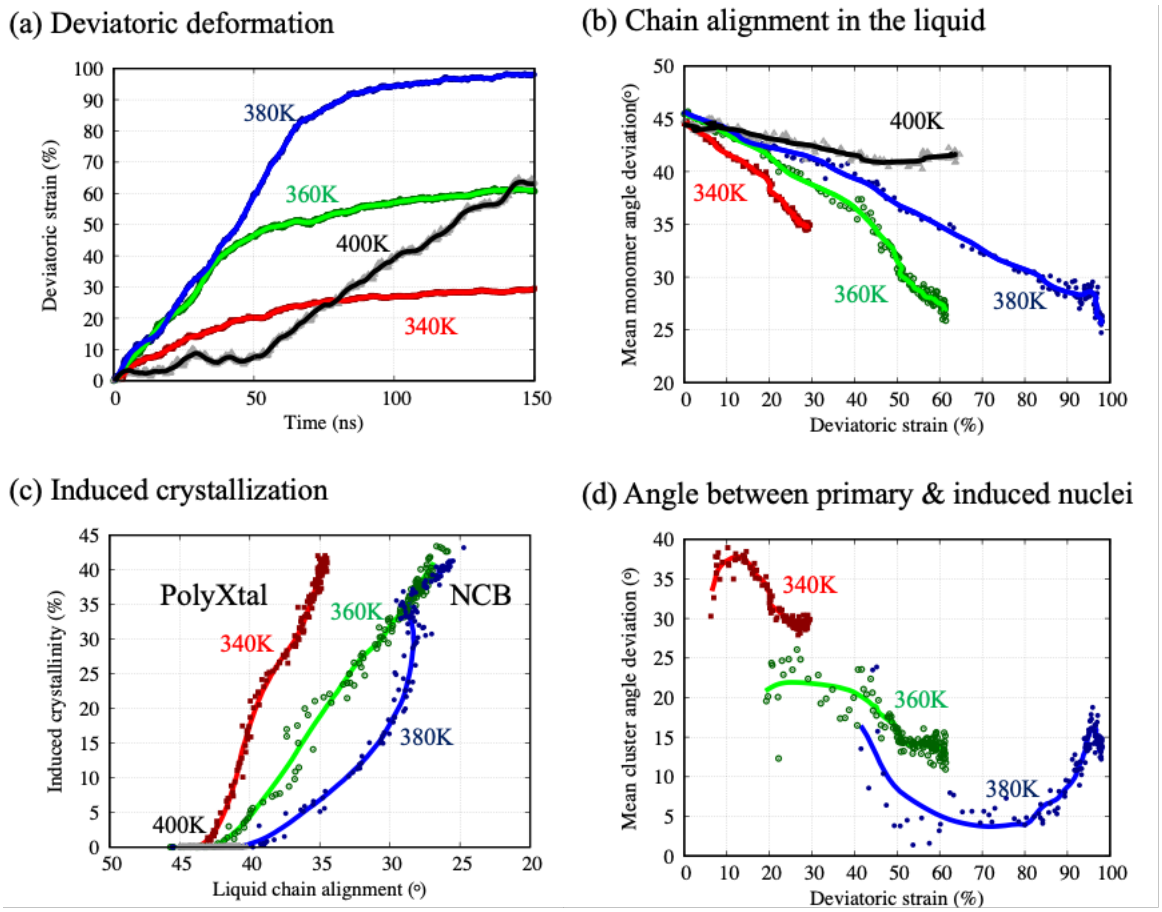

Figure 4.13. System evolution during crystallization process. (a) Time evolution of deviatoric component of the simulation cell deformation. (b) Relation between deviatoric strain and chain alignment in the liquid compared with the primary nucleus and (c) that with induced crystallinity. (d) Average angle deviation between induced nuclei and the primary nucleus. All solid curves represent the trend using polynomial fittings. Given the computational intensity of these simulations these results represent a single run per temperature. We believe they are representative due to the relatively large scale of the individual systems and the fact that we observed consistent trends as a function of temperature.

Figure 4.12. To assess the flow associated with this deformation, we computed the displacement vectors of all C atoms during the process of crystallization. Atomic flow patterns during initial induced nucleation process, see Figure 4.16, clearly show the flow of the liquid regions around the growing crystalline lamella. Vector field maps at later stages, see Figure 4.17, demonstrate that most of the chains move along the chain direction and chain movements happen more at the boundary of nucleus indicating reel-in process of the crystal growth. This observation led us to hypothesize that the local deformation in the supercooled liquid around the primary nucleus,

induced by its growth, could result in flow-induced chain alignment which, in turn, would induce crystallization with a preferred, non-crystallographic orientation. [166]

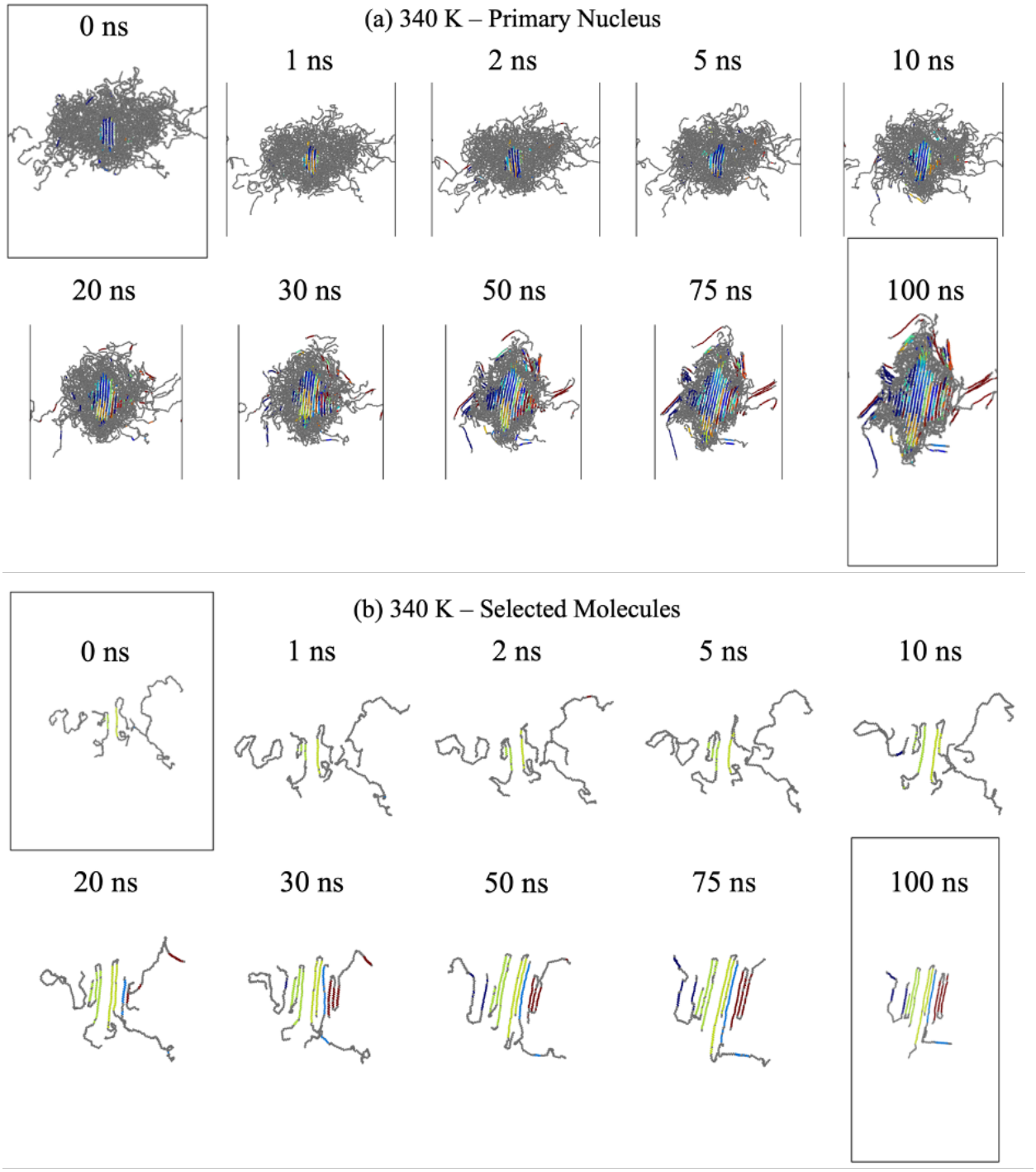

Figure 4.14. Primary nucleus evolution during crystallization. Whole nucleus and selected molecules views at (a) (b) 340 K, (c) (d) 360K and (e) (f) 380K. (Color coding represents polymer chains at crystalline region, grey represents chains at amorphous region)

Figure 4.14. continued

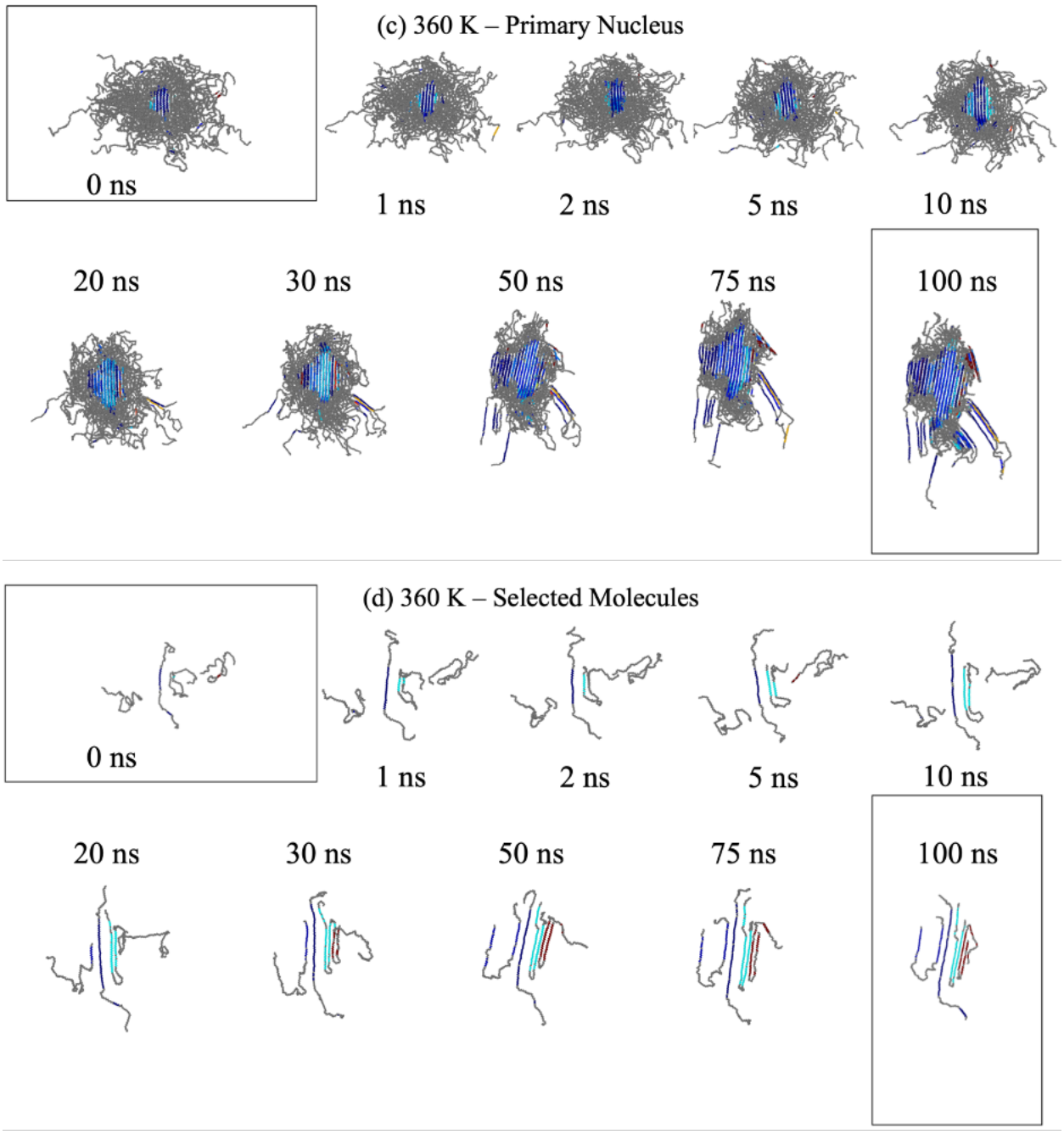

Figure 4.14. continued

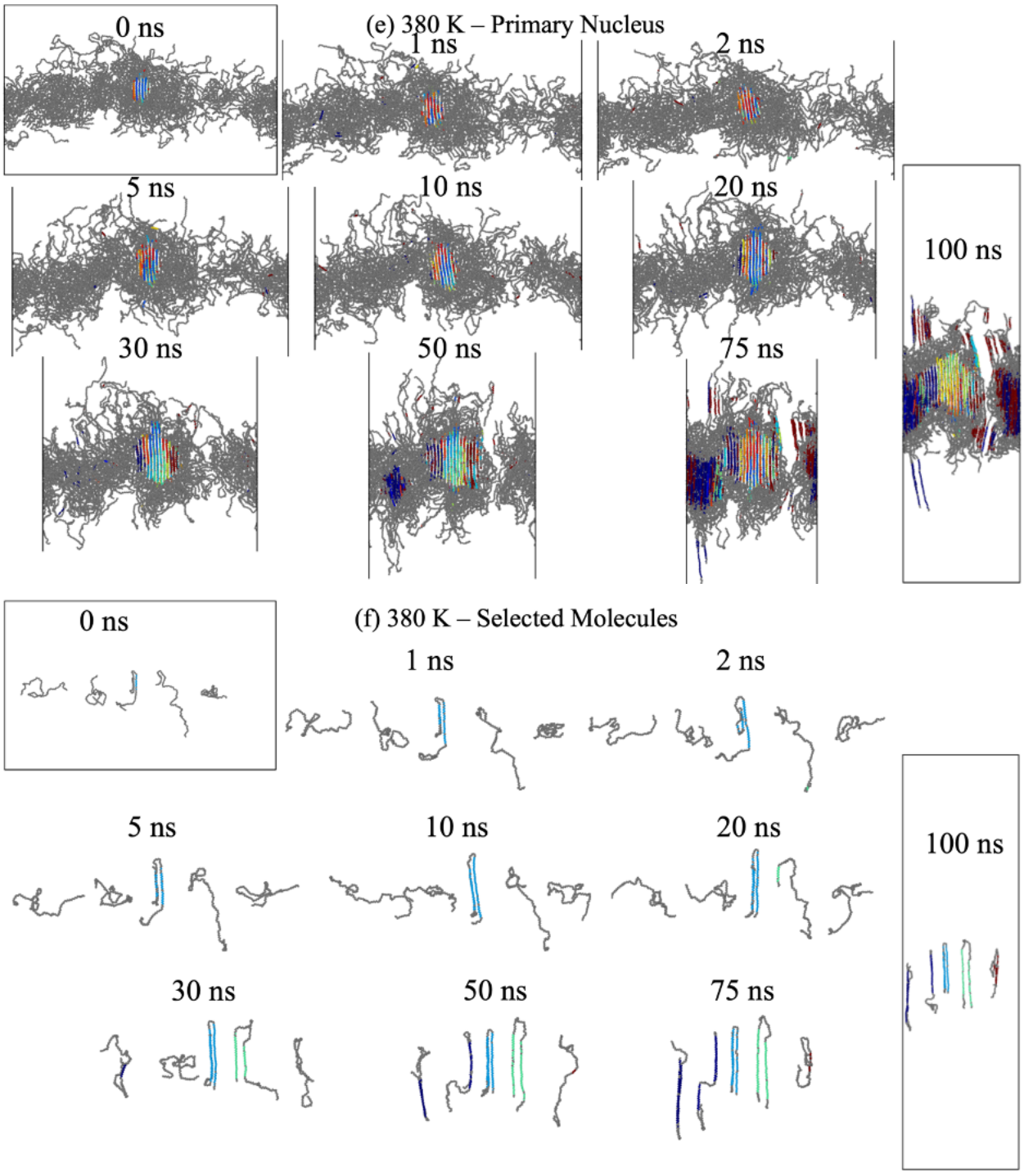

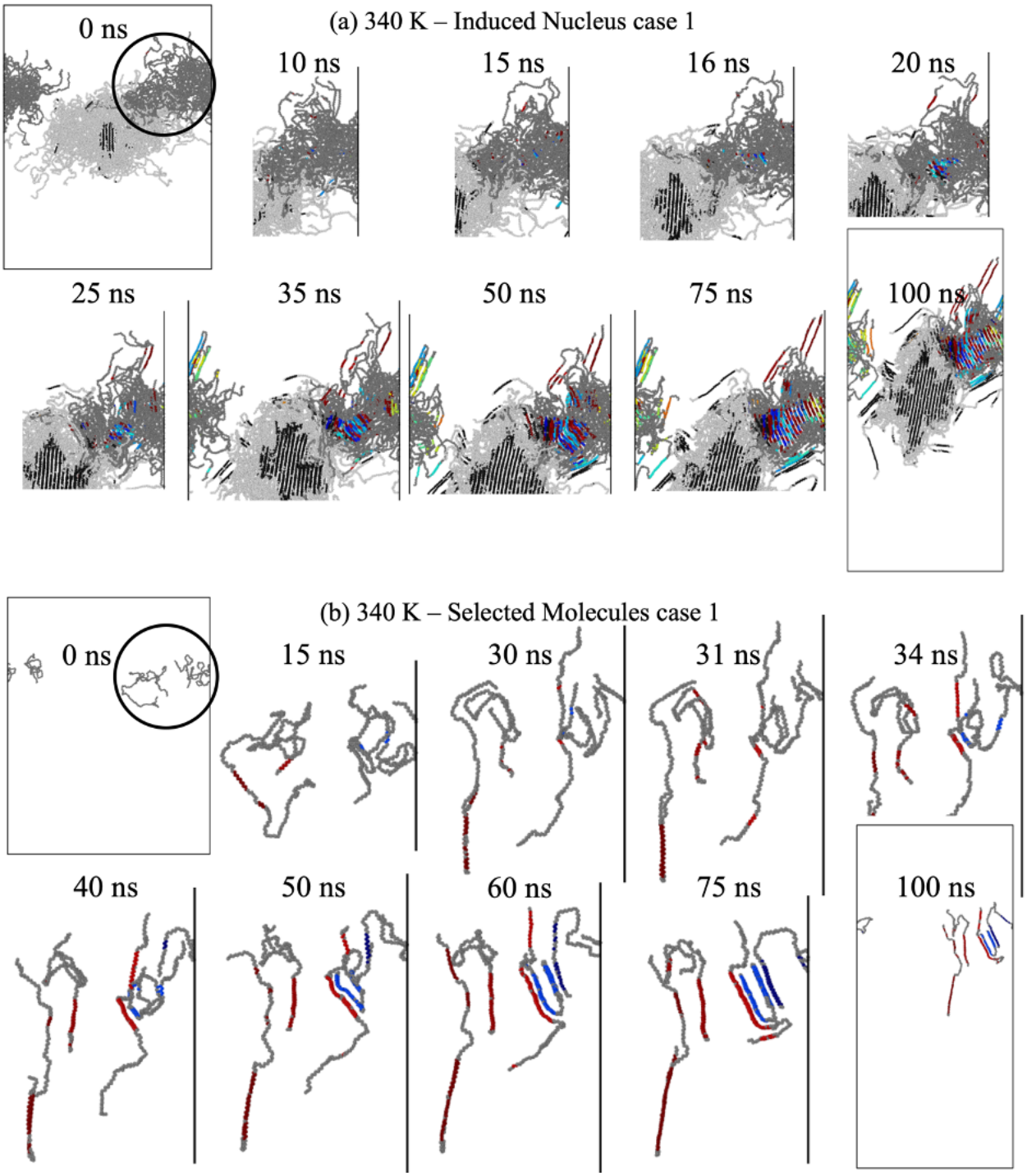

Figure 4.15. Induced nucleus evolution during crystallization. Whole nucleus and selected molecules views for (a) (b) selected induced nucleus 1 at 340 K, (c) (d) selected induced nucleus 2 at 340 K and (e) (f) selected induced nucleus 1 at 360 K. (Color coding represents polymer chains at crystalline region, grey represents chains at amorphous region and black represents primary crystal)

Figure 4.15. continued

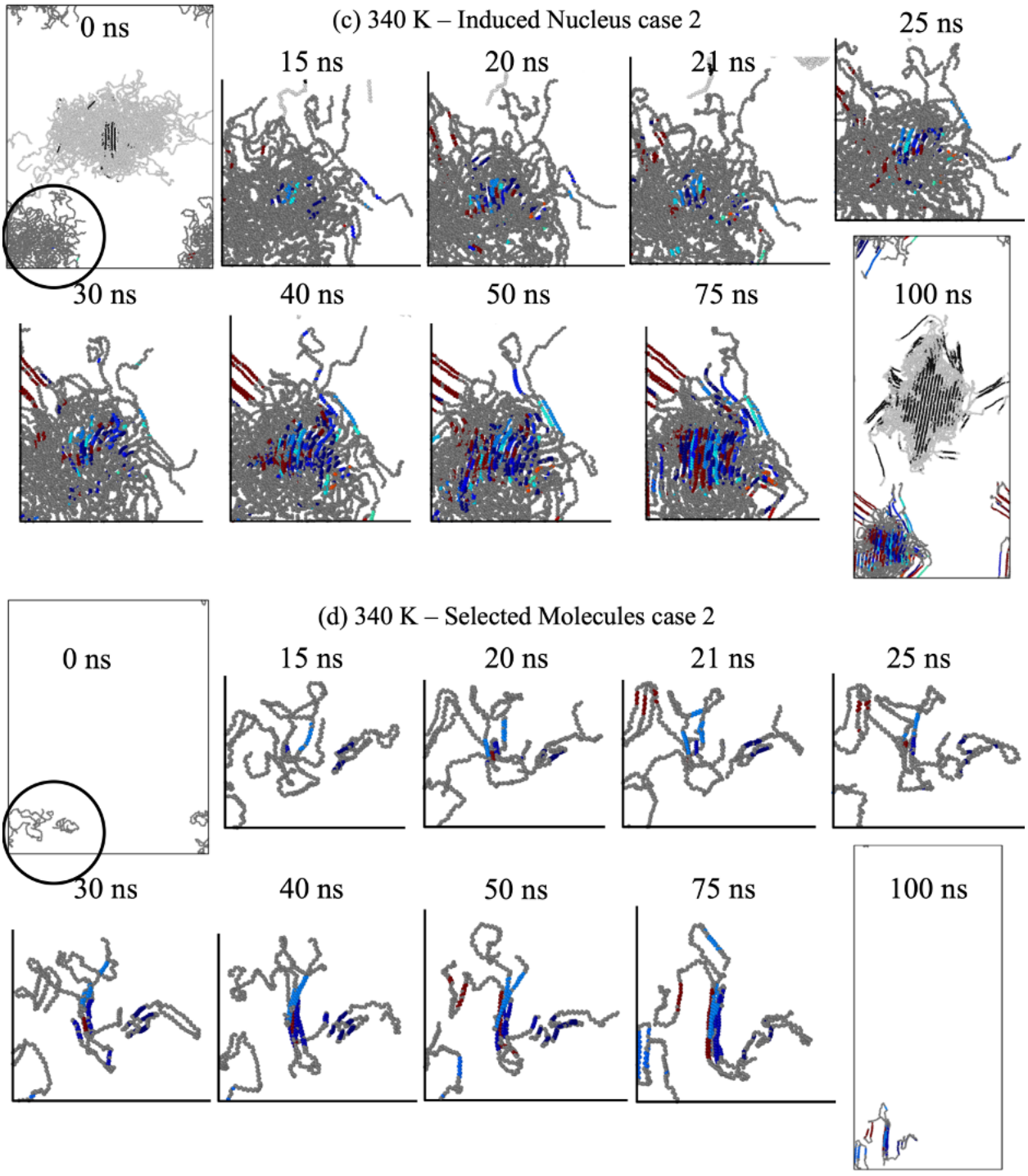

Figure 4.15. continued

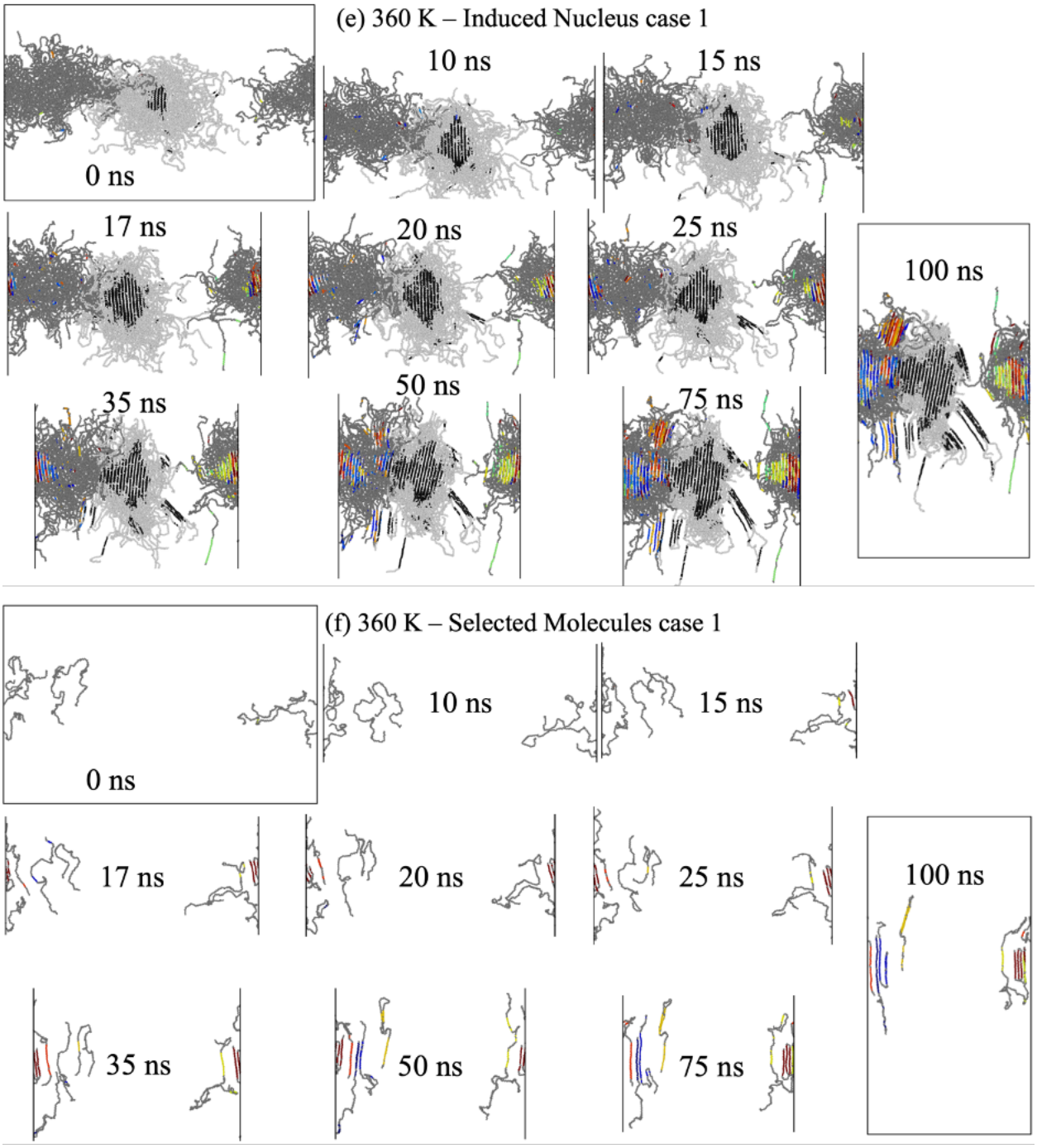

Figure 4.13(a) shows the time evolution of the deviatoric component of the total strain of the simulation cell during the crystallization process. We find significant non-volumetric deformation in timescales of tens of nanoseconds, this is particularly true for intermediate levels

of undercooling (380 K and 360 K) where we observe local strains over 60% (strain rates surpassing 10^7 s^{-1}). This extraordinary level of shear deformation originates from the growth of the primary nucleus through reeling in of chains from the amorphous region and chain folding [101]. As chains are reeled in and aligned with the primary nuclei, they induce the orientation of neighboring polymer chains [98]. A molecular-level picture of this process is presented in Figure 4.18. We find a direct relationship between chain alignment and deviatoric strain, see Figure 4.13(b). As expected, due to the increase in molecular mobility, the rate of alignment vs. strain decreases with temperature. Crystallization at a temperature close to the melting point will cause a decrease in crystallinity due to the slower growth rate of crystallites and

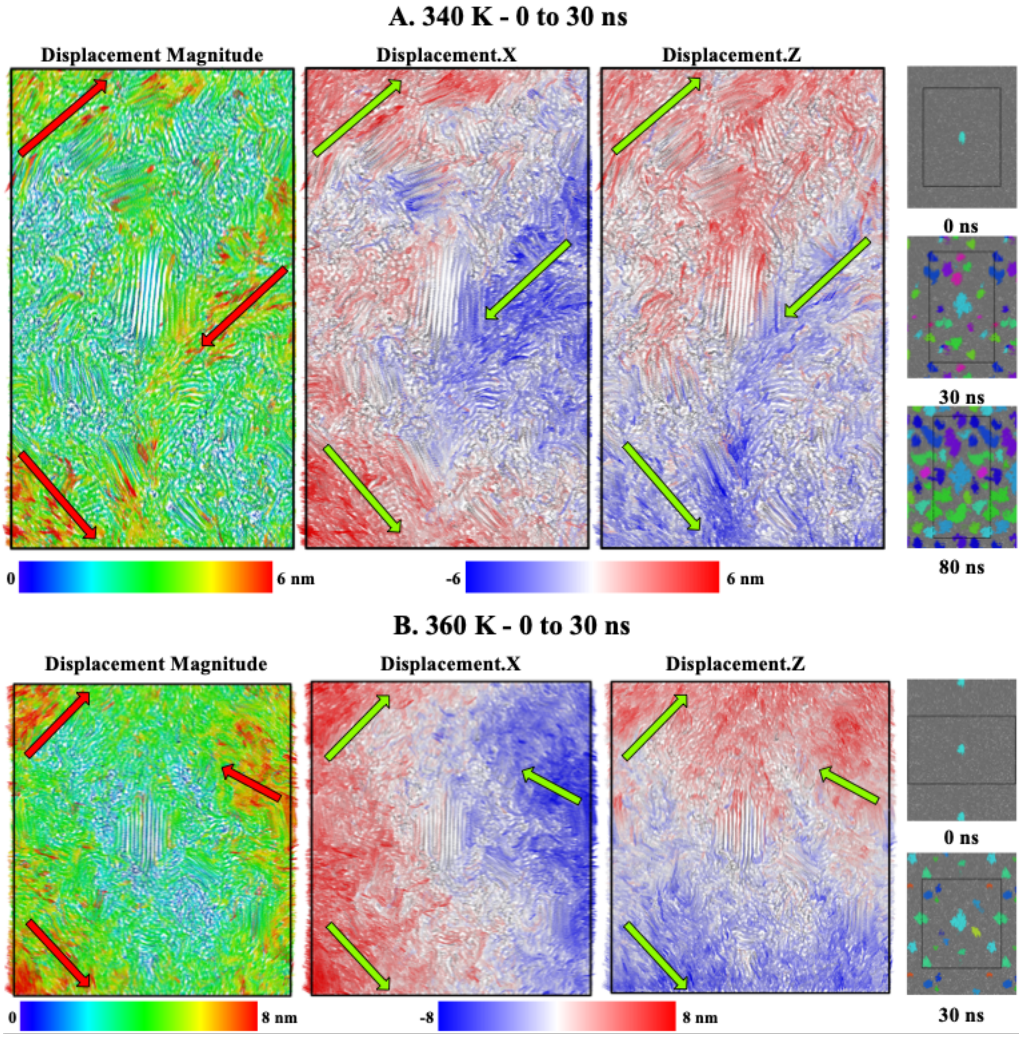

Figure 4.16. Atomic flow patterns (A) from 0 to 30 ns at 340 K, (B) from 0 to 30 ns at 360 K, (C) from 0 to 30 ns at 380 K, (D) from 50 to 80 ns at 380 K and (E) from 0 to 30 ns at 400 K. Displacement magnitude are colored based on the colormap.

Figure 4.16. continued

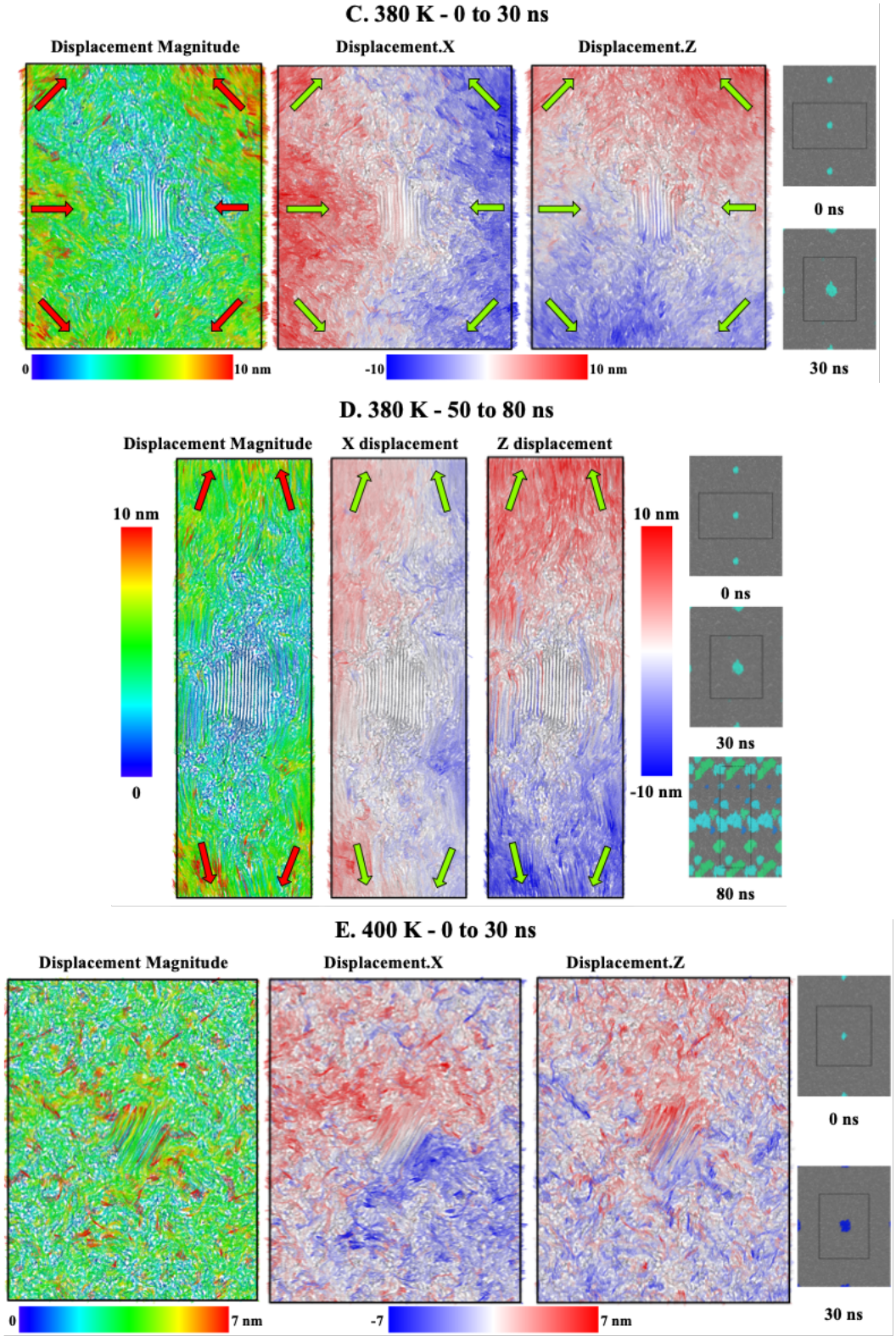

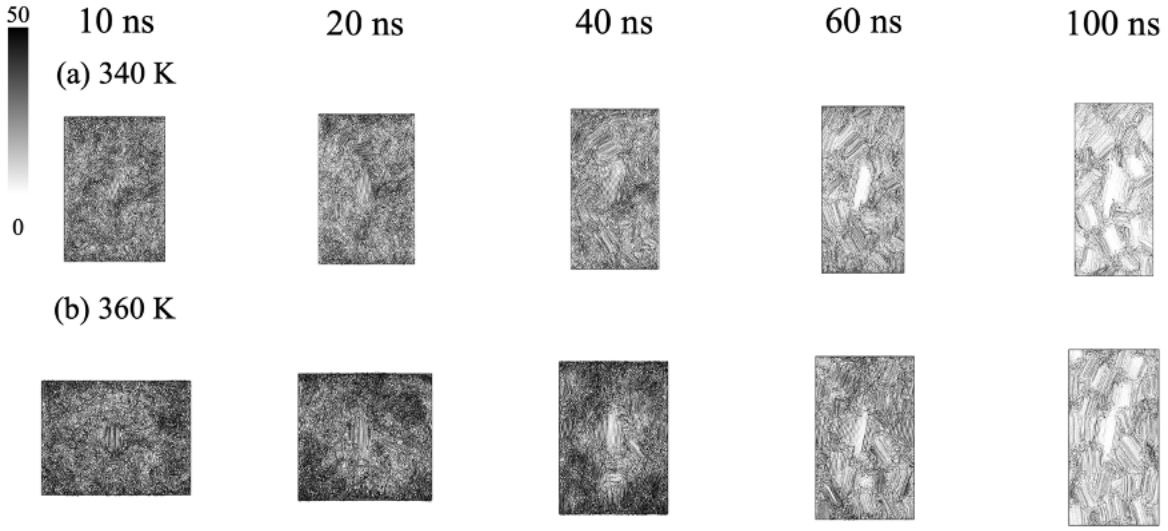

Figure 4.17. C atom velocity distribution during crystallization at (a) 340 K and (b) 360 K. [Color coding represent velocity in cm/s (0.01 nm/ns)]

increased chain mobility. At low temperatures, we also observe relatively low alignment; this is the result of fast rates of crystal nucleation which results in the growth of near randomly oriented crystallites. Significant change of molecular shape also occurs at 360 K and 380 K, see Figure 4.19(c) and indicates that crystal growth process greatly changes the shape of the polymer chains with preferred orientation especially for temperatures with high crystal growth rate. We believe the change of the molecular shape during the crystallization process is the atomic origin of dynamic heterogeneities and the key source of the formation of static disorder, which leads to further spherulitic growth. [166]

We note that macroscopic flow is known to result in chain alignment and has been shown to have an important effect on the resulting crystalline microstructure [43,44]. Our work shows, for the first time, the influence of nano-scale local flow caused by crystal growth on the relative orientation of adjacent crystallites. Furthermore, pre-ordering of chains in the amorphous phases has been postulated to explain experimental growth rates [87], the simulations provide direct observation of this process and indicate that it can play a role in NCB. We believe the deformation observed in our simulations, especially for cases at 360 K and 380 K is flow driven due to the initial crystal growth and subsequent growth of induced nuclei. While at 400K, the simulation exhibits a deviatoric strain similar to that at 360 K and this is due to the initial unbalanced liquid flow slightly turning the growing primary nucleus around. Key differences between 360 K and

400 K are: i) The significantly less chain alignment at 400K for the same deformation due to higher chain mobility, Figure 4.13(b) shows this very clearly. ii) At T=400 K we observe no induced nucleation events in the simulation time. [166]

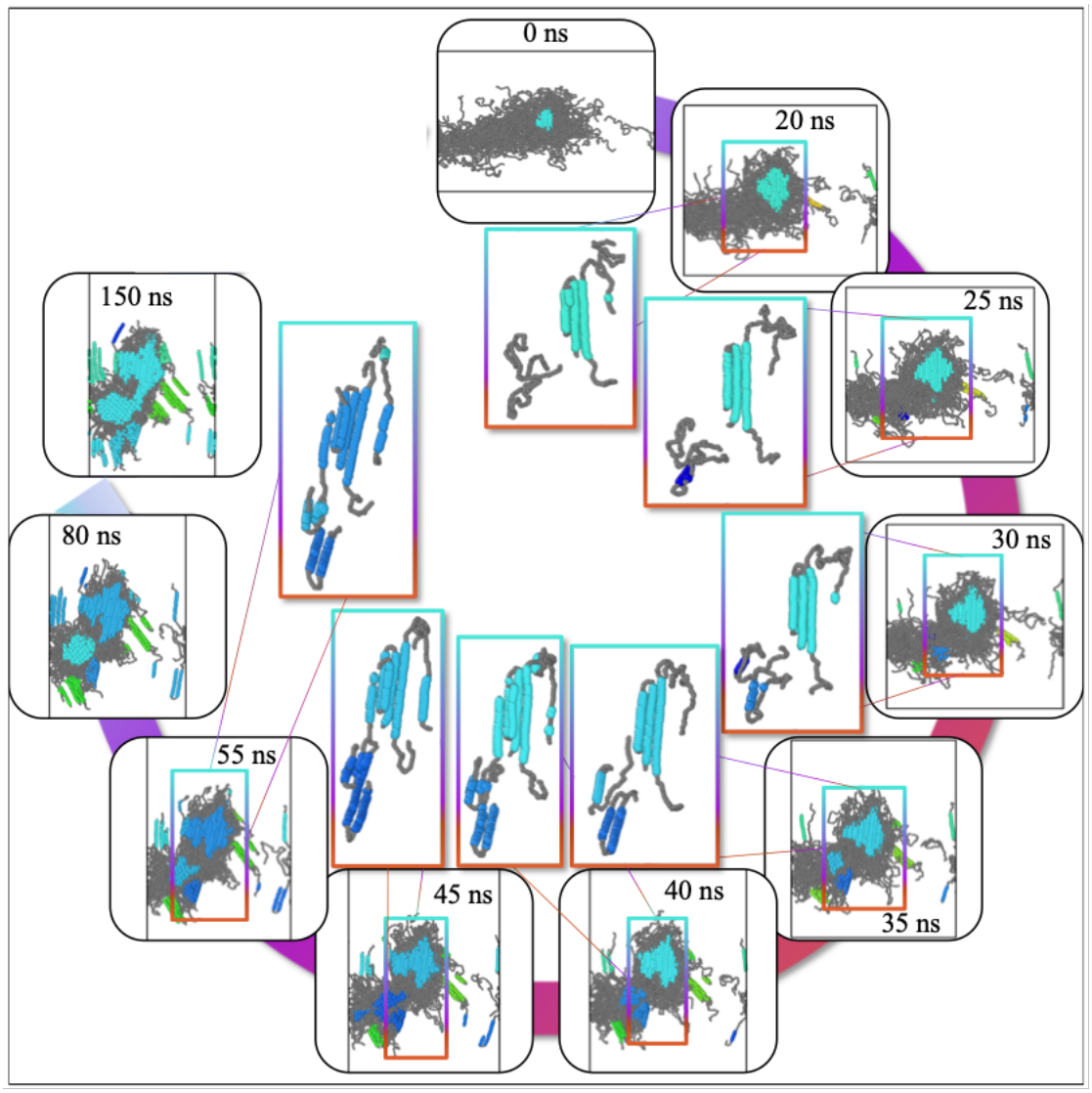

Figure 4.18. Molecular snapshots of the growth of the primary nucleus and the induced nucleation resulting in NCB at 360 K.

Induced nucleation. Having established that crystal growth results in local deformation which, in turn, leads to chain alignment in the liquid, we now track the process of induced nucleation to study possible causality. Figure 4.19(b) shows the evolution of crystallinity, which accounts for crystalline part of the total number of monomers in the system. Despite 400 K with

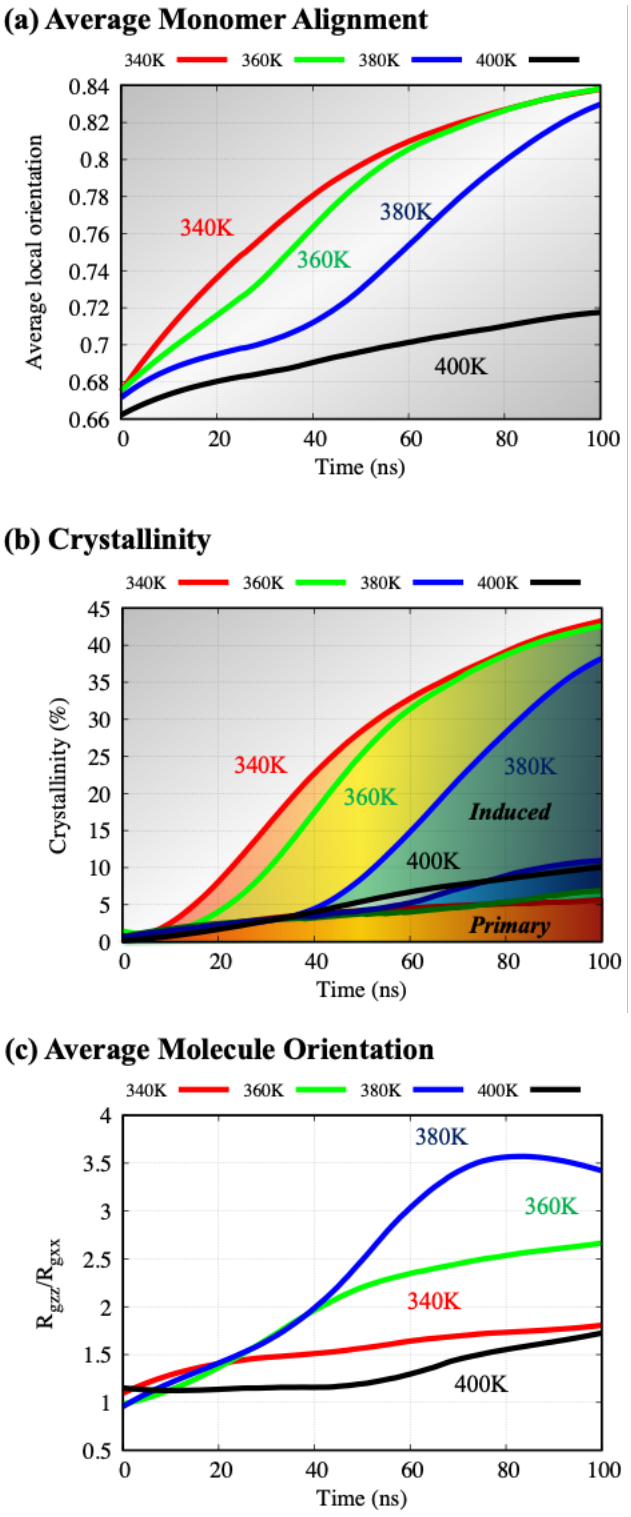

Figure 4.19. (a) Average local monomer alignment; (b) crystallinity as a fraction of the total number of monomers in the system and (c) average molecule orientation using $R_{g_{zz}}/R_{g_{xx}}$.

single crystal format, we observed that as temperature goes up, the induction time for induced nucleation increases. While in terms of primary crystal growth, we observed the highest growth rate happened at 380 K. This indicates a mismatch between the temperature dependence of the nucleation rate and the crystal growth rate. Figure 4.13(c) shows the relationship between alignment of the liquid chains and induced crystallinity (defined as the fraction crystalline monomers disregarding the primary crystallite). At high quench depths, T_c = 340 K, we find that fast nucleation rates result in induced lamella nucleating before any significant flow-induced chain alignment has occurred. We, thus, deem this nucleation to be spontaneous and assume it to be very similar to homogeneous nucleation. In contrast, nucleation at intermediate quench depths, most notably at 380 K, *chronologically follows* chain orientation. It takes 50 ns at 380 K to develop noticeable non-primary crystallinity over 5%, and significant chain orientation has already taken place. Thus, these induced crystallites nucleate from a liquid whose chains have been pre-aligned by the growth of the primary nucleus. Interestingly, the chain alignment between the primary nucleus and the surrounding material continues during the early parts of the induced nucleation and growth. This process leads to a significant alignment between primary and induced nuclei, see Figure 4.13(d), where we find a significant negative correlation between deviatoric strain and cluster angle deviation between primary and induced nuclei. With angles between 10° to 15° for intermediate quench depths, our results are consistent with experimentally measured angles between polycrystalline aggregates in spherulites [47]. As expected, high quench depths result in faster nucleation and consequently a much broader range of angles. The initial average misalignment for 340 K is 35°, indicating nearly random orientations. Detailed cluster orientation for all the nucleus are shown in Figure 4.10. The effect of quench depth on the nanoscale induced nucleation processes observed in the simulations is consistent with experimental observations. With increasing quench depth, the simulations show a transition from single crystals to induced nuclei with strong alignment with the primary nucleus and decreasing alignment with quench depth. This is in agreement with the gradual transition in polymer crystal morphology with reducing temperature from single crystals to uniform spherulites, with polycrystalline aggregates and axialites (an assembly of lamellae with large rather open and sometimes roughly spherical structures) as intermediate stages [81,179].

Molecular-level pictures. Having established the overall mechanisms of NCB, we now focus on the molecular level picture of the process by highlighting the time evolution of selected

chains. Figure 4.18 shows snapshots of the growth of the primary nucleus and the induced nucleation resulting in NCB. The insets highlight selected chains in the primary crystal (crystalline monomers are colored in cyan) and neighboring molecules in the undercool liquid that will eventually form an induced crystallite (crystalline monomers in the secondary grain are colored green). Up to 20 ns into the simulation, the selected liquid chains exhibit disordered, equiaxed, conformations. However, by 30 ns some of its segments are elongated along the orientation of the primary crystal. Quite interestingly, one of these chains is reeled into the primary crystal (see insets at 40 and 45 ns). This particular chain is not completely absorbed by the primary crystallite and it forms a bridge with the induced nuclei (green sections). The other selected chain in the liquid, never forms part of the primary nucleus but it aligns with it and eventually is reeled into the induced nucleus. Clearly, this induced nucleus exhibits a preferred orientation determined by that of the primary one. [166]

4.3.3 Discussion

As with any physics-based model our simulations are not without approximations. The use of a force field to describe atomic interactions introduces uncertainties but this is not expected to affect the mechanisms behind NCB. In addition, these mechanisms apply generally to polymeric materials and do not dependent on any specific property of PE or the chosen molecular weight. Thus, this mode of NCB is expected to be pervasive in polymers. Also, compared with isolated crystals in large sea of supercooled liquids, the relatively small size of simulation cells with periodic boundary conditions may lead to overestimation of local deformation levels. This can enhance the level of flow-induced chain orientation, but the effect would still be present in the case of an isolated grain. Finally, it is important to stress that the characteristic size and time scales of MD limit our simulations to the initial stages of polymer fibril growth and branching. However, given the general nature of the auto-deformation process, the resulting chain alignment in the undercooling liquid, and induced nucleation, we believe that the processes captured in the simulations would continue to operate in the later stages of spherulite growth in polymers. [166]

4.4 Conclusion and outlook

In summary, large-scale MD simulations of polymer crystallization captured a novel mode of NCB during the initial stages of polymer fibril growth, responsible for the formation of spherulites. The simulations revealed that crystal growth results in unexpectedly large local deformation which, in turn, causes the alignment of the chains in the neighboring undercooled liquid with those of primary nucleus. At intermediate quench depths, the timescales of chain alignment are shorter than those of nucleation resulting in induced nucleation of secondary grains within a pre-aligned liquid and chain orientation strongly correlated to that of the primary grain. The predicted range of misalignment associated with NCB in the simulations is consistent with experimental observations in spherulites and the dependence on quench depth consistent with experimentally observed changes in morphology [47,81]. At large quench depths, fast nucleation rates reduce the amount of flow and chain alignment prior to nucleation, resulting in a fine polycrystalline structure with nearly random orientations. Thus, the key ingredients for NCB and the formation of fibrils in pure polymeric systems is relatively fast grain growth with respect to nucleation to enable local alignment of the liquid prior to nucleation but enough quenching to preclude growth to completely dominate nucleation, which results in large grains. [166]

Our simulations solve a puzzle that has intrigued researchers for over half a century and, we believe, will elicit additional experimental and simulation work. The goal of our work also meets the need of bridging the gap between MD and phase field modeling on polymer materials in terms of understanding the temperature effects of branching both qualitatively and quantitively. With more enhanced capability and longer time scales in this type of polymer MD simulations, especially on mechanisms of secondary nucleation relating to the inherently glassy dynamics of polymeric materials, phenomenon attributed to the "decoupling" between rotational and translational mobility in glass-forming liquids and fluid flow in crystallizing systems that seems to be associated with the volume changes that occur with crystallization, we could eventually link our branching angle with the scalar orientation field θ developed in orientation-field-based phase-field models. With phase field simulations having the ability to predict a variety of polymer spherulite shapes [48,49,51,54], future multi-scale models have the potential to provide a description of microstructure development from first principles. Such capability would be invaluable in areas ranging from food processing [162], materials science [180], and medicine [164]. Furthermore, a molecular understanding of the formation of polycrystalline

structures in polymers is also of practical importance. The results could enable a more fundamental understanding of crystallization kinetics and may enable the design of tailored polymer microstructures for specific applications by the appropriate choice of molecular composition and processing conditions. [166]

5. POLYMER CRYSTAL STRUCTURE GENERATOR AND ANALYSIS SOFTWARE

5.1 Introduction

With enhanced ability in computational science, simulation starts to become an essential investigation method to provide thermodynamic insights at this molecular level. In terms of polymer crystallinity, the main problems and challenges remain unresolved, including detailed understanding of melting, annealing and crystallization, molecular conformation, crystal structure and mesoscale morphology determination and control. With the fierce debate on crystal growth models and the validity and extent of chain folding, it is obvious that in the near future, research on the crystal structure and crystallization mechanism at molecular level and corresponding predictive simulations will become a huge demand for exploration of mechanical, optical and other physical properties of polymeric materials.

Despite significant importance, simulation software and tools targeted to build and analyze polymer crystal structures is still lacking. For polymer builders only a few options are available, these include nanoHUB Polymer Modeler [130,131], Polymer Builder module in Cerius2 Builders and MedeA Amorphous Materials Builder [181]. While these builders are mainly focus on building amorphous polymer structures with no features on creating polymer crystal structure. And due to complex crystallography in polymer systems, molecular visualization and analysis software like OVITO and VMD also does not have features to analyze crystallinity in polymers. The goal of polymer crystal structure generator and analysis software (PolymerXtal) is to generate polymer crystal structure based on monomer, tacticity, helicity, chiriality and unit cell information as well as to give out the corresponding XRD patterns, see Figure 5.1.

In this chapter, I will briefly introduce several aspects of polymer crystal structures and present PolymerXtal, a software designed to build and analyze molecular-level polymer crystal structures. PolymerXtal provides a standardized process to generate polymer crystal structure based on monomer, tacticity, helicity, chiriality and unit cell information and analyze the crystallinity in polymer systems with given atom trajectories. These features have allowed PolymerXtal to lead further investigations of semi-crystalline polymers where most properties are governed by the crystalline microstructure and promote future research endeavors in the area of crystalline polymer simulations.

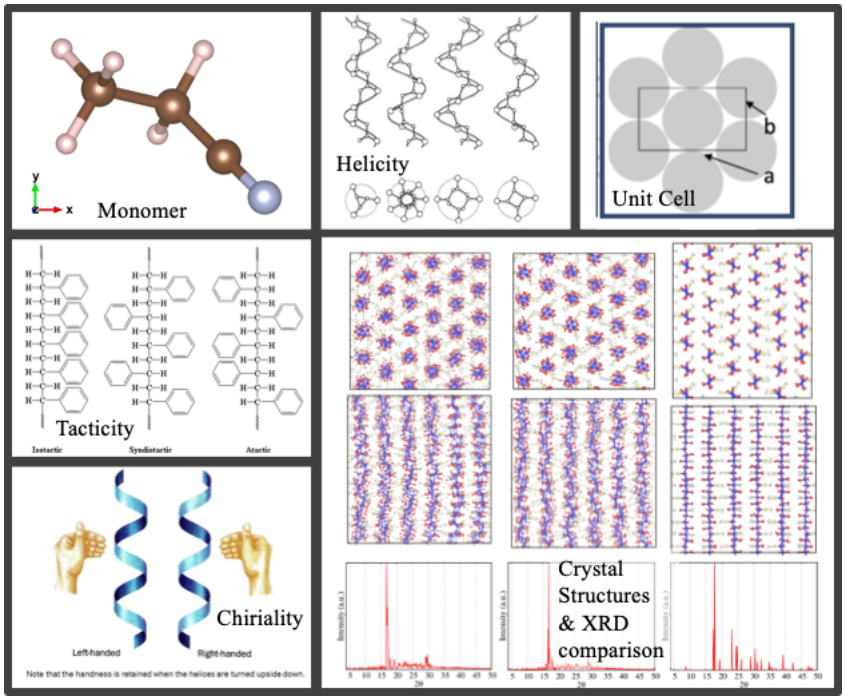

Figure 5.1. Information to generate polymer crystal structure using PolymerXtal (monomer, tacticity, helicity, chiriality and unit cell information) and output crystal structures with XRD.

5.2 The structure of macromolecules

5.2.1 Constitutional isomers

Constitutional isomers, also called structural isomers, have the same molecular formula but different connectivity. These compounds can only be converted into each other by breaking and reforming one or more bonds connected to one or more chiral centers in different spatial directions. Symmetrical monomers without a chiral center such as ethylene and tetrafluoroethylene can be joined together in only one way. Monosubstituted (vinyl) monomers, on the other hand, may be joined together in three distinct ways for adjacent repeat units, see Figure 5.2. In the case of free radical or ionic polymerization, the mode of monomer addition to the chain growth center is mainly head-to-tail (or 1,3-placement), so that the pendant groups (and chiral centers) are on every other carbon atom in the polymer backbone. Polymers that grow predominantly in this fashion include propylene, styrene, vinyl chloride, acrylonitrile and (meth)acrylates. [182–184].

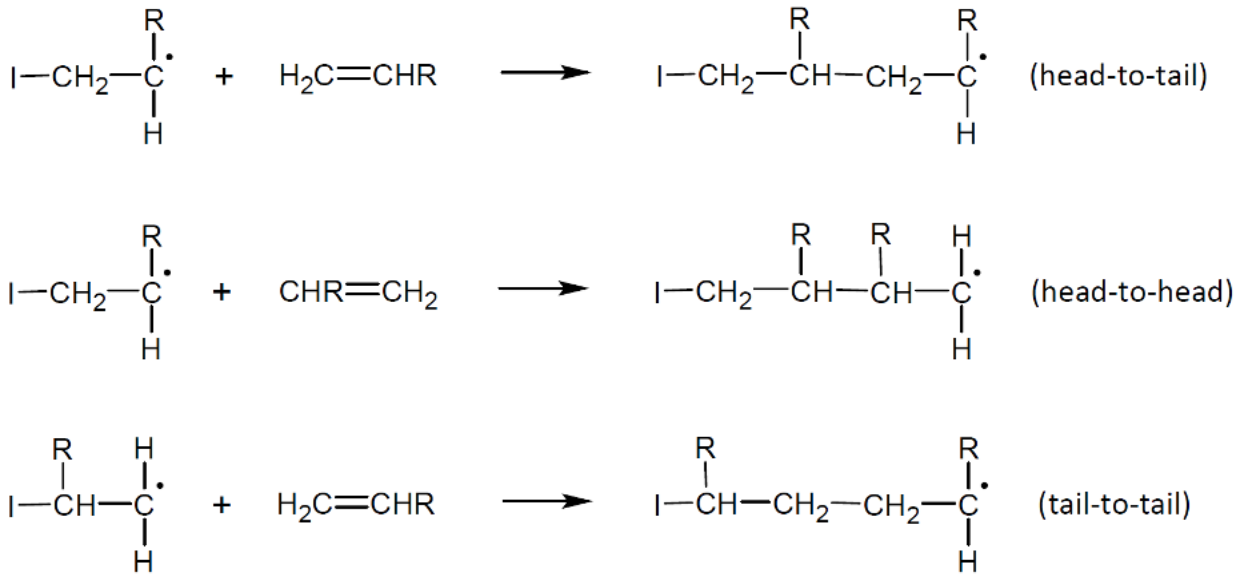

Figure 5.2. Illustration of head-to-tail, head-to-head and tail-to-tail arrangements. Figure adapted from Ref. [185].

5.2.2 Tacticity

The physical properties of a polymer not only depend on the types of monomers that make up the polymer, but also on the stereoregularity along its chain. For asymmetric linear chains, the side groups can be arranged in an orderly or completely random arrangement. The spatial order is called tacticity. The side groups in *isotactic* polymers are arranged with the same configuration while those in *syndiotactic* polymers are arranged alternatively around their chiral center. *Atacitc* or *heterotactic* polymers are usually with side groups arranged randomly, [185] see tacticity illustration in Figure 5.1.

5.3 The microscopic structure of crystals

5.3.1 Motif and repetition scheme

The concept of repetition implies an operation by which the system is brought into a state indistinguishable from the initial state. Any such operation will be called a symmetry operation. For the purpose of description, the aggregate of atoms of the crystal which is repeated is called a motif. The motif can be as simple as a single atom or ion, but it can also be a part of a molecule,

an entire molecule, or even several molecules. For the structure of polyethylene (PE), the motif CH_2 has a point group symmetry *mm2*. The space group is P*nma*. Figure 5.3 shows the symmetry and the *bc* and *ab* projections of the unit cell pf PE given by Bunn [186].

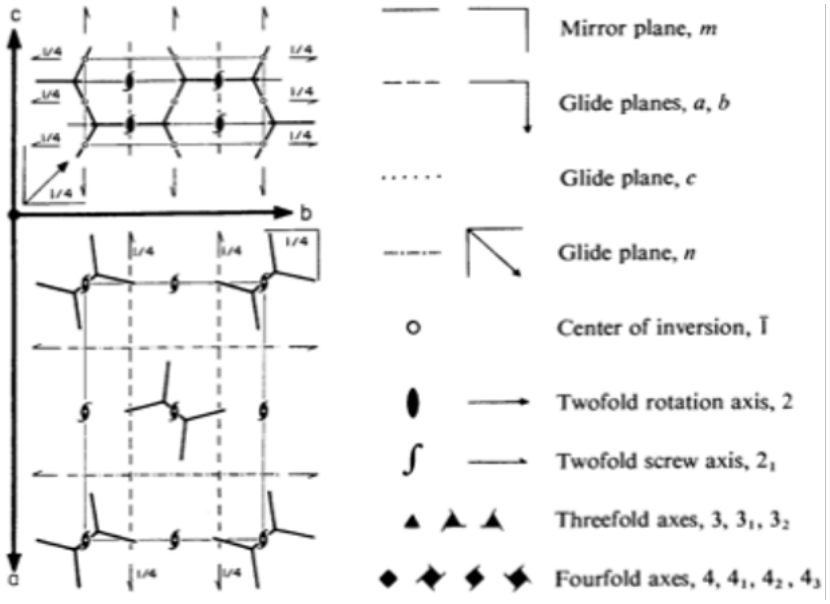

Figure 5.3. Symmetry and unit cell of PE (left). Heavy lines mark the directions of chemical bonds. Thin lines outline the unit cell. Each projection contains all symmetry elements as the legend of standard symbols for symmetry elements on the right. Figure adapted from Ref. [187].

5.3.2 Structures of minimum free energy

Trans-gauche conformation. The trans-gauche conformation of the polymer chain can be interchanged by simply rotating the bond connecting each part [188]. In general, the potential of a molecule as a function of rotation angle ϕ of can be expressed as

$$U(\phi) = U_{steric} + U_{rot} + U_{val} \tag{5.40}$$

The first term, U_{steric}, represents the steric interaction in the case of large substituents. For the ethane molecule is was shown to be of little importance. The next term, U_{rot}, represents the intrinsic hindering potential. Since its origin is mainly orbital overlap, it is similar in form for many molecules. If at least one of the rotating sets of orbitals has the symmetry *3m* with the threefold axis along the rotation axis, the intrinsic potential does not change on replacing the rotation angle ϕ by $\phi \pm 2\pi/3$ because of symmetry. In almost all bonds at least one set of sp^3 hybrid orbitals is

involved which satisfies the symmetry *3m*. Knowing little about the functional form of U_{rot}, one may expand it in a Fourier series taking into account the symmetry condition:

$$U_{rot} = \left(U^{(3)}/2\right)(1 - \cos 3\phi) + \left(U^{(6)}/2\right)(1 - \cos 6\phi) + \ldots \qquad (5.41)$$

Furthermore, experiments have shown that $U^{(6)}$ is usually so small that it can be neglected. Assuming $U^{(6)} \approx 0$, $U^{(3)}$ represents the barrier height of the potential, U_0. A plot of Eq. (5.41) is shown in Figure 5.4. The thrid term, U_{val}, again, is only of importance for larger substituents.

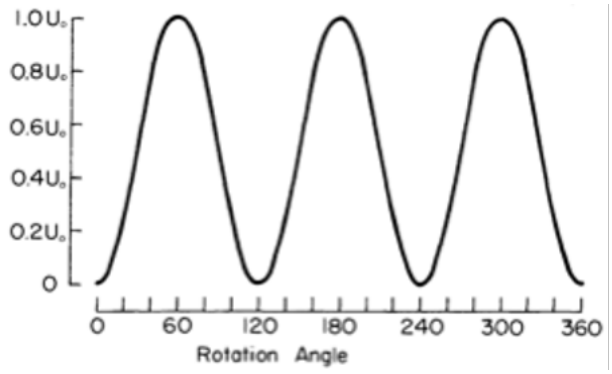

Figure 5.4. Rotational potential energy of ethane. Drawing of the potential $U = (U_0/2)(1 - \cos 3\phi)$. Figure adapted from Ref. [187].

Helices. Before packing of macromolecules in a crystal can be discussed, the low-energy conformations of the backbone chain have to be evaluated. Since the intramolecular rotational potential energy is, at least for carbon chains, larger in magnitude than the packing energy. As long as a repetitive sequence of backbone atoms makes up the macromolecule, a more or less extended conformation, generally described by a helix, will result. The intramolecular potential energy causes a macromolecule to take on a distinct, generally helical, conformation. The symbol for the helix in point net notation is A*u/t; it represents a helix of the class A (helix with motifs of A chain atoms) which has u motifs and t turns of the helix per translatory identity period c along the helix axis z. A number of helices are illustrated in helicity of Figure 5.1.

Packing of macromolecules. Macromolecules with sufficient overall regularity were shown to have a unique extended chain conformation of lowest energy. Their structure is generally described by relating the suitably chosen motifs to a one-dimensional, helical lattice. A cylinder is the most symmetric body which approximates to some degree a macromolecule in its

extended chain conformation. The packing density k for a close-packed array of cylinders is 0.907, the coordination number is 6, and the symmetry, hexagonal (*6/mmm*). An arrangement with coordination number 4 and tetragonal symmetry *4/mmm* has, in contrast, only a packing density of 0.785. Both packing densities are still higher than that of close-packed spheres (k = 0.741), because of the solid structure along the cylinder axis.

5.4 Software architecture and functionality

In this section, I will briefly introduce PolymerXtal, a software designed to build and analyze molecular-level polymer crystal structures. PolymerXtal provides a standardized process to generate polymer crystal structure based on monomer, tacticity, helicity, chiriality and unit cell information and analyze the crystallinity in polymer systems with given atom trajectories. These features have allowed PolymerXtal to lead further investigations of semi-crystalline polymers where most properties are governed by the crystalline microstructure and promote future research endeavors in the area of crystalline polymer simulations.

Overall, PolymerXtal are written in standard python and some of the power using PolymerXtal incorporates third-party open source software, like Ovito [189], LAMMPS [136] and PolymerModeler [130,131] tool from nanoHUB.org [132]. In these cases, proper installation of external software is considered a prerequisite to use PolymerXtal. PolymerXtal can be used interactively through any python interface and importing *polymerxtal* library.

The *polymerxtal* python package is composed of three core parts. The system part including *data*, *io* and *visualize* modules is capable of interpreting, generating, modifying and visualizing molecular data. The generation part including *crystal*, *polymod* modules is responsible for generating various polymer crystal structures. And the analysis part contains *xrd* and *energy* modules. This part is mainly handling output of radial distribution function (RDF), XRD, neutron and/or X-ray weighted static structure factors (SSF), as well as energy profiles including intra- and inter- molecular energies. Detailed software architecture and functionality is showing in Figure 5.5.

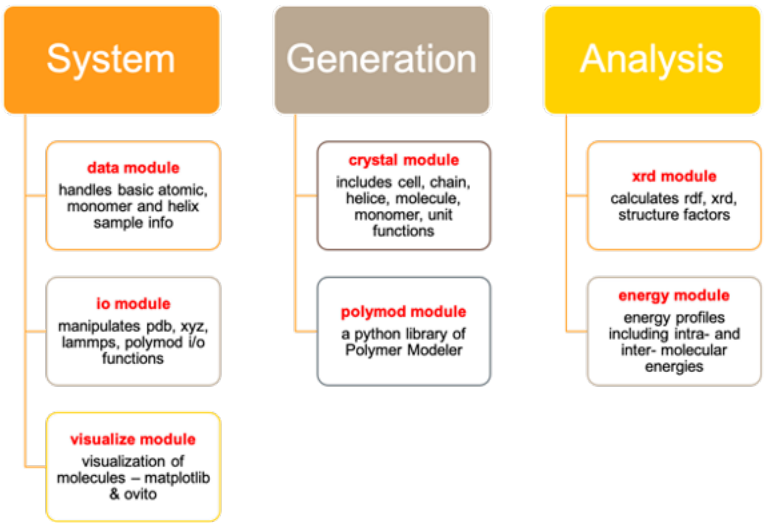

Figure 5.5. PolymerXtal software architecture and functionality.

5.4.1 System

polymerxtal.data module stores basic atomic, monomer and helix sample info. Elements included here are H, C, N, O, P, F, S, Cl, Si and Br. Monomers for polyacrylonitrile (PAN), PE, polyoxymethylene (POM), polypropylene (PP), PS, polytetrafluoroethylene (PTFE) and polyvinyl chloride (PVC) are also stored in this module. Example PAN monomer is illustrated in monomer of Figure 5.1. Helix samples for helice 2*3/1, 2*2/1 and 2*1/1 (planar zig-zag) are also included at here. User can access the smaple helix by using *sample_chain(helice)* with *helice* specified by **Helice** class. This class will be covered in the following generation - *polymerxtal.crystal* section.

polymerxtal.io module manipulates all the read and write functions about pdb xyz, lammps data & dump files. It also handles functions interpreting input and output files from PolymerModeler [130,131] tool from nanoHUB.org [132].

polymerxtal.visualize module is mainly used to visualize of molecules with employed third party software which have been designed specifically to accomplish these tasks efficiently. The module requires pre-install of matplotlib and ovito python library [189].

5.4.2 Generation

polymerxtal.crystal module has class definitions for components of a polymer crystal systems such as includes **Chain** and **Cell**. **Chain** class includes features like **PolymerType**,

Helice, number of monomers, tacticity, chiriality, as well as ratio of constitutional isomers (head-to-tail, head-to-head and tail-to-tail connections). Figure 5.6 shows an example of 40-monomer isotactic PAN with 10 % head-to-head and tail-to-tail connections by

```
>>> from polymerxtal import Helice, Chain
>>> chain = Chain(polymer_type='PS',
>>>               helice=Helice(2, 1, 1),
>>>               tacticity='isotactic',
>>>               head_tail_defect_ratio=0.1)
```

Type object **PolymerType** defines basic configurations of a polymer type with name, path to monomer pdb file, indices for backbone atoms and side atom specified where backbone atoms are the atoms in the monomer which will become backbone of the polymer chains and side atom is the special atom directly connecting to the backbone which could determine the tacticity, see Figure 5.7. Object **Helice** defines helix notation of A*u/t discussed in Sec. 5.3.2 with A - chain (backbone) atoms of a motifs, u - motifs and t - turns of the helix. Number of monomers, tacticity of isotactic, atactic or syndiotactic, chiriality of left or right (see chiriality illustration in Figure 5.1) can also be specified within **Chain** class. **Backbone** object will be constructed when execute *chain.build_chain()* which exams all the configurations of a monomer by varying head and tail atoms which will become the basic unit configuration when building up the polymer chain, see Figure 5.7. Examples of various helix chains with different polymer types and helices are shown in Figure 5.8. **Cell** class includes features of **Chain** as well as unit cell length ***a***, ***b***, ***c*** (Å) and angle ***α***, ***β***, ***γ*** (°) where ***c*** can be automatically generated with *cell.chain.build_chain()*. Other parameters could also be generated with packing functions. With default hexagonal packing, user can specify a target density with *cell.hexagonal_packing(density)*.

Figure 5.6. Illustration of 40-monomer isotactic PAN with 10 % head-to-head and tail-to-tail connections

polymerxtal.polymod module contains the python library of PolymerModeler [130,131] related to building rod-like polymers. All the execution of *chain.build_chain()* will generate an input file *run_polymod.txt* with specified backbone configurations and

run_polymod('run_polymod.txt') would generate a pdb file with the as-built helix polymer chains.

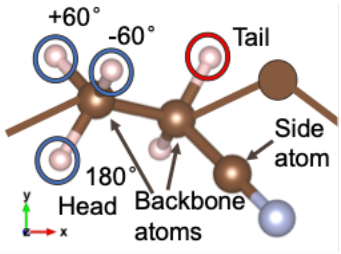

Figure 5.7. Illustration of backbone atoms and side atom for **PolymerType** definition as well as head and tail atoms for **Backbone** definition.

5.4.3 Analysis

polymerxtal.xrd module is mainly responsible for calculation of RDF, XRD and neutron and/or X-ray scattering SSF. This module executes with functions of *sfac()* which gives output of both neutron and X-ray weighted SSF information, *rdf()* which gives output RDF information and *xrd()* which gives output XRD information. This module requires integration with the LAMMPS simulation package [136].

polymerxtal.energy module is mainly responsible for calculation of intra- and inter-molecular energies. This module requires integration with the LAMMPS simulation package and user needs to provide potential.mod file with force field information [136].

5.5 Conclusion and future work

PolymerXtal has been developed as a software to generate polymer crystal structure based on monomer, tacticity, helicity, chiriality and unit cell information as well as to give out the corresponding XRD patterns. We believe this software will be useful to the computational molecular science community, especially for macromolecular scientists and researchers. This will lead to further investigations of semi-crystalline polymers where most properties are governed by the crystalline microstructure. We will continue to lead the effort to improve the software and add more analysis features regarding crystallinity in polymer systems, like examples in Figure 5.9. Also, more defect features like chain ends or loops, as they are always present in polymer system,

are also greatly needed. We believe upon improvement with PolymerXtal, our work will help promote future research endeavors in polymer crystals.

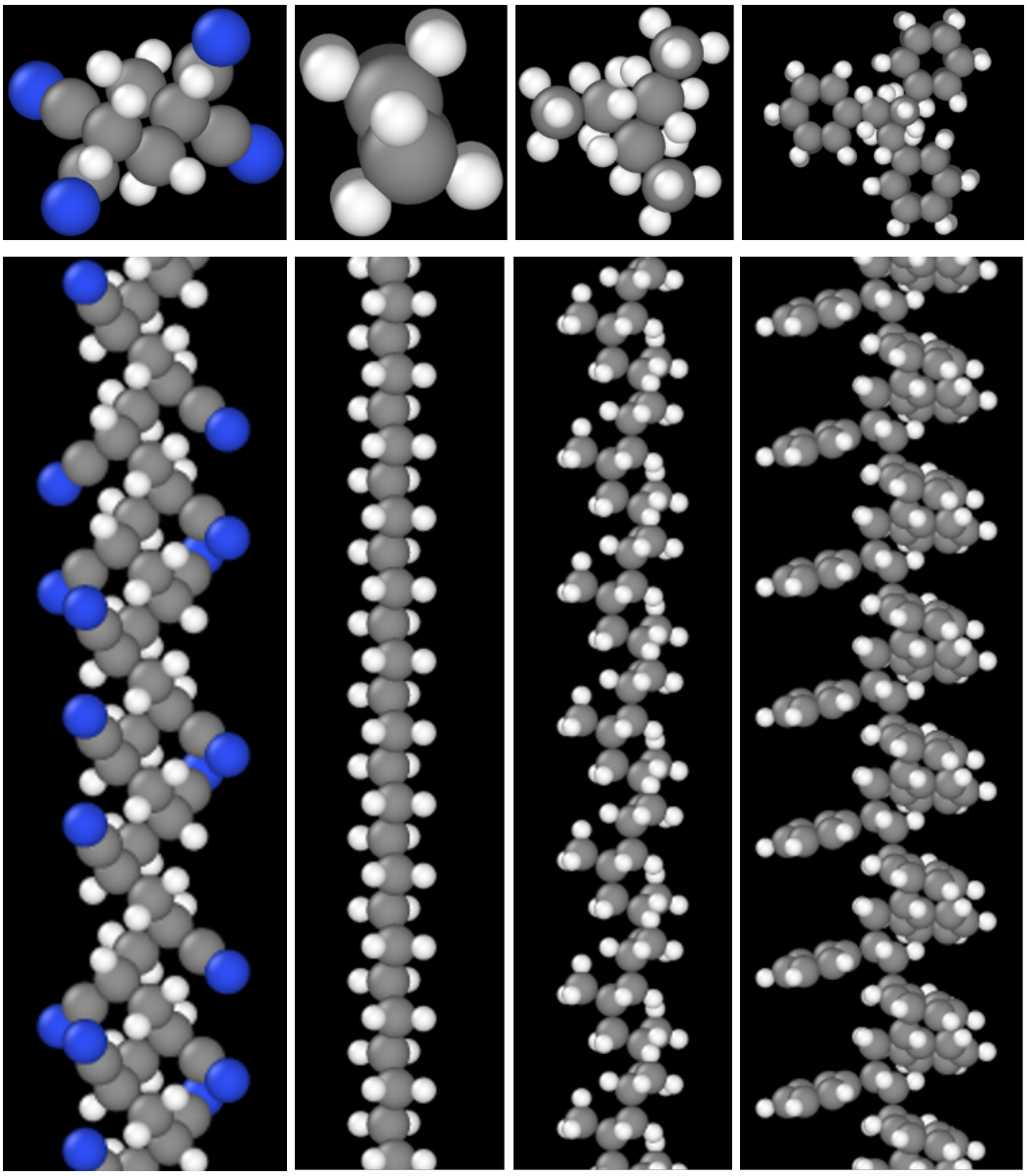

Figure 5.8. Illustration of various helix chains built by PolymerXtal. From left to right: syndiotactic PAN Helix 2*2/1, PE Helix 2*1/1 (planar zig-zag), isotactic PP Helix 2*3/1 and isotactic PS Helix 2*3/1. Top views on the top row and front views on the bottom row.

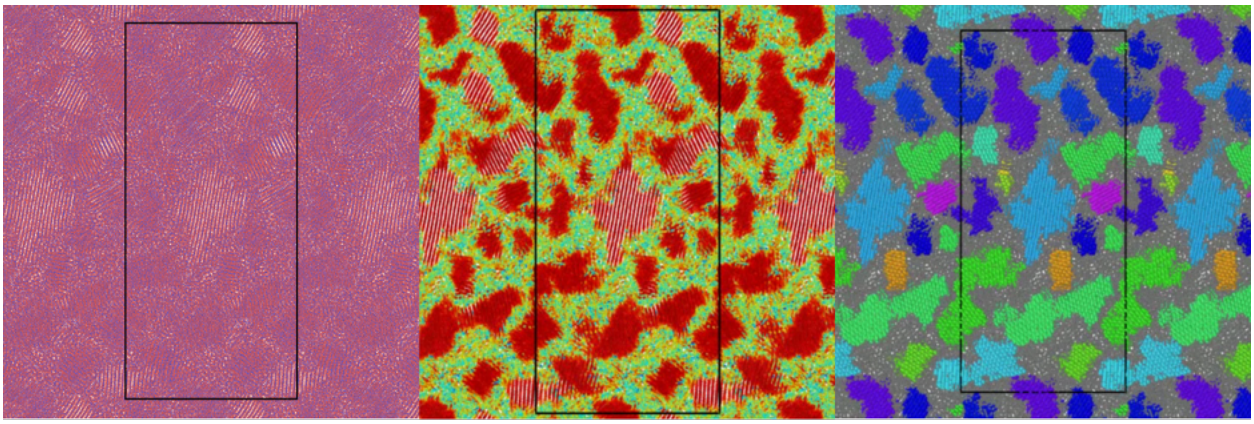

Figure 5.9. Crystallinity analysis from atom trajectory. [Original trajectory (left); Crystallinity analysis (middle), red color represents crystalline region, green color represents amorphous region; Crystal orientation analysis (right), dark grey represents amorphous region and other colors represent different crystal orientations]

6. CONCLUSION

Polymer crystals and crystallization are a broad field as they cover a wide range of applications at different organizational level with various length scales from sub-molecules to morphology. Our work covered in this dissertation involves several aspects of this broad field.

First, we use molecular dynamics (MD) simulations to predict the molecular structure of the crystalline regions of spun PAN used in the production of carbon fibers (CFs) and known to critically affect the microstructure and, consequently, the properties of the final fiber. We characterized how tacticity and the arrangement of torsional angles along the backbone affect packing of the chains and lattice parameters. Most configurations, regardless of tacticity, loose periodicity along the chain axis during relaxation resulting in pseudo-crystalline structures. Simulated X-ray diffraction (XRD) patterns of these pseudo-crystalline structures show excellent agreement with recent experimental measurements and reveal that intermolecular spacing decreases as backbone trans/gauche ratio increases corresponding to different experimental conditions. Stability and stiffness also increase as backbone trans/gauche ratio increases. A syndiotactic system with planar zig-zag configuration results in crystalline order along the c axis; this more ordered structure has the lowest potential energy and highest stiffness of all structures studied. The predicted XRD pattern differs significantly from those of the pseudo-crystalline structures but, interestingly, it matches the multi-peak fingerprint reported experimentally in solution-grown single crystals of PAN. The simulations shed light into longstanding discrepancies in XRD patters of PAN precursors.

Second, MD simulations in polyethylene reveal the molecular-level origin of non-crystallographic branching and the initial formation of fibrils in spherulites, the most ubiquitous of polycrystalline microstructure of polymers developed under a wide range of conditions by the subsequent branching of crystalline lamella that results in an overall spherical shape. We find that the growth of crystalline lamella by reeling in and folding of polymer chains causes surprisingly large local deformation which, in turn, aligns the chains in the neighboring undercooled liquid. Thus, subsidiary grains nucleate with preferred orientations resulting in fibril growth with branching at small angles, consistent with those observed experimentally.

Final, PolymerXtal has been developed as a software to generate polymer crystal structure based on monomer, tacticity, helicity, chiriality and unit cell information as well as to give out the

corresponding XRD patterns. We believe this software will be useful to the computational molecular science community, especially for macromolecular scientists and researchers. This will lead to further investigations of semi-crystalline polymers where most properties are governed by the crystalline microstructure. We will continue to lead the effort to improve the software and add more analysis features regarding crystallinity in polymer systems. Also, more defect features like chain ends or loops, as they are always present in polymer system, are also greatly needed. We believe upon improvement with PolymerXtal, our work will help promote future research endeavors in polymer crystals.

Though my personal research path has touched several important aspects of polymer science, we note that there are still many have been left aside. Current available theories and/or models provide physical molecular diagrams of how polymer crystallization occurs, while they still cannot predict the crystallization behavior of polymers. Therefore, we look forward to new theories and simulations based on different conditions and environments to further develop many physical principles in this field.

REFERENCES

[1] B. Lotz, T. Miyoshi, and S. Z. D. Cheng, Macromolecules (2017).

[2] S.-J. Park, (2015).

[3] C. D. Warren, Present. 20th Eur. Photovolt. Sol. Energy Conf. Exhib. 1 (2010).

[4] Y. Liu and S. Kumar, Polym. Rev. **52**, 234 (2012).

[5] M. S. A. Rahaman, A. F. Ismail, and A. Mustafa, Polym. Degrad. Stab. **92**, 1421 (2007).

[6] X. Huang, Materials (Basel). **2**, 2369 (2009).

[7] E. Fitzer, Carbon N. Y. **27**, 621 (1989).

[8] N. Yusof and A. F. Ismail, J. Anal. Appl. Pyrolysis **93**, 1 (2012).

[9] H. Chang, A. T. Chien, H. C. Liu, P. H. Wang, B. A. Newcomb, and S. Kumar, ACS Biomater. Sci. Eng. **1**, 610 (2015).

[10] E. Y. J. Robert G and Choueiri, Acad. Press **3**, 125 (2002).

[11] P. Morgan, *Carbon Fibers and Their Composites* (CRC press, 2005).

[12] L. Tan, A. Wan, and D. Pan, Mater. Lett. **65**, 887 (2011).

[13] L. Tan, S. Liu, K. Song, H. Chen, and D. Pan, Polym. Eng. Sci. **50**, 1290 (2010).

[14] H. G. Chae, B. A. Newcomb, P. V. Gulgunje, Y. Liu, K. K. Gupta, M. G. Kamath, K. M. Lyons, S. Ghoshal, C. Pramanik, L. Giannuzzi, K. Şahin, I. Chasiotis, and S. Kumar, Carbon N. Y. **93**, 81 (2015).

[15] J. C. Chen and I. R. Harrison, Carbon N. Y. **40**, 25 (2002).

[16] R. W. P. and L. J and Li, J. Appl. Polym. Sci. **52**, 1667 (1994).

[17] M. L. Minus and S. Kumar, JOM (2005).

[18] T. -H Ko, J. Appl. Polym. Sci. (1991).

[19] R. Setnescu, S. Jipa, T. Setnescu, W. Kappel, S. Kobayashi, and Z. Osawa, Carbon N. Y. (1999).

[20] T.-H. Ko, T.-C. Day, and M.-F. Lin, J. Mater. Sci. Lett. **12**, 343 (1993).

[21] T. H. Ko, S. C. Liau, and M. F. Lin, J. Mater. Sci. (1992).

[22] Z. Wangxi, L. Jie, and W. Gang, in *Carbon N. Y.* (2003).

[23] F. Liu, H. Wang, L. Xue, L. Fan, and Z. Zhu, J. Mater. Sci. (2008).

[24] I. A. S. Edwards, R. Menendez, and H. Marsh, *Introduction to Carbon Science* (Butterworth-Heinemann, 2013).

[25] P. Bajpai, *Update on Carbon Fibre* (2013).

[26] P. C. Hiemenz and T. P. Lodge, *Polymer Chemistry* (CRC press, 2007).

[27] I. L. Hosier, D. C. Bassett, and A. S. Vaughan, Macromolecules (2000).

[28] I. L. Hosier and D. C. Bassett, in *Polymer (Guildf).* (2000).

[29] X. Wang, R. Liu, M. Wu, Z. Wang, and Y. Huang, Polymer (Guildf). (2009).

[30] H. Kajioka, M. Hikosaka, K. Taguchi, and A. Toda, Polymer (Guildf). (2008).

[31] D. Patel and D. C. Bassett, Proc. R. Soc. London. Ser. A Math. Phys. Sci. **445**, 577 (1994).

[32] H.-M. Ye, J. Xu, B.-H. Guo, and T. Iwata, Macromolecules **42**, 694 (2008).

[33] H. M. Ye, J. S. Wang, S. Tang, J. Xu, X. Q. Feng, B. H. Guo, X. M. Xie, J. J. Zhou, L. Li, Q. Wu, and G. Q. Chen, Macromolecules (2010).

[34] J. Xu, B. H. Guo, J. J. Zhou, L. Li, J. Wu, and M. Kowalczuk, Polymer (Guildf). (2005).

[35] A. Toda, K. Taguchi, M. Hikosaka, and H. Kajioka, Polym. J. (2008).

[36] A. J. Lovinger, J. Appl. Phys. (1978).

[37] G. Ryschenkow and G. Faivre, J. Cryst. Growth (1988).

[38] J. Bisault, G. Ryschenkow, and G. Faivre, J. Cryst. Growth (1991).

[39] P. F. James, J. Amer. Ceram. Soc., Ohio **1**, (1982).

[40] H. W. Morse, C. H. Warren, and J. D. H. Donnay, Am. J. Sci. 421 (1932).

[41] P. J. Phillips, Elesvier, Amsterdam **2**, 1169 (1993).

[42] A. G. Shtukenberg, Y. O. Punin, E. Gunn, and B. Kahr, Chem. Rev. (2012).

[43] F. L. Binsbergen, Nature **211**, 516 (1966).

[44] S. Kimata, T. Sakurai, Y. Nozue, T. Kasahara, N. Yamaguchi, T. Karino, M. Shibayama, and J. A. Kornfield, Science (80-.). (2007).

[45] W. H. F. Talbot, in *Abstr. Pap. Print. Philos. Trans. R. Soc. London* (1837), pp. 388–390.

[46] W. H. F. Talbot, Philos. Trans. R. Soc. London 29 (1837).

[47] J. H. Magill, J. Mater. Sci. (2001).

[48] L. Gránásy, T. Pusztai, J. A. Warren, J. F. Douglas, T. Börzsönyi, and V. Ferreiro, Nat. Mater. (2003).

[49] L. Gránásy, T. Pusztai, T. Börzsönyi, J. A. Warren, and J. F. Douglas, Nat. Mater. (2004).

[50] H. Zhang, Y. Yang, and J. F. Douglas, J. Chem. Phys. (2015).

[51] L. Gránásy, T. Pusztai, G. Tegze, J. A. Warren, and J. F. Douglas, Phys. Rev. E - Stat. Nonlinear, Soft Matter Phys. (2005).

[52] L. Lu, R. G. Alamo, and L. Mandelkern, Macromolecules (1994).

[53] H. D. Keith and F. J. Padden, J. Appl. Phys. (1963).

[54] L. Gránásy, L. Rátkai, A. Szállás, B. Korbuly, G. I. Tóth, L. Környei, and T. Pusztai, in *Metall. Mater. Trans. A Phys. Metall. Mater. Sci.* (2014).

[55] H. D. Keith and F. J. Padden, J. Polym. Sci. (2003).

[56] H. D. Keith and F. J. Padden, J. Appl. Phys. (1964).

[57] H. D. Keith and F. J. Padden, J. Polym. Sci. (2003).

[58] H. D. Keith and F. J. Padden, Macromolecules (1996).

[59] H. D. Keith and F. J. Padden, J. Appl. Phys. (1964).

[60] F. J. Padden and H. D. Keith, J. Appl. Phys. (1965).

[61] W. Hu, Phys. Rep. (2018).

[62] V. I. Vladimirov, I. P. Kuz'mina, A. A. Loshmanov, V. R. Regel', N. L. Sizova, M. A. Chernysheva, E. P. Kostyukov, I. S. Smirnov, and Y. V. Shaldin, Cryst. Res. Technol. (1986).

[63] Y. O. Punin and A. G. Shtukenberg, St. Petersbg. Univ. Press St. Petersburg, Russ. (2008).

[64] V. M. Kosevich, A. A. Sokol, B. I. Bortnik, and P. S. MELNIKOV, Kristallografiya **25**, 1045 (1980).

[65] I. E. Bolotov, A. V Kozhin, and S. B. Fisheleva, SOV PHYS CRYSTALLOGR **15**, 461 (1970).

[66] V. M. Kosevich, A. A. Sokol, and A. G. Bagmut, Sov. Phys. Crystallogr **24**, 80 (1979).

[67] A. Blatter and C. Ortiz, Appl. Phys. Lett. (1993).

[68] A. A. Chernov, *Modern Crystallography III* (1984).

[69] K. A. Jackson, *Kinetic Processes: Crystal Growth, Diffusion, and Phase Transitions in Materials* (2005).

[70] A. V Shubnikov, Kak Rastut Krist. (1935).

[71] A. V Shubnikov, Obraz. Krist. (1947).

[72] M. N. Maleev, TMPM Tschermaks Mineral. Und Petrogr. Mitteilungen (1972).

[73] Y. O. Punin and O. Yu, Zap. Vses. Miner. Ova **110**, 666 (1981).

[74] H. Tlatlik, P. Simon, A. Kawska, D. Zahn, and R. Kniep, Angew. Chemie - Int. Ed. (2006).

[75] R. Kniep and S. Busch, Angew. Chemie - Int. Ed. English (1996).

[76] P. Simon, D. Zahn, H. Lichte, and R. Kniep, Angew. Chemie - Int. Ed. (2006).

[77] P. Simon, E. Rosseeva, J. Buder, W. Carrillo-Cabrera, and R. Kniep, Adv. Funct. Mater. (2009).

[78] Z. Li, A. Geßner, J.-P. Richters, J. Kalden, T. Voss, C. Kübel, and A. Taubert, Adv. Mater. (2008).

[79] Z. Liu, X. D. Wen, X. L. Wu, Y. J. Gao, H. T. Chen, J. Zhu, and P. K. Chu, J. Am. Chem. Soc. (2009).

[80] A. Toda, M. Okamura, K. Taguchi, M. Hikosaka, and H. Kajioka, Macromolecules (2008).

[81] B. Crist and J. M. Schultz, Prog. Polym. Sci. (2016).

[82] D. C. Bassett, J. Macromol. Sci. - Phys. (2003).

[83] D. C. Bassett and R. H. Olley, Polymer (Guildf). (1984).

[84] N. Goldenfeld, J. Cryst. Growth (1987).

[85] C. M. Chan and L. Li, Adv. Polym. Sci. (2005).

[86] L. Li, C. M. Chan, K. L. Yeung, J. X. Li, K. M. Ng, and Y. Lei, Macromolecules (2001).

[87] Y. Ono and J. Kumaki, Macromolecules (2018).

[88] S. Plimpton, J. Comput. Phys. (1995).

[89] S. L. Mayo, B. D. Olafson, and W. A. Goddard, J. Phys. Chem. **94**, 8897 (1990).

[90] C. Li and A. Strachan, Polymer (Guildf). **52**, 2920 (2011).

[91] C. Li, G. A. Medvedev, E. W. Lee, J. Kim, J. M. Caruthers, and A. Strachan, Polymer (Guildf). (2012).

[92] C. Li and A. Strachan, Macromolecules (2011).

[93] C. Luo and J. U. Sommer, Macromolecules (2011).

[94] X. Jiang, G. Reiter, and W. Hu, J. Phys. Chem. B (2016).

[95] T. Verho, A. Paajanen, J. Vaari, and A. Laukkanen, Macromolecules (2018).

[96] T. Yamamoto, Adv. Polym. Sci. (2005).

[97] T. Yamamoto, Polymer (Guildf). (2009).

[98] R. S. Graham, Chem. Commun. (2014).

[99] K. Takeuchi, R. Matsuzaki, T. Okabe, and Y. Oya, Adv. Compos. Mater. (2016).

[100] P. Yi, C. R. Locker, and G. C. Rutledge, Macromolecules (2013).

[101] T. Yamamoto, J. Chem. Phys. (2013).

[102] P. Yi and G. C. Rutledge, J. Chem. Phys. (2009).

[103] G. Cao, Imp. Coll. London, Cap **4**, (2004).

[104] S. Zhang, L. Wei, W. Gao, S. Feng, and R. Liu, J. Yanshan Univ. **39**, 213 (2015).

[105] L. Alzate-Vargas, N. Onofrio, and A. Strachan, Macromolecules (2020).

[106] L. J. Abbott, K. E. Hart, and C. M. Colina, Theor. Chem. Acc. (2013).

[107] C. Li and A. Strachan, Polymer (Guildf). (2019).

[108] J. Ganster, H. P. Fink, and I. Zenke, Polymer (Guildf). **32**, 1566 (1991).

[109] J. Ganster and J. R. Lochmann, Polymer (Guildf). **31**, 1159 (1990).

[110] X. D. Liu and W. Ruland, Macromolecules **26**, 3030 (1993).

[111] R. J. Hobson and A. H. Windle, Macromolecules **26**, 6903 (1993).

[112] R. J. Hobson and A. H. Windle, Polymer (Guildf). **34**, 3582 (1993).

[113] D. D. L. Chung, *Carbon Fiber Composites* (2012).

[114] J. -S Tsai and C. -H Lin, J. Appl. Polym. Sci. **43**, 679 (1991).

[115] M. C. Weisenberger, E. A. Grulke, D. Jacques, A. T. Rantell, and R. Andrewsa, J. Nanosci. Nanotechnol. **3**, 535 (2003).

[116] J. -S Tsai and C. -H Lin, J. Appl. Polym. Sci. (1991).

[117] M. Minagawa and T. Iwamatsu, J. Polym. Sci. A1. (1980).

[118] W. B. C. and S. JR and Statton, J. Polym. Sci. Part A Polym. Chem. **55**, 531 (1961).

[119] G. Hinrichsen, J. Polym. Sci. Part C Polym. Symp. **38**, 303 (1972).

[120] Z. Bashir, Polymer (Guildf). **33**, 4304 (1992).

[121] A. Takaku and M. Shioya, J. Mater. Sci. (1990).

[122] A. K. Gupta and R. P. Singhal, J. Polym. Sci. Part A-2, Polym. Phys. (1983).

[123] S. H.-O. Gisela and Olivé, Chemistry (Easton). 123 (1979).

[124] R. H. Knibbs, J. Microsc. (1971).

[125] A. G. Dumanlı and A. H. Windle, J. Mater. Sci. (2012).

[126] B. Saha and G. C. Schatz, 2 (2012).

[127] B. Saha, Y. Dzenis, and G. C. Schatz, Carbon N. Y. **94**, 694 (2015).

[128] F. M. M. and Y. H. and Y. Kouichi and Yoshii, Macromolecules **25**, 503 (1992).

[129] B. Wunderlich, *Macromolecular Physics* (2013).

[130] A. H. B. P. and L. C. and W. N. and J. Eugenio and Strachan, ArXiv Prepr. ArXiv1503.03894 (2015).

[131] H. B. P, W. Nate, L. Chunyu, A. Andrea, J. Eugenio, and S. Alejandro, (2016).

[132] A. Strachan, G. Klimeck, and M. Lundstrom, Comput. Sci. Eng. **12**, 12 (2010).

[133] T. Shen, C. Li, B. Haley, S. Desai, and A. Strachan, Polymer (Guildf). (2018).

[134] L. H. RB and Tzentis, J. Polym. Sci. Part C Polym. Lett. **1**, 423 (1963).

[135] G. J. Martyna, M. L. Klein, and M. Tuckerman, J. Chem. Phys. **97**, 2635 (1992).

[136] S. Plimpton, P. Crozier, and A. Thompson, Sandia Natl. Lab. **18**, 43 (2007).

[137] W. J. Mortier, K. Van Genechten, and J. Gasteiger, J. Am. Chem. Soc. **107**, 829 (1985).

[138] S. L. Njo, J. Fan, and B. Van De Graaf, in *J. Mol. Catal. A Chem.* (1998), pp. 79–88.

[139] P. Bultinck, W. Langenaeker, P. Lahorte, F. De Proft, P. Geerlings, M. Waroquier, and J. P. Tollenaere, J. Phys. Chem. A **106**, 7887 (2002).

[140] C. Li and A. Strachan, Polymer (Guildf). **51**, 6058 (2010).

[141] A. C. T. Van Duin, S. Dasgupta, F. Lorant, and W. A. Goddard, J. Phys. Chem. A **105**, 9396 (2001).

[142] T. Darden, D. York, and L. Pedersen, J. Chem. Phys. **98**, 10089 (1993).

[143] R. W. Hockney and J. W. Eastwood, SIAM Rev. **25**, 540 (1988).

[144] D. T. Cromer and J. B. Mann, Acta Crystallogr. Sect. A **24**, 321 (1968).

[145] U. Shmueli, *International Tables for Crystallography, Volume B: Reciprocal Space* (Springer Science \& Business Media, 2008).

[146] S. P. Coleman, D. E. Spearot, and L. Capolungo, Model. Simul. Mater. Sci. Eng. **21**, (2013).

[147] S. A. Hosseini Ravandi, E. Hassanabadi, H. Tavanai, and R. A. Abuzade, J. Appl. Polym. Sci. **124**, 5002 (2012).

[148] G. Prusty and S. K. Swain, Polym. Compos. **32**, 1336 (2011).

[149] W. Kast, Melliand Textilber **32**, 442 (1957).

[150] F. Kumamaru, T. Kajiyama, and M. Takayanagi, J. Cryst. Growth **48**, 202 (1980).

[151] B. G. Colvin and P. Storr, Eur. Polym. J. **10**, 337 (1974).

[152] P. K. JJ and Geil, J. Polym. Sci. Part B Polym. Phys. **6**, 1381 (1968).

[153] R. A. Allen, I. M. Ward, and Z. Bashir, Polymer (Guildf). **35**, 2063 (1994).

[154] Z. Bashir, J. Polym. Sci. Part B Polym. Phys. **32**, 1115 (1994).

[155] J. Zou, Y. Wang, W. Pang, L. Shi, and F. Lu, (2012).

[156] D. P. Bahl, R. B. Mathur, and T. L. Dhami, Mater. Sci. Eng. **73**, 105 (1985).

[157] G. Capone, Acrylic Fiber Technol. Appl. 69 (1995).

[158] S. Desai, C. Li, T. Shen, and A. Strachan, J. Chem. Phys. **147**, 224705 (2017).

[159] S. Kawabata, J. Text. Inst. **81**, 432 (1990).

[160] J.-M. N. K. and T. Yoshihisa and Yang, Carbon N. Y. **118**, 168 (2017).

[161] A. Imhof and D. J. Pine, Nature (1997).

[162] R. J. Davey, Nature **428**, 374 (2004).

[163] S. Weiner, I. Sagi, and L. Addadi, Science (80-.). (2005).

[164] M. Jucker and L. C. Walker, Nature (2013).

[165] J. Zhou, Y. Yang, Y. Yang, D. S. Kim, A. Yuan, X. Tian, C. Ophus, F. Sun, A. K. Schmid, M. Nathanson, H. Heinz, Q. An, H. Zeng, P. Ercius, and J. Miao, Nature (2019).

[166] T. Shen, C. Li, and A. Strachan, Phys. Rev. Lett. **125**, 247801 (2020).

[167] R. Hill, (1953).

[168] G. J. Martyna, M. L. Klein, and M. Tuckerman, J. Chem. Phys. (1992).

[169] L. J. Fetters, D. J. Lohse, D. Richter, T. A. Witten, and A. Zirkel, Macromolecules (1994).

[170] R. Everaers, S. K. Sukumaran, G. S. Grest, C. Svaneborg, A. Sivasubramanian, and K. Kremer, Science (80-.). (2004).

[171] G. Ungar, J. Stejny, A. Keller, I. Bidd, and M. C. Whiting, Science (80-.). (1985).

[172] J. Gasteiger and M. Marsili, Tetrahedron (1980).

[173] M. V. Massa, J. L. Carvalho, and K. Dalnoki-Veress, Phys. Rev. Lett. (2006).

[174] R. L. Cormia, F. P. Price, and D. Turnbull, J. Chem. Phys. (1962).

[175] D. Turnbull and R. L. Cormia, J. Chem. Phys. (1961).

[176] S. K. Ghosh, M. Hikosaka, A. Toda, S. Yamazaki, and K. Yamada, Macromolecules (2002).

[177] S. Liang, H. Yang, K. Wang, Q. Zhang, R. Du, and Q. Fu, Acta Mater. (2008).

[178] L. Yang, R. H. Somani, I. Sics, B. S. Hsiao, R. Kolb, H. Fruitwala, and C. Ong, Macromolecules (2004).

[179] A. Toda and A. Keller, Colloid Polym. Sci. (1993).

[180] J. J. De Pablo, B. Jones, C. L. Kovacs, V. Ozolins, and A. P. Ramirez, Curr. Opin. Solid State Mater. Sci. (2014).

[181] A. France-Lanord, D. Rigby, A. Mavromaras, V. Eyert, P. Saxe, C. Freeman, and E. Wimmer, in *2014 15th Int. Conf. Therm. Mech. Mulit-Physics Simul. Exp. Microelectron. Microsystems* (2014), pp. 1–8.

[182] Y. Zhang, J. Li, X. Li, and J. He, Macromolecules (2014).

[183] S. Arichi, M. Y. Pedram, and J. M. G. Cowie, Eur. Polym. J. (1979).

[184] S. Grossman, A. Stolarczyk, and O. Vogl, Monatshefte Für Chemie (1981).

[185] CROW, Polymerdatabase.Com (2015).

[186] C. W. Bunn, Trans. Faraday Soc. (1939).

[187] B. Wunderlich, *Macromolecular Physics Vol. 1: Crystal Structure, Morphology, Defects* (1973).

[188] L. H. Sperling, in *Introd. to Phys. Polym. Sci.* (2005).

[189] A. Stukowski, Model. Simul. Mater. Sci. Eng. (2010).